



UNIVERSITÀ
DI PAVIA



Jointly Supervised Ph.D

Università degli Studi di Pavia

Ph.D School in Electronics, Computer and Electrical Engineering

Universidad de Cantabria

Ph.D School in Mobile Network Information and Communication
Technologies

Components and devices for de-pointing correction of antenna autotrack system

Doctoral Thesis of:
GABRIELE CECCATO

Supervisors:

Prof. Luca Perregrini

Prof. Angel Mediavilla

Academic Cycle XXXIV
2018-2021

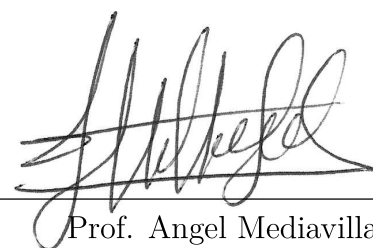
Università di Pavia - Universidad de Cantabria

Dipartimento di Ingegneria Industriale e dell'Informazione

Departamento de Ingeniería de Comunicaciones



Prof. Luca Perregrini
Supervisor



Prof. Angel Mediavilla
Supervisor

Acknowledgements

I would like to thank my supervisors, Prof. Luca Perregrini and Prof. Angel Mediavilla, for the amazing opportunity to work in space-related projects making me completely addicted to the electromagnetic environment and that letting me stalk them in these years, sharing them knowledges and wisdom that I will bring in my entire career.

A special thank all my colleagues Lorenzo, Nicolò, Simona, Giulia, Giuseppe, Simone, Valentina, Martina, Dajana and all the people that spent months in our group, making the Lab a sort of second family.

Thank to Marco, for following me and giving me technical and life advises.

And also to Matteo, my wingman, for sharing with me all the joys and pains that the PhD life can lead.

Thank to Dr. Juan Luis Cano for his support and advice during the period spent in Santander.

Thank to Dr. Luca Piffer from FDS Italy for his support for the project of radomes.

Contents

1	Tracking Principle	1
1.1	Tracking	2
1.1.1	Range measurements	2
1.1.2	Angular measurements	3
1.2	Monopulse	4
1.2.1	Multiple source	6
1.3	Multiple modes	7
1.4	Monopulse Chain Components	11
1.4.1	Mode Extraction	11
1.4.2	Combining Network	17
1.5	Example of Combining Networks	21
	References	24
2	Monopulse In-Lab Calibration System	27
2.1	Monopulse In-lab Bench Test	28
2.1.1	Excitation Coefficient High Order Modes	29
2.1.2	Mathematical Model of the Step-Waveguide Junction	33
2.1.3	Simulated Modes Excitation from the Calibration Tower	37
2.2	Design of monopulse waveguide components	40
2.2.1	Circular-To-Circular Waveguide	40
2.2.2	3dB/90° Hybrid Coupler	42
2.2.3	Compact Quadrature Hybrid Coupler	43
2.2.4	Septum Polarizer	48
2.2.5	Radiating Load	49
2.2.6	Mode Coupler	50
2.3	OCWG Measurements and Tracking test	52
2.4	Conclusion	57
	References	57
3	Radome Effects on tracking	59
3.1	Multi-Layer Radome	62
3.1.1	IFR Model and Joint Compensation	63
3.1.2	Compensating Ladders Design	68
3.2	Weather Raining Condition	74
3.3	Conclusion	81
	References	81
	List of Publications	84

*Ai miei genitori,
per non avermi tagliato i viveri*

Introduction

In order to establish a proper communication with a spacecraft from a ground station located on the earth's surface, the antenna should be able to point correctly the target. This is called spacecraft tracking. The most common way to track is through autotrack: the antenna will follow automatically the source once the signal is acquired, refining the previous position with feedback signals.

To track spacial targets there are two typical ways:

- **program track:** knowing the orbital parameters and roughly the position of the target, a controller sends these informations to drive motors of the antenna to point it;
- **autotrack:** the antenna will follow automatically the source once the signal is acquired, refining the previous position. Ideally in autotrack, the controller needs just the orbital parameters (but should be constantly reviewed) without knowing anything else.

Monopulse is the popular type of autotrack. In literature is possible to find configuration with one feed system or clusters of feeds of the same type, but the one studied in this work will be the single feed configuration, largely used in space and aeronautic environment.

Monopulse provides two DC signals, the *sum* (Σ) and *delta* (Δ), and thanks to their pattern Σ channel is used for communication purposes, while Δ is used for tracking. The latter gives two angular informations: measure of *azimuth* and *elevation* each one controlling the dedicated antenna's drive motor in order to move it and correct the pointing. Due to atmospheric effects (wind, gusts and even gravity) servos may not be able to a point in the correct direction without a retro-action and therefore other processing steps are needed to correct this kind of errors. If from one side, monopulse allow a complete automatic way to track spacecraft, on the other hand it is commonly affected by de-pointing problems, mainly due to design of waveguide components that can be critical in the generation of DELTA signal.

Environment not only generates mechanical problems described before, but is also a source of electromagnetic problems due to scattering effects. Due to its geometry, an antenna can become a collector of water, snow and ice that downgrades its performances. To avoid that, special structures can be designed to cover and protect the ground station (i.e. radomes); but if from one side this protections solve the environmental problem, on the other side, these structure are placed in front of the antenna that can cause electromagnetic blockage, scattering and so on.

The aim of this thesis will be give a general overview on tracking monopulse systems, explaining how the generation of SUM and DELTA signals is made, underlining possible causes of tracking errors.

Once understood the basic concept on the monopulse principle, Chapter 2 will aim to prevent and possibly correct tracking errors by designing an in-lab testing system for the monopulse tracking chain that mimics the same operation that is commonly performed in

every monopulse antenna before being operative: the calibration. This is typically done down-timing the whole antenna at high costs. The proposed in-lab system will avoid antenna's downtime, testing the monopulse tracking chain before being installed in the ground station. Finally, the third Chapter 3 will aim to explain environmental effects on tracking systems and how radome coverage is made. Electromagnetic analysis of radome is performed in both dry and wet conditions by experimentally simulating rain effects on panels. It will be explained how minimize tracking problems due to radomes by designing special compensating structures as well as different panels solutions.

1

Tracking Principle

The first type of tracking system ever designed is the human being.

The receiving system of a person are his eyes, which collect the visual information to determine the position of a target. This information is processed by a processor, the occipital lobe of the brain, that computes the distance that separates him from the target, allowing the recognition and giving him the possibility to follow the object as it moves in the space.

From the electrical point of view, human eyes are photodetectors collecting the electromagnetic radiation in the visible band between $390 \mu\text{m}$ to $700 \mu\text{m}$ of the spectrum, or between 430 THz to 770 THz ; the information is then elaborated by the processor that builds the image with a given resolution and keep in line of sight the target and generating some sort of feedback signal to follow the target in space by moving head and eyes.

To replicate the behavior of human eyes, scientists and engineers developed an artificial system using electromagnetic (EM) waves to detect targets' positions: the RADAR (RADIO Detection And Ranging). Its basic principle is to illuminate a certain area in space and detect the EM field scattered by an object. Directive antennas are used to illuminate a specific area with a wide or very narrow radiation pattern to roughly scan the area in sight, or identify with high precision the type of object, respectively.

In a basic RADAR system, when a target is inside his field of view, EM field impinges the object and is reflected back to the antenna. In this way, range (or distance) measurement is determined considering the time needed by the field to reach the target and come back to the antenna. To determine angular position, instead, antenna can be moved of a small amount inside a determined area, in order to maintain the target insight.

These measurements are generally performed in the microwave region of the EM spectrum because electromagnetic fields are less not affected by atmospheric attenuation and ideally allows the detection with any weather condition. In any case, as described in Chapter ??, atmosphere plays a big role in tracking and if not considered, catastrophic situations may occur (for example lose a target). Terrestrial applications mainly use frequencies between 100 MHz to $20 - 40 \text{ GHz}$.

The lower boundary at 100 MHz is due to the fact that antennas' dimension would be too large and the ionosphere reflects any incident field back to the surface with frequency lower than the resonance of plasma ($5 - 7 \text{ MHz}$); the upper boundary is due to the atmosphere that absorbs around 22 GHz which is the first resonant frequency of the oxygen while at 35 GHz becomes important the presence of rain and fog. At 60 GHz the oxygen's resonant frequency plays an important role. [1]. Table 1.1 represents the standard frequency bands used.

Table 1.1: IEEE definition of the frequency bands [1]

	L	S	C	X	Ku	K	Ka	V	W	mm
(GHz)	1-2	2-4	4-8	8-12	12-18	18-27	27-40	40-75	75-110	110-300

Today radars are used in naval and aeronautic applications, both military and civil [2]; recently are also been installed for automotive applications, like self-parking cars, industrial, etc. [3]

While for terrestrial application simple tracking techniques can be successfully used, for space application it is not possible to assure high precision, since targets are located at hundreds (low orbit spacecrafts) or even million or billion of kilometers (interplanetary missions, for example Mars 2020, or deep space missions for example Voyager) far from the antenna.

1.1 Tracking

Tracking system is typically composed by an antenna fed through a waveguide structure where the EM field propagates and is converted into electric signal for processors, amplifiers and converters. (see Fig. 1.1)

Components for space applications are designed following strict requirements (ECSS standards) due to the unfriendly environment that is the space; therefore hardware for this type of systems need to be perfectly designed, using the most reliable components. Antennas for space applications might have the typical parabolic shape with very high gains in order to focus the transmitted power in a small region (i.e. ground stations antennas), or also planar arrays with a very broad directive in order to be easily tracked (i.e. spacecraft antennas). Two type of measures can be performed to determine targets' positions: range measurement, for the distance between an object and the ground station, or angular measurements to determine the position in space.

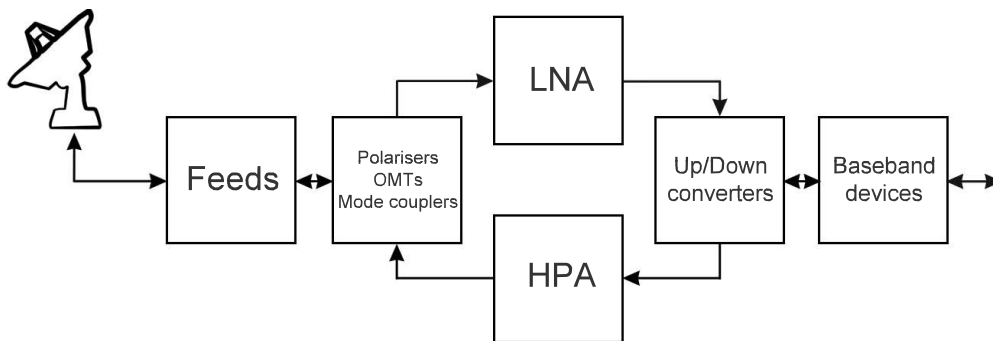


Figure 1.1: Transmission/Reception Chain

1.1.1 Range measurements

- Ranging pulse: an un-modulated pulse is sent to the target and measured the time needed to return to the antenna. This type of measurement is used with collaborative targets because the pulse need to be collected, processed by the transponder and sent back to the ground station (Fig. 1.2a);

- ranging tones: satellite send a modulated signal to compare it with another modulated signal generated by the ground station. In this case phase would be a problem because would assume the same amount every 2π (phase wrapping), therefore a multiple frequency signal is preferred, using the central one as reference (Fig. 1.2*b*);
- radar: used with non collaborative targets considering the time needed by the field to reach the target and come back to the antenna (Fig. 1.2*c*);

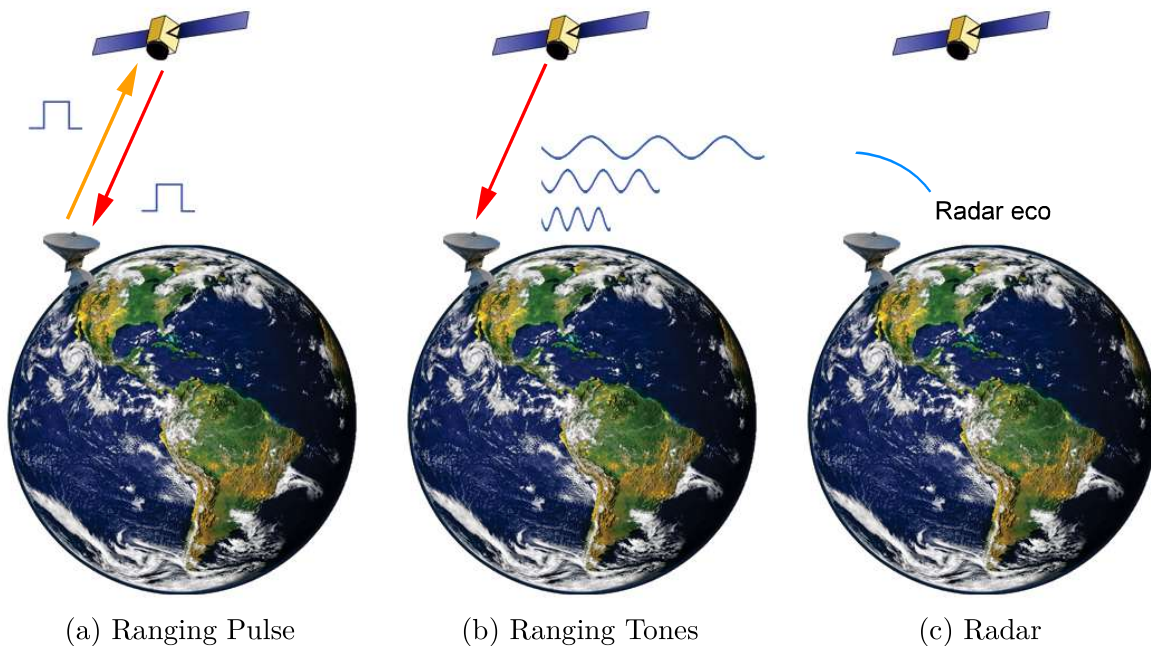


Figure 1.2: Range Measurements

1.1.2 Angular measurements

- Conical Scan: consists in moving the antenna in a circular path in order to maintain the target inside the center of the beam. Cons of this technique is the difficulty to move large antennas in a continuous way in order to maintain a target pointed; moreover, a minimum pointing error may cause losing target, especially for very distant ones such as deep-space missions (Fig. 1.3*a*);
- monopulse: the most used way to track targets, exploits by two channels: SUM and DELTA signals. The first one that is the classic main lobe of the antenna used for ranging measurement and data transmission. DELTA signal is the core of this system, formed by two signals (similar to the SUM) shifted by 180° the one to another; a target is said to be tracked when DELTA gives a null signal value, while non-null signals refer when the antenna is not pointing exactly the target. Using two signals is possible to determine not only the target position, but also generate a sort of feedback to control servos and re-point the antenna. Due to this feature, monopulse is able not only to track but also to lock and follow a target in space (Fig. 1.3*b*);
- delta-DOR: uses two ground stations displaced far away the one to another and a well-known reference source signal (i.e. pulsar or quasar) to triangulate the object

position, comparing the angle formed between the cosmic source and the target (Fig. 1.3c).

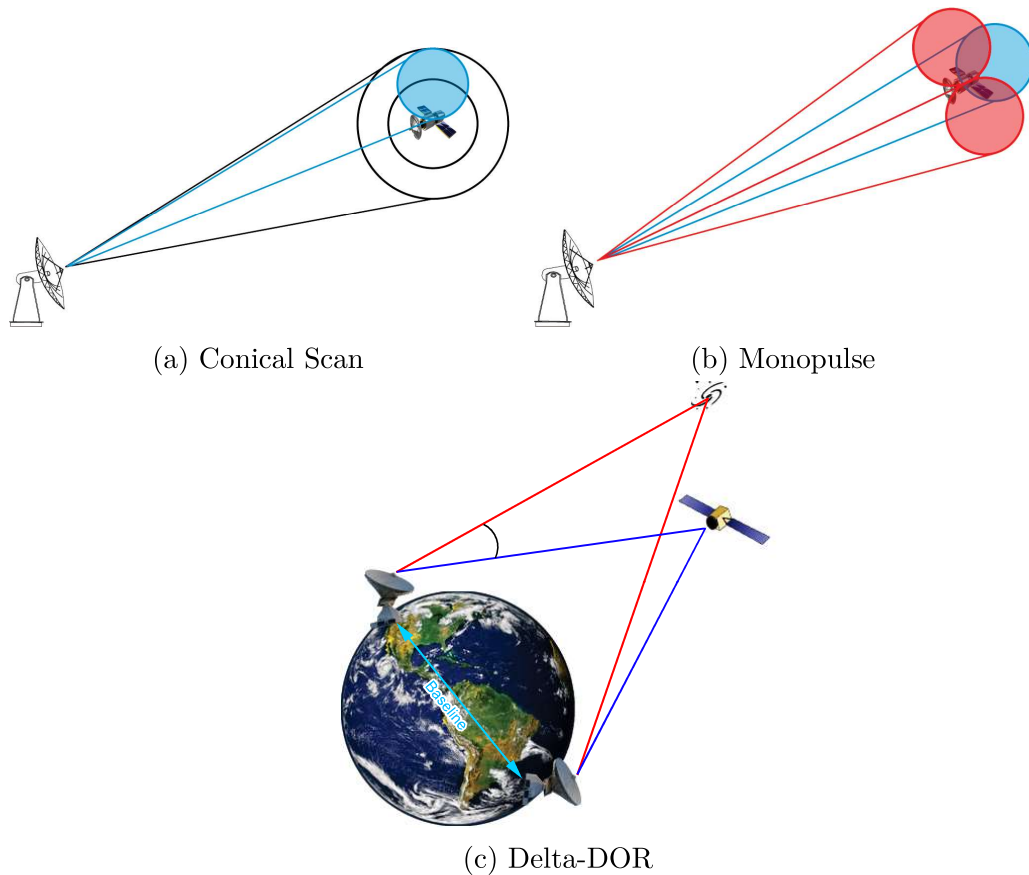


Figure 1.3: Angular Measurements

1.2 Monopulse

Monopulse is a hybrid word: *mono-*, meaning *one* from Greek, and *-pulse* from Latin *pulsus*. The angle estimate is possible using a single pulse (hence the name monopulse), but also multiple pulses are usually employed to improve the accuracy of the estimate. [4]

Monopulse systems are composed by two signals: SUM and DELTA shown in Fig. 1.4. SUM signal is the classic main lobe of the antenna; DELTA signal is the core of this tracking system because allows to measure the angular position of a spacecraft. Target is tracked (i.e. its direction is perfectly aligned with the boresight of the antenna) when DELTA signal is zero, which means that the antenna is pointing the spacecraft exactly in the NULL direction; when the measured signal is not zero, the characteristics of the DELTA pattern allow to detect angular position and also understand in which direction the antenna should be moved. To work correctly SUM and DELTA signal must be aligned; it means that when SUM signal is at its maximum value, DELTA signal has to be minimum.

If not, tracking errors may appear. Modern monopulse systems are typically based on multimodal waveguide components where the SUM and DELTA signals are composed by combination of multiple modes.

Typically, the fundamental mode is used for the SUM signal, while a combination of higher order modes for the DELTA signal. The combination of higher order modes (HOMs) is chosen such that the phase carries the information on the direction, while its amplitude, the amount of mispointing. But in the history, mono-modal systems were firstly used [4].

In a typical azimuth-over-elevation mount antenna, the information carried by SUM and DELTA signals to correct the antenna position with respect to the target is done through the Tracking Receiver [5] (or IQ demodulator in Fig. 1.5) that generates two error signals that are proportional to the misalignment. The tracking information is typically normalized with respect to the SUM signal (ratio DELTA over SUM).

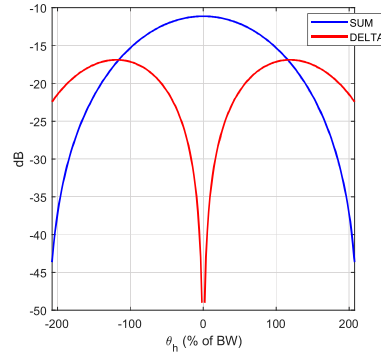


Figure 1.4: 2D radiation pattern of a monopulse tracking system

Given two signals $v(t)$ and $v_r(t)$ modulated in amplitude and phase [4]

$$\begin{aligned} v(t) &= a \cos(\omega t + \phi) \\ v_r(t) &= a_m a \cos(\omega t + \phi + \phi_m(t)) \end{aligned}$$

that in phasor representation, are represented as

$$\begin{aligned} V(t) &= a e^{j(\omega t + \phi)} \\ V_r(t) &= a e^{j(\omega t + \phi)} a_m e^{j\phi_m(t)} \end{aligned}$$

it is possible to represent through a Cartesian representation

$$m(t) = I(t) + jQ(t) \quad (1.1)$$

where the in-phase and quadrature components are

$$\begin{aligned} I(t) &= a_m \cos \phi_m(t) \\ Q(t) &= a_m \sin \phi_m(t) \end{aligned} \quad (1.2)$$

$$Re \left\{ \frac{d}{s} \right\} = \frac{d_I s_I + d_Q s_Q}{s_I^2 + s_Q^2} \quad (1.3)$$

$$Im \left\{ \frac{d}{s} \right\} = \frac{d_Q s_I + d_I s_Q}{s_I^2 + s_Q^2} \quad (1.4)$$

These two signals represent azimuth and elevation errors and are typically provided to the Antenna Control Unit (ACU) that moves the antenna in order to correct its position with

respect to the target. These values also determine the speed of the antenna that has to move to be aligned with the target.

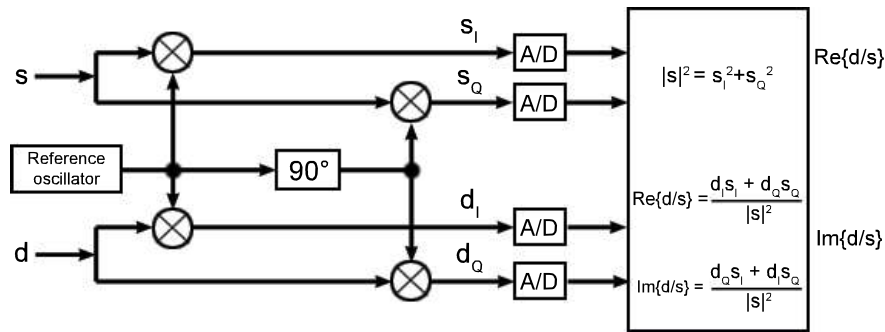


Figure 1.5: Example of tracking receiver [4]

1.2.1 Multiple source

In the history, the first kind of monopulse systems use a parabolic-reflector antenna fed by four horns in the focal plane [4]. This configuration produces four squinted beams in which the upper horns produce the lower beam and the lower horns vice-versa. A target senses equal amplitudes only on the axis of symmetry of the antenna, while different amplitudes in other directions depending on the radiation pattern.

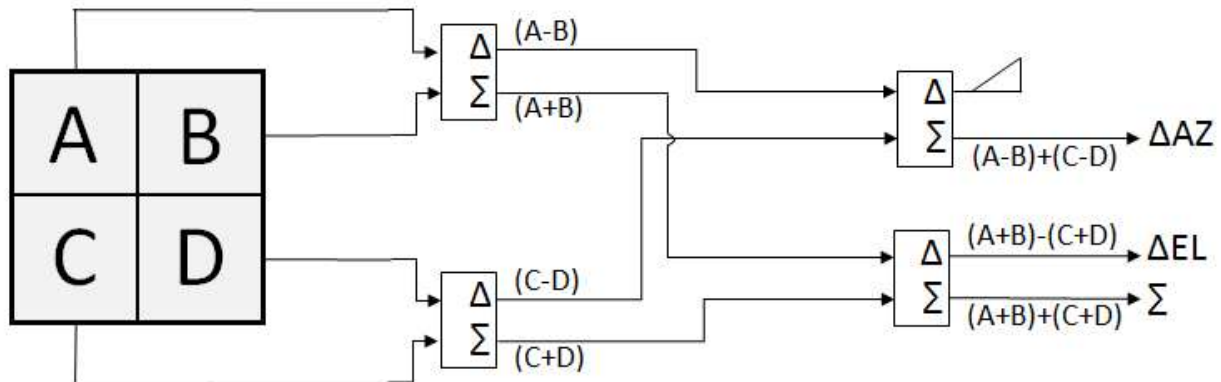


Figure 1.6: Four horns configuration A, B, C, D horns

The obtained pattern is affected by mutual coupling, therefore it would not be the same as the one that would be obtained from individual horns if the other three were missing. Taking as reference Figure 1.6 and calling A, B, C, D the voltages corresponding to each horn, the sum and difference signals would be:

$$\begin{aligned}
 s &= \frac{1}{2}(A + B + C + D) \\
 d_{az} &= \frac{1}{2}[(A - B) + (C - D)] \\
 d_{el} &= \frac{1}{2}[(A + B) - (C + D)]
 \end{aligned} \tag{1.5}$$

where s represents SUM signal, d_{az} the azimuth difference and d_{el} the elevation difference. The direction in which azimuth and elevations are nulls, is called monopulse axis that

corresponds to the boresight direction of the antenna.

Azimuth and elevation are measured between the horizontal plane and the slant plane respectively, as shown in Fig. 1.7.

- the slant plane is perpendicular to the vertical boresight plane, containing the line of sight to the target;
- the azimuth angle is measured from the slant plane and the vertical boresight plane intersection.

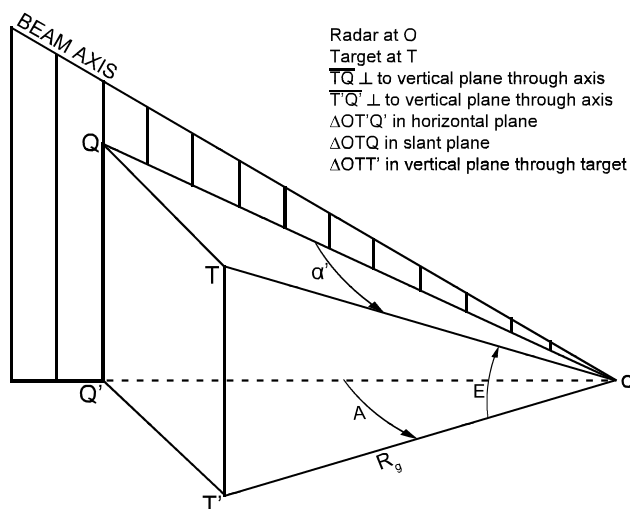


Figure 1.7: Relations among azimuth and elevation axis [4]

In reception, the radio-frequency (RF) sum and difference signals are combined and down-converted to intermediate frequency (IF) and mixed with the output of a local oscillator to be amplified and filtered at IF. This signal will be processed by a monopulse processor where the output is the ratio of the Δ signal and the Σ signal (see example in Fig. 1.5), multiplied by a cosine of the local oscillator. The cosine will be $+1$ if the target is on one side of the axis, and -1 when is on the other side. The amplitude ratio gives also the information how is far the target is off axis; the cosine factor reduces also errors due to noise.

1.3 Multiple modes

The directly next generation of multiple source systems exploits the capability of a waveguide to propagate HOMs.

Waveguides are commonly used in space applications because allow the propagation of EM waves in a confined space, isolated from external environment and therefore less affected by interference. Furthermore, these components are typically made of aluminum providing a high resistivity to mechanical shocks that are common in the space environment.

Circular waveguides are typically used in space application, allowing the propagation of circular polarized fields shown in Fig. 1.8 because are less affected by propagation interference.

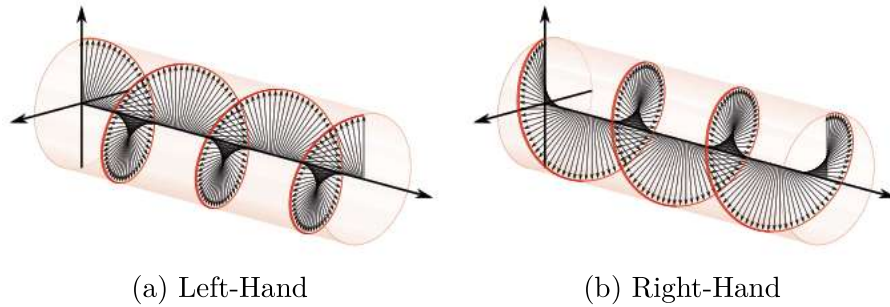


Figure 1.8: Circular Polarization

The fundamental mode in a circular waveguide is the degenerate TE_{11} (cosine and sine) in which the E-field is transversal with the maximum at center (Fig. 1.9a,b), while the H-field perpendicular to it, describes a closed contour that extends inside the waveguide. For its radiation characteristics, this mode is perfect to be used for communications and range measurements, building SUM signal.

The first HOM is the TM_{01} in which the E-field is radial in the cross-section with a null in the center of the structure and at the boundary, while a maximum in the annular region in between (Fig.1.9c); the H-field is transversal describing circles around the center of the structure. This mode is typically used in combination with the TE_{01} to build DELTA signal. The subsequent one is the TE_{21} degenerate (cosine and sine) in which the E-field has a null at the center and four regions of maximum alternated with regions of null in the annular space between the center and the boundary for TE_{21}^c , while the same behavior rotated by 45° for the TE_{21}^s (Fig. 1.9d,e). H-field describes a closed contour that extends inside the waveguide with a null at the center and maximum at the four corner. Exploiting the null in the center of the electric field, the two degenerate modes are typically used to build DELTA signal.

Then the TE_{01} is the opposite of the TM_{01} with the E-field transversal describing circles around the center, with a null exactly in the center and maximum at half way between the center and the boundary of the waveguide (figure 1.9f), while the H-field radial opposite with respect to the E-field. For its characteristics is typically used in combination with the TM_{01} to build DELTA signal.

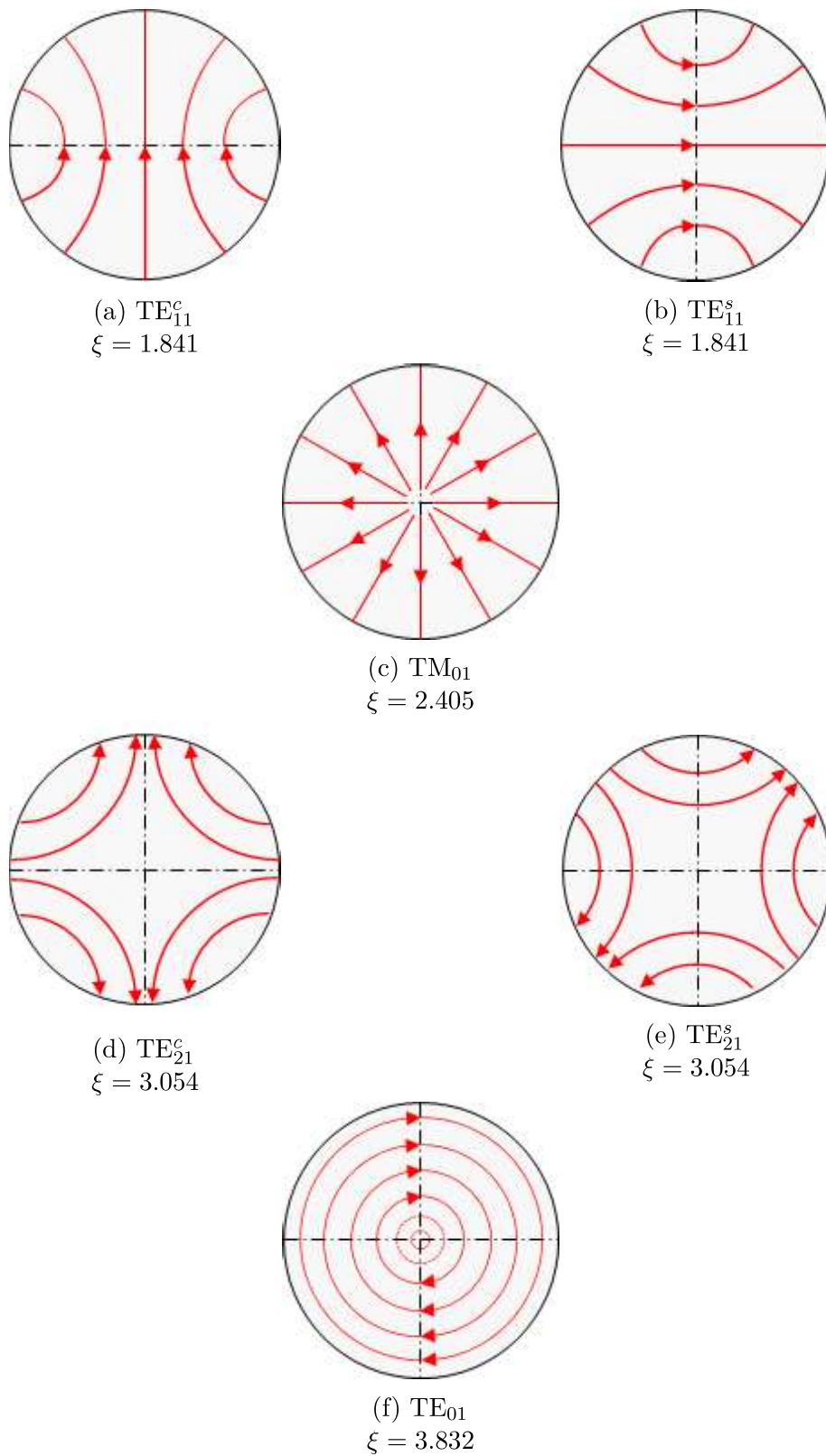


Figure 1.9: Electric field of propagating High Order Modes in circular waveguide. ξ the zeroes of the Bessel functions

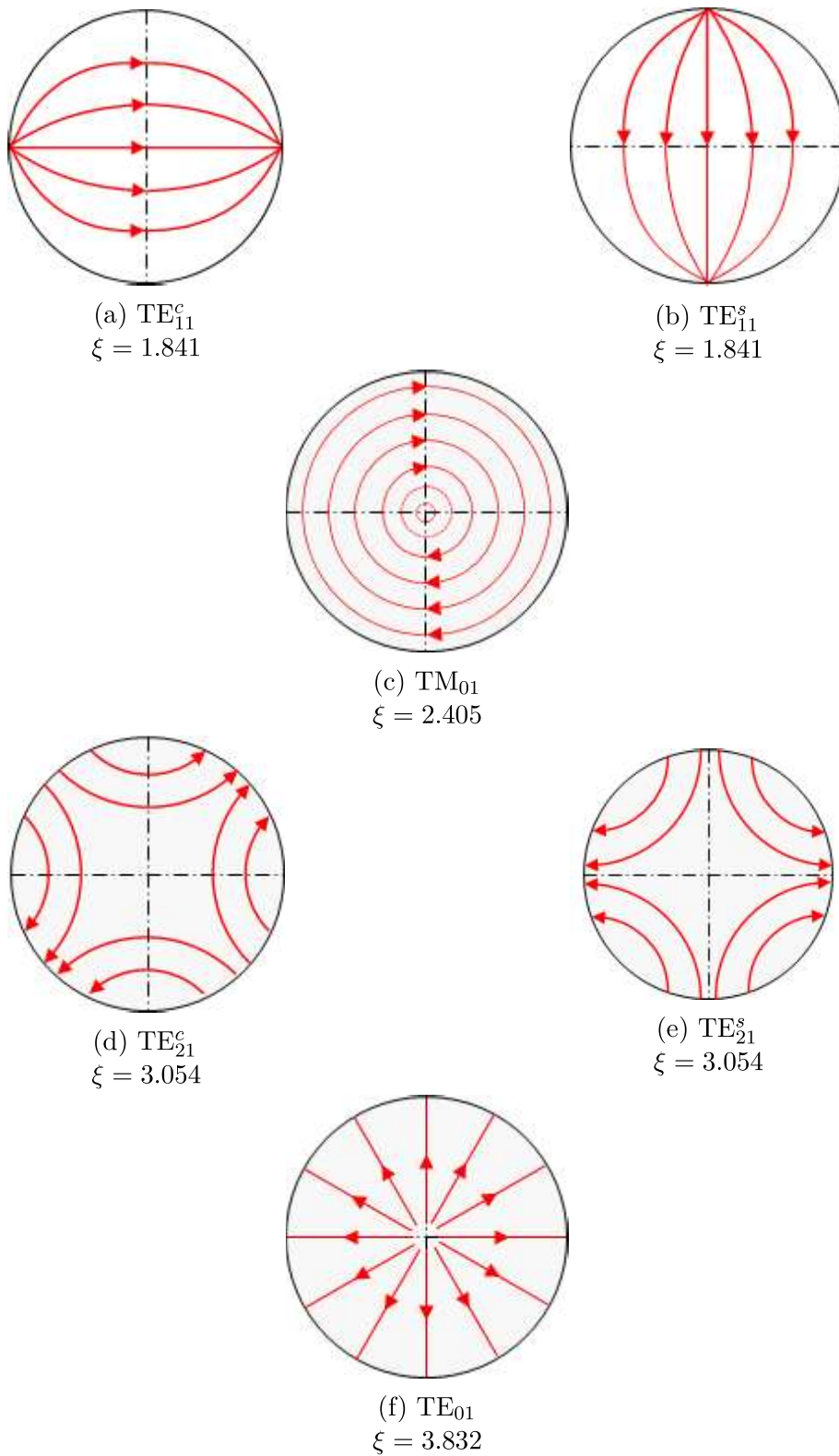


Figure 1.10: Magnetic field of propagating High Order Modes in circular waveguide. ξ the zeroes of the Bessel functions

1.4 Monopulse Chain Components

An impinging EM field propagating in the environment must be collected through a feed that generates the signals exciting HOMs in the waveguide network. HOMs must be separated to extract the modes needed for the monopulse to build SUM and DELTA signals. The most common way to separate modes in a waveguide structure is through mode couplers and once each mode is separated, the extracted signal will be processed in the tracking receiver to generate SUM and the DELTA signal.

Fig. 1.11 explains the process that an impinging signal is processed. The result is the SUM and DELTA shown in Fig. 1.4

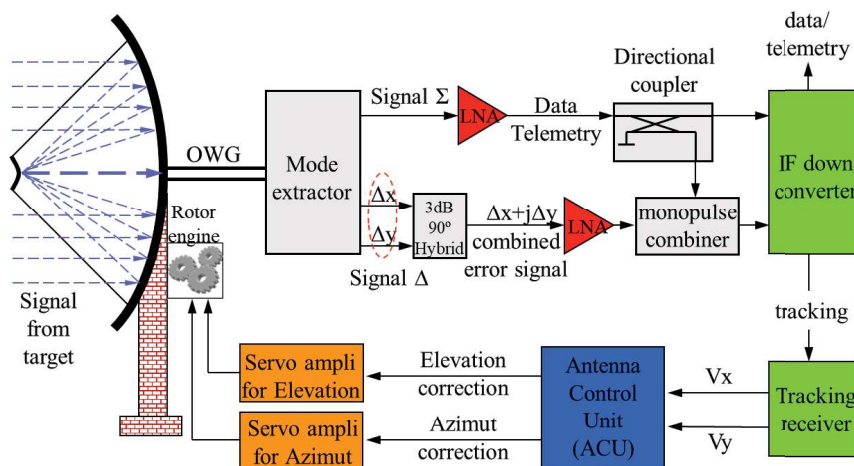


Figure 1.11: Complete scheme of a monopulse system.

1.4.1 Mode Extraction

Mode couplers are components made by different waveguides with a common core where the collected signal from the feed propagates. Attached to the common waveguide, smaller waveguides are displaced to allow the extraction of a specific mode. Generally, the most common mode coupler is the travelling wave type, where the core structure is a classical waveguide (typically circular in space applications), sufficiently large to allow the propagation of the needed HOMs. The specific mode is extracted through slots in the main circular waveguide positioned in such way that electric or magnetic coupling is possible. These slots could have rectangular or circular shapes and the number of slots to extract the same mode depends on the bandwidth needed for the component.

Mode extraction using slots are made with rectangular waveguide (of dimensions a and b) allowing the propagation of the fundamental TE_{10} mode. When HOMs propagate in the circular waveguide has the correct field distribution to be coupled inside the slot, this aperture collects the EM field exploiting electric or magnetic coupling (depending on the orientation aperture) and if the extraction is made through a rectangular waveguide, the only TE_{10} mode is excited. In the case that HOMs do not have the correct field distribution, TE_{10} is not excited. The electrical signal is typically extracted through coaxial pins, while both termination of the rectangular waveguide must be closed with a matching load to avoid back reflections that may degrade the field quality.

Electric coupling happens when TE_{10} is generated through the coupling of the E-field from the circular to the rectangular waveguide. This is possible when the long side a is perpendicular to the circular waveguide propagation axis, taking the name of transversal slots (Fig. 1.12). Vice-versa, magnetic coupling happens when TE_{10} is generated through the coupling of the H-field from the circular to the rectangular waveguide and this is possible when the long side a is along the circular waveguide propagation axis. This refers to axial slots as shown in Fig. 1.13.

These two types work in the same way and each configuration is able to extract the desired mode. It is possible to divide these two categories of slots into two others subcategories, depending on the orientation. Can be horizontal or vertical, and again they are completely exchangeable.

The existence of these categories is just for a design point of view. When the space surrounding the extractor is limited, is possible to choose the most convenient configuration. It is mandatory that the component have all the slots working in the same way without mixing the two behaviours.

From a theoretical point of view, it is possible to extract a specific mode using a single slot, but since a circular waveguide allows the propagation of several HOMs, the single-slot configuration would couple not only the needed HOM, but also all the others that share the same electric or magnetic coupling. Therefore this solution would be a combination of multiple modes that would be catastrophic for the monopulse system. Another reason to not use a single-slot configuration is the asymmetry of the structure: small variations of the EM field would not the needed mode in the correct way. Therefore a more stable configuration is using at least a pair of slots for each HOM.

Different solutions are available in the market: with two, four or even eight slots as described in Chapters 1.4.1.1, 1.4.1.2 and 1.4.1.3 respectively, and also with electric or magnetic coupling.

From a design point of view there exist three categories of mode couplers: travelling wave couplers described in detail in this work, geometrical couplers in which modes are generated using a particular geometric shape for a single aperture or set of apertures and finally resonant couplers, where modes are generated by the development of standing waves in resonant cavity. This type of mode coupler can be used for narrow-band operations [5]. More advanced and broadband designs are the multi-hole mode couplers are presented in Chapter ?? , where the rectangular waveguide extends to the entire length of the circular waveguide and apertures in the shared wall allow magnetic coupling.

These components might be the main cause loss in the performance of an autotrack system and might introduce misalignment errors.

It is common to find transitions (as shown in Fig. 1.14) from wider to narrower circular waveguide in a mode coupler in order to reject all the HOMs of no interest. The transition need to be done smoothly to avoid reflections at the interface. These transitions allow the simplest mode extraction for the SUM signal, since it is obtained through the only fundamental TE_{11} modes.

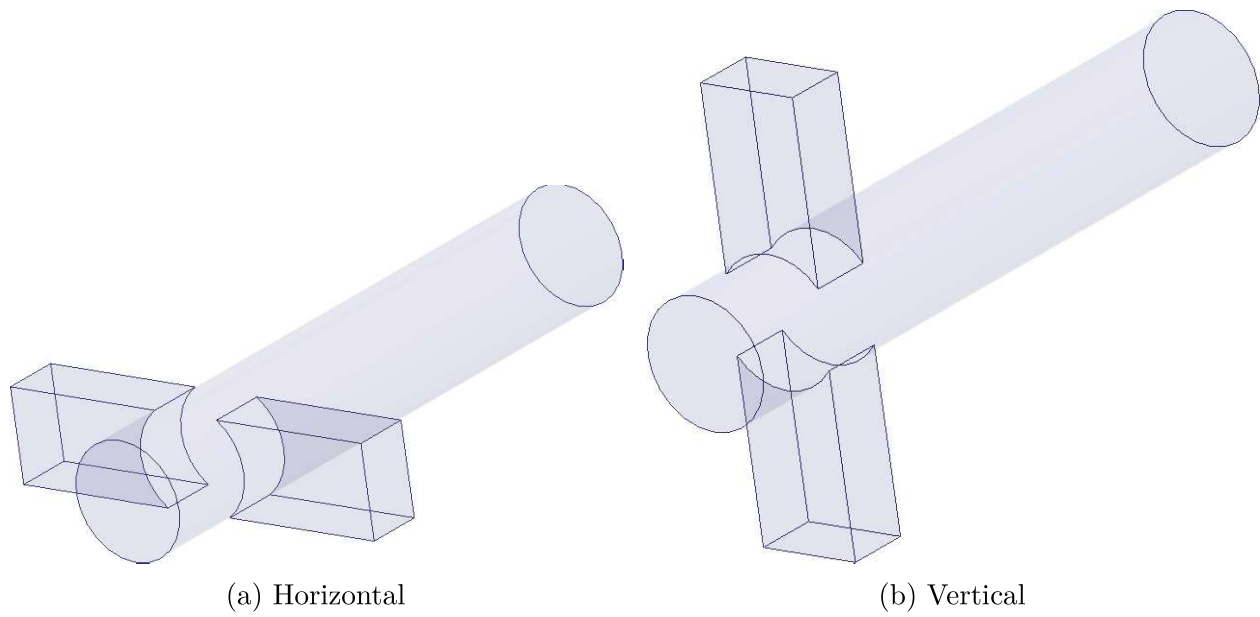


Figure 1.12: Example of a 2-port Transversal Mode Extractor

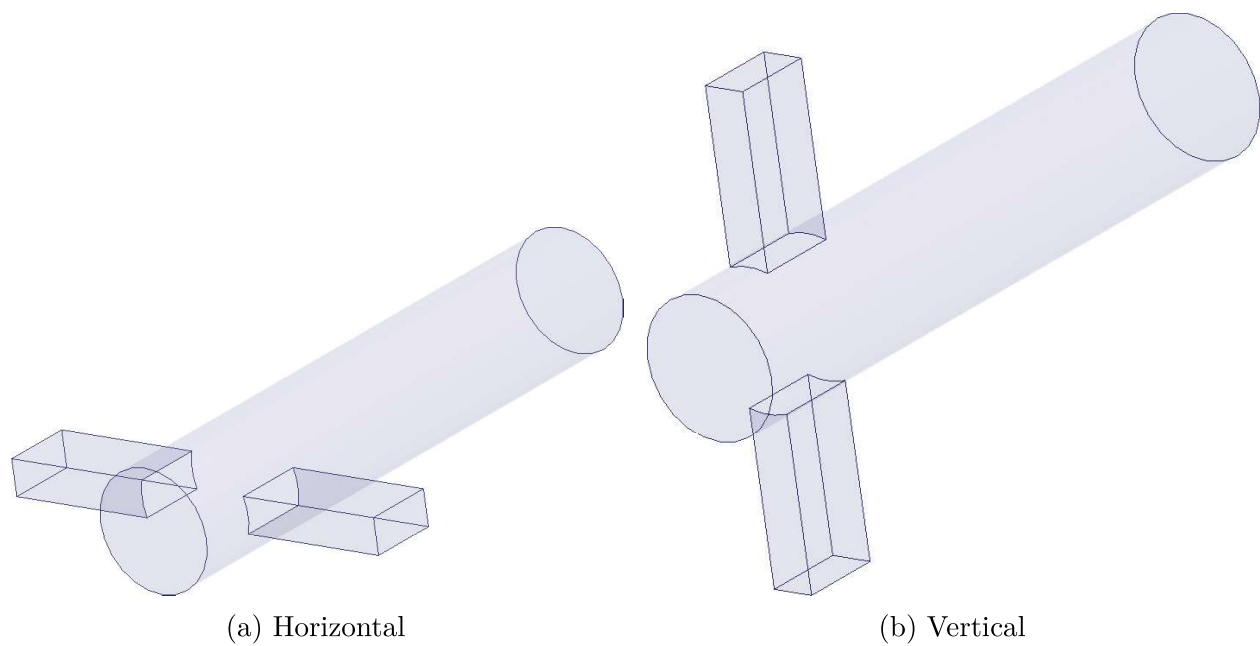


Figure 1.13: Example of a 2-port Axial Mode Extractor

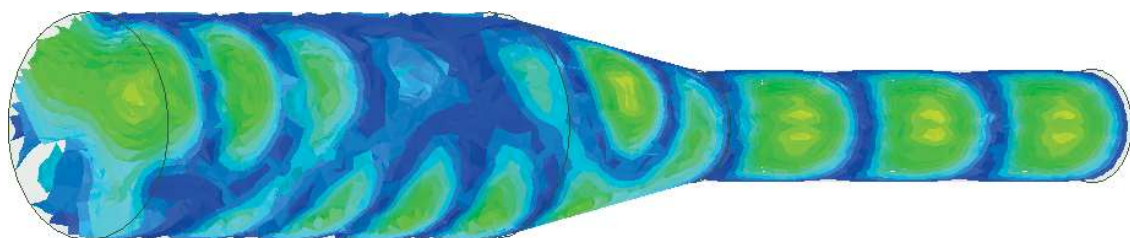


Figure 1.14: Wider-to-Narrower Transition

1.4.1.1 2-way coupler

The use of two slots is the simplest way to extract modes propagating in a waveguide. In the figures below is shown how the extraction using axial or transversal slots is completely exchangeable depending on which mode is need to be extracted.

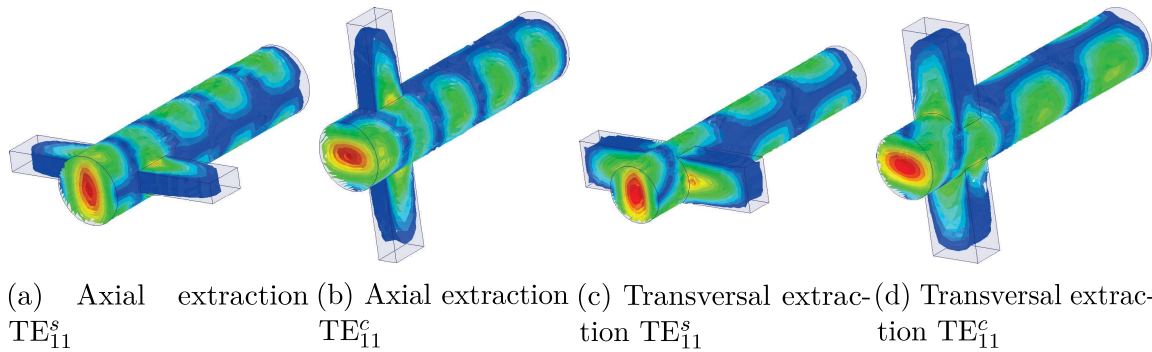


Figure 1.15: Example of 2-port extractors

Using just two slots allows the extraction not only of the needed mode, but also all the other modes propagating inside the circular waveguide concordant with the magnetic or electric coupling, depending on the orientation of the used slots as shown in Fig. 1.15. For example the axial slots allow to extract both TE_{11} and TE_{21} at the same time therefore is not possible to use it for the monopulse. To solve this problem is possible to break the symmetry using still two slots as shown in Fig. 1.16; in this way it is possible to extract the TE_{21}^c with one slot and TE_{21}^s with the other, giving the basic mode extractor for the DELTA signal. As is shown in the Figures 1.16, TE_{21}^c is coupled through the axial slot rotated by 0° with respect to the vertical direction, while TE_{21}^s mode is coupled through the axial slot rotated by 135° along the vertical direction while the other slot is barely excited.

With a 2-port coupler it is only possible to achieve coupling factors of -3 dB because with a single slot to extract the correspondent HOM (TE_{21}^s or TE_{21}^c), only half of the power can be extracted. Therefore to increase the coupling coefficient and the selectivity, configurations with four or eight slots exploiting the symmetric behaviour are needed.

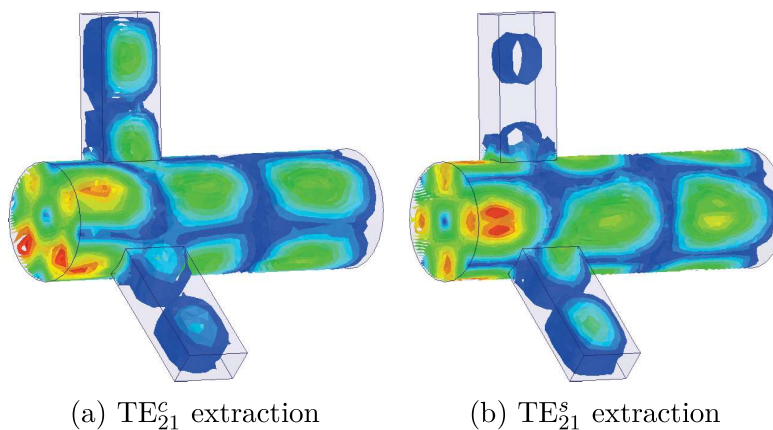


Figure 1.16: Example of 2-port TE_{21} extractors

1.4.1.2 4-way coupling

To increase the coupling coefficient and reject undesired modes, can be used more than two slots. For instance, in case the TE_{21} mode need to be coupled two slots are sufficient but TE_{11} is coupled as well in the same slots, generating interferences in the extracted signal. In order to extract just the two TE_{21} four slots are needed (see Fig. 1.17).

TE_{21}^c has the electric field rotated by 45 degree therefore to extract it can be used four axial slots rotated by 45 degree with respect to the electric field in order to obtain the magnetic coupling.

To extract TE_{21}^s four axial slots rotated by 45 degree with respect to the electric field are needed and each slot presents a coupling factor of -3 dB.

Using four slots, the extraction of the single TE_{21} degenerate mode is possible, without extract any other modes.

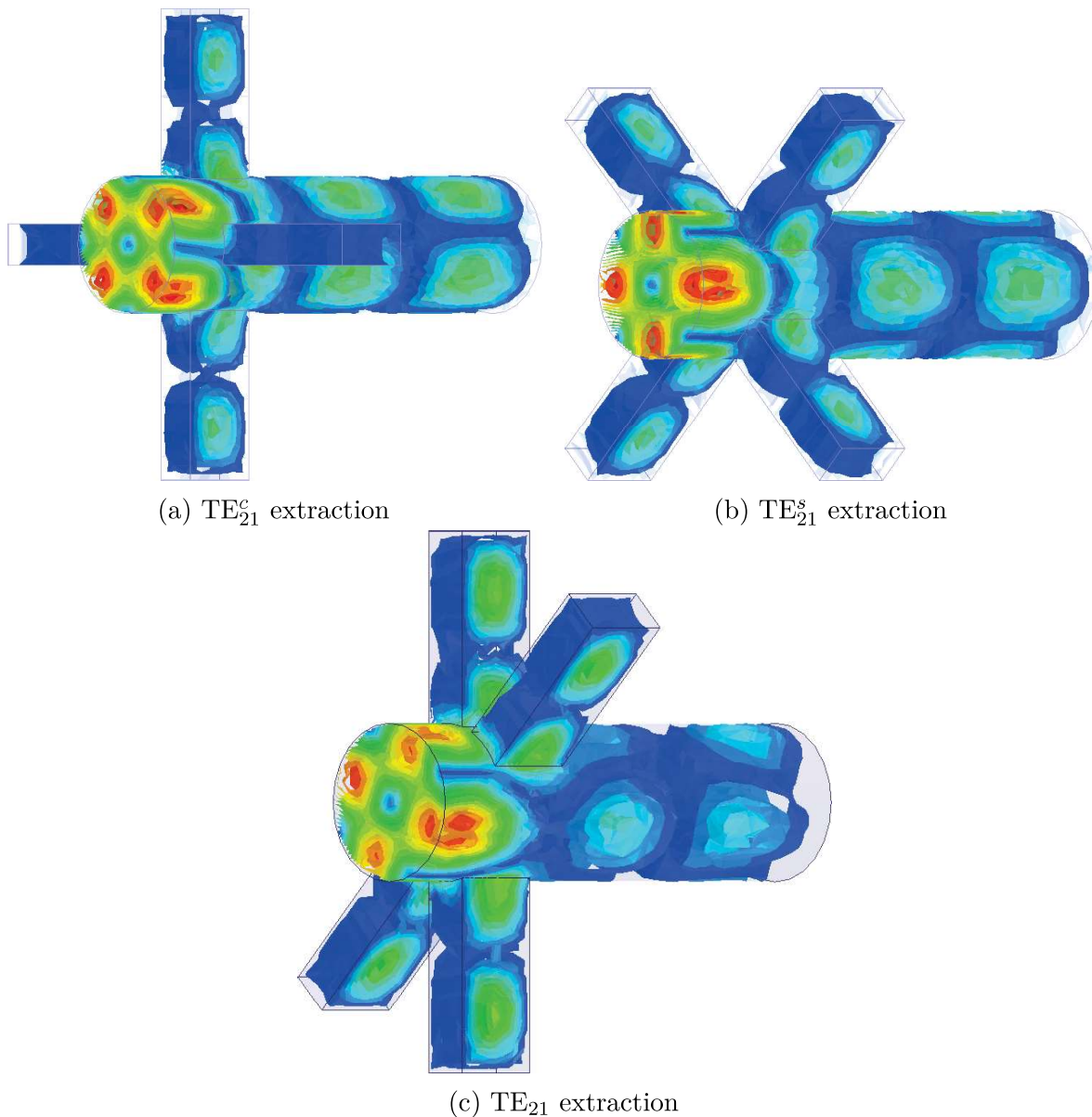


Figure 1.17: Example of 4-port TE_{21} extractors

1.4.1.3 8-way coupler

To simultaneously extract both the TE_{21}^c and the TE_{21}^s modes, an 8-way coupler can also be used as shown in Fig. 1.18. This coupler is the combination of two 4-way couplers one rotated of 45° respect to the other and each pair of four slots extract a single TE_{21} mode. Technical properties are the same as the ones described before. To recover all the energy is needed a coupling coefficient of -6 dB for each slot.

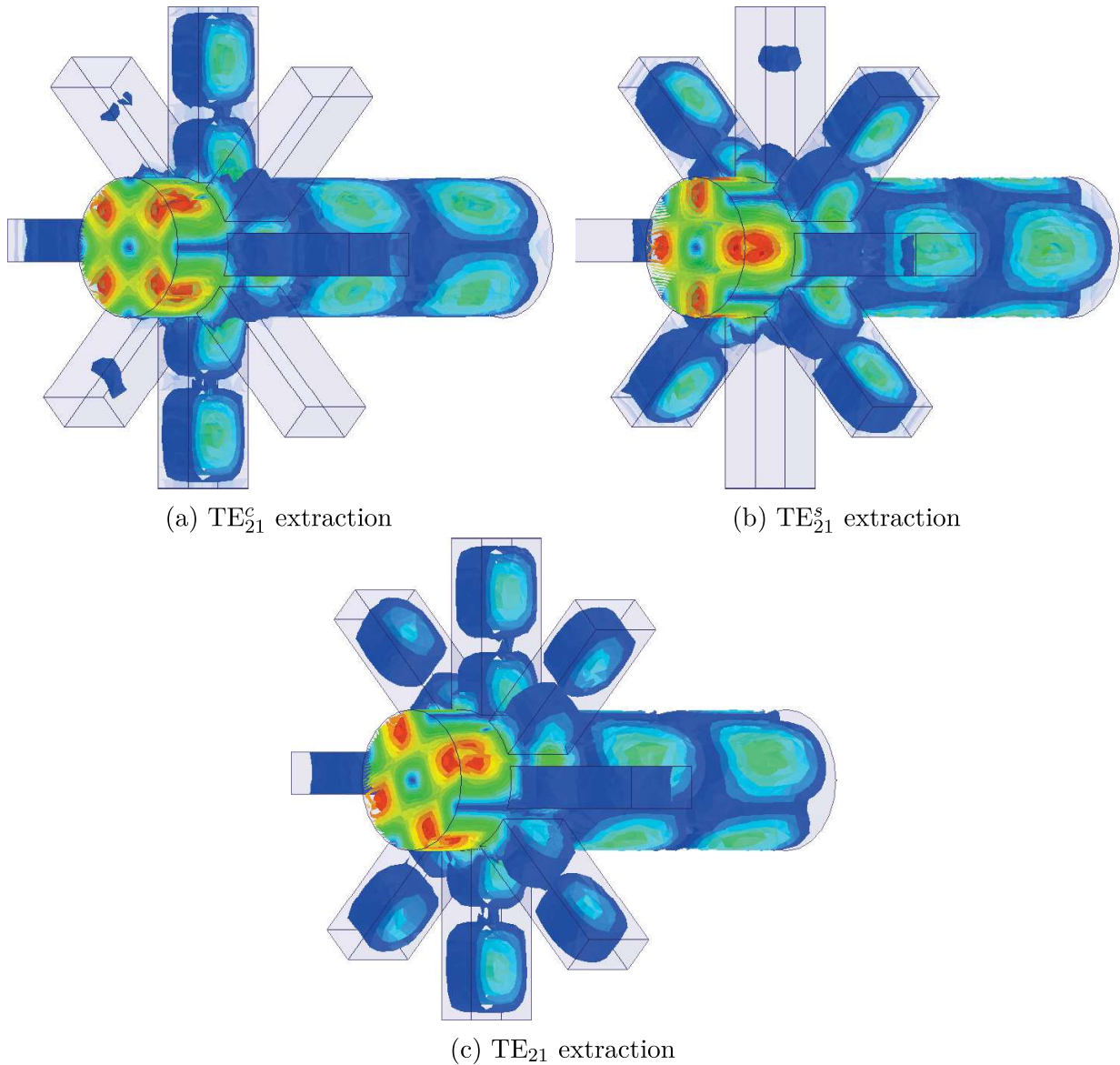


Figure 1.18: Example of 8-port TE_{21} extractors

1.4.2 Combining Network

Modes extracted through the mode coupler, need to be coupled inside all the waveguide circuitry that builds SUM and DELTA signals as well as post-processing components installed that make the monopulse system work.

To do this, a combining network is used to combine in the correct way fields that would be extracted through coaxial probes or waveguides connecting mode couplers to components like septum polarizers, hybrid couplers, orthomode transducers, filters, matched loads and amplifiers.

1.4.2.1 Septum Polarizer

To separate left-hand and right-hand polarizations (LHCP and RHCP) as well as generate linear polarizations, is using a septum polarizer. It is a four-port passive device consisting in a rectangular waveguide (sometimes circular-to-rectangular waveguide transitions are required) and a step-shaped metal wall that progressively divides the rectangular waveguide into two separated waveguides.

To explain how it works, in Fig. 1.19 is presented this component divided in four sections S_0, S_1, S_2, S_3 , and the TE_{10} excited in the input port IN that generates an horizontally linearly polarized field (i.e. $E = \hat{x}E_0$). The field distribution is represented in Figure 1.20. As the electric field propagates through the component, encounters the metallic wall that gradually changes the field orientation. Because a linear polarized field has been choose for the example, the field ad the output ports OUT_1, OUT_2 will be still linearly polarized but the output power will be half of the input power. Septum polariser can be engineered so that a 90° relative phase difference at one port and -90° at the other port relative can be established between the vertical and horizontal polarization outputs.

With the same approach, it is possible to separate also LHCP and RHCP.

The EM model to describe a septum polarizer is trough the scattering matrix 1.6.

$$\mathbf{S} = \frac{1}{\sqrt{2}} \begin{bmatrix} S_{11} & S_{12} & S_{13} & S_{14} \\ S_{21} & S_{22} & S_{23} & S_{24} \\ S_{31} & S_{32} & S_{33} & S_{34} \\ S_{41} & S_{42} & S_{43} & S_{44} \end{bmatrix} = \frac{1}{\sqrt{2}} \begin{bmatrix} 0 & 0 & 1 & 1 \\ 0 & 0 & -j & j \\ 1 & -j & 0 & 0 \\ 1 & j & 0 & 0 \end{bmatrix} \quad (1.6)$$

Calling OUT_1 the LHCP port and OUT_2 the RHCP output of the septum, will result the same field distribution with amplitude divided in half and opposite phase.

Taking for example the left-hand circular polarized field definition, $E = \frac{E_0}{\sqrt{2}}(\hat{y} - j\hat{x})$, it results

$$OUT_1 : -j\frac{E_0}{\sqrt{2}} - j\frac{E_0}{\sqrt{2}} = -jE_0$$

$$OUT_2 : j\frac{E_0}{\sqrt{2}} - j\frac{E_0}{\sqrt{2}} = 0$$

The opposite for a right-hand circular polarization.

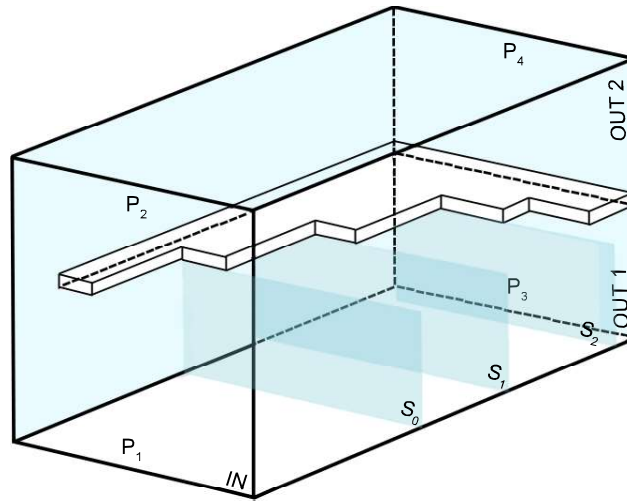


Figure 1.19: Transversal view of a septum polarizer

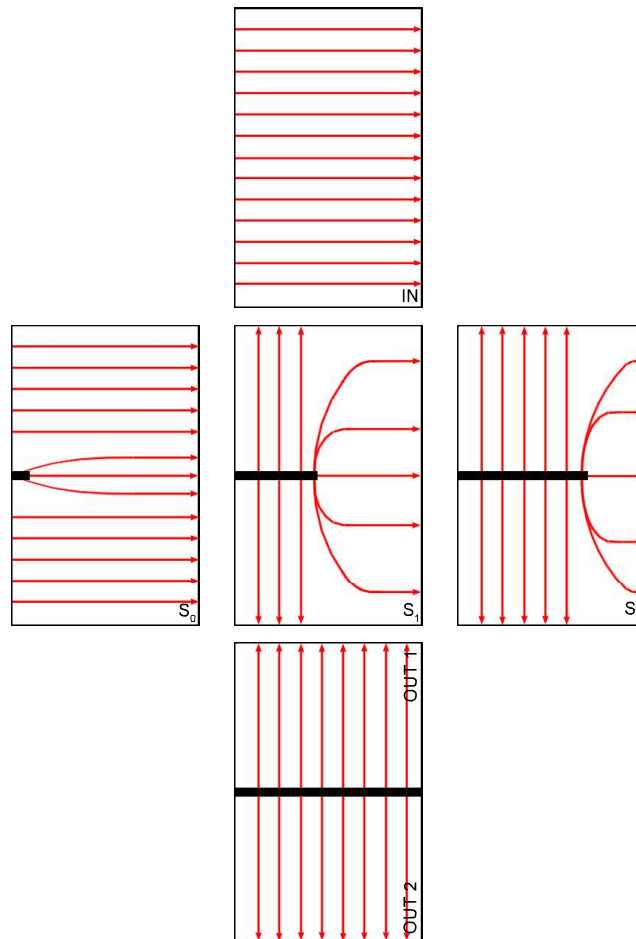


Figure 1.20: Schematic representation of the E-field distribution inside a septum polariser at different cross-section along the metal septum

1.4.2.2 3 dB/90° Hybrid Coupler

To generate DELTA signal, the extracted HOMs needed must be combined and the typical component used is a 3 dB/90° hybrid coupler (as shown in Fig. 1.21) that combines the input signal (the extracted TE₂₁ modes) with a 90-degree phase shift the one to another with a very high isolation ($S_{12} = 0$, $S_{23} = 0$). The typical S-matrix is shown in Eq. 1.7.

It can be schematized as a 4-port with each pair connected in a crossed way by a quarter-wavelength transmission line. The obtained signal at the output is used by the tracking receiver described in Chapter 1.2 generating the DELTA signal and the signals to control antenna' servos.

Hybrid couplers are used to separate right-hand and left-hand circular polarization into two separate channel and also to maximise the coupled extracted signal. This component, in fact, it is not necessary in the case of linear polarization because the signal coupling would be exactly the same at both output ports and with an amplitude 3 dB lower. For this reason, hybrid coupler it is suggested to be installed only when circular polarisation is used.

$$\mathbf{S} = -\frac{1}{\sqrt{2}} \begin{bmatrix} S_{11} & S_{12} & S_{13} & S_{14} \\ S_{21} & S_{22} & S_{23} & S_{24} \\ S_{31} & S_{32} & S_{33} & S_{34} \\ S_{41} & S_{42} & S_{43} & S_{44} \end{bmatrix} = -\frac{1}{\sqrt{2}} \begin{bmatrix} 0 & 0 & 1 & j \\ 0 & 0 & j & 1 \\ 1 & j & 0 & 0 \\ j & 1 & 0 & 0 \end{bmatrix} \quad (1.7)$$

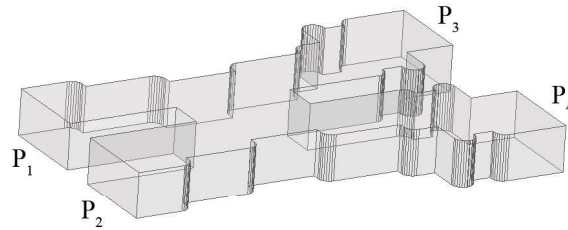


Figure 1.21: Hybrid Coupler schema

1.4.2.3 Magic-Tee

A classical component that is used to combine signals is Magic-Tee also known as 3 dB/0 – 180° hybrid coupler [6] (shown in Fig. 1.22), consisting in a four ports, where port P_1 and port P_2 are the two inputs, while port P_3 and P_4 are the two outputs. P_3 is also known as sum port Σ while P_4 is known as delta port Δ . It is designed in such way that TE_{10} mode is excited and exploiting the even symmetry, Σ and Δ port are completely decoupled the one to another. The same happens considering all the other couple of ports: ports P_1/P_2 and P_3/P_4 are completely decoupled.

Coupling between port P_4 with ports P_2 and P_3 is equal in amplitude but with a 180° phase shift, and this explains why the name of the two ports. Given two signals entering in port P_1 and P_2 , is possible find at port P_3 the sum of the two input signals, while at port P_4 the difference between the two.

In order to work properly, matching is needed inside the structure. This allows to achieve $S_{11} = S_{44} = 0$; then, in order to be lossless, also $S_{22} = S_{33} = 0$. According to this convention, the scattering matrix is shown in Eq. 1.4.2.3

$$\mathbf{S} = -\frac{1}{\sqrt{2}} \begin{bmatrix} S_{11} & S_{12} & S_{13} & S_{14} \\ S_{21} & S_{22} & S_{23} & S_{24} \\ S_{31} & S_{32} & S_{33} & S_{34} \\ S_{41} & S_{42} & S_{43} & S_{44} \end{bmatrix} = -\frac{1}{\sqrt{2}} \begin{bmatrix} 0 & 0 & 1 & 1 \\ 0 & 0 & 1 & -1 \\ 1 & 1 & 0 & 0 \\ 1 & -1 & 0 & 0 \end{bmatrix}$$

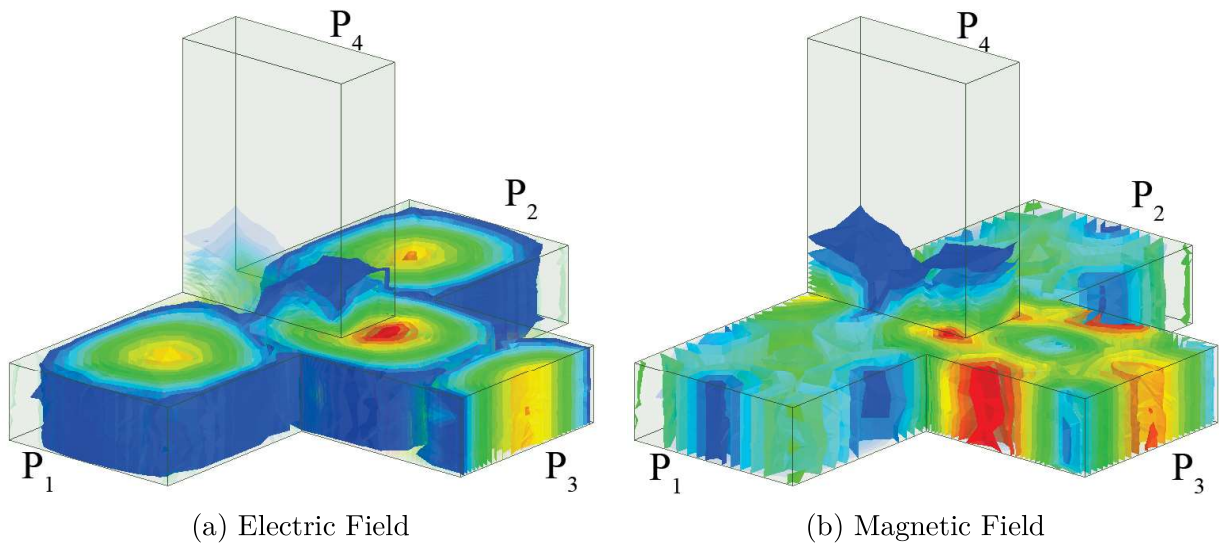


Figure 1.22: Magic-Tee

1.5 Example of Combining Networks

To extract TE_{11} modes for SUM signal is quite simple: is possible connect the wider-to-narrower transition (Fig. 1.14) to discard HOMs and a septum polariser at the output of the circular transition to separate left-hand from right-hand circular polarization (while the same result at the septum output will be obtained in case of a linear polarization). On the other side, for the DELTA signal a network might be needed to combine each output slots in the correct way, typically using hybrid couplers.

A simply 2-way mode coupler, no needs couplers to extract DELTA signal, because it is possible to connect directly outputs of the mode coupler to the $90^\circ/3dB$ hybrid coupler input ports.

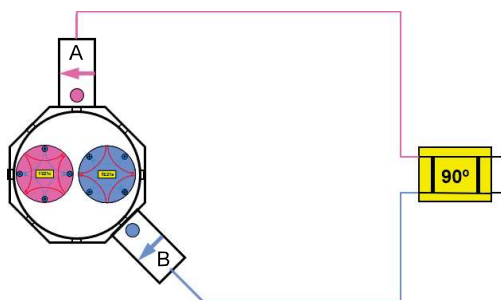


Figure 1.23: 2-port combining network

Complex network is required in case of a larger number of extracting slots and the complexity depends on the mode coupler used.

For example taking into account that TE_{11}^c , TE_{11}^s , TM_{01} , TE_{21}^c , TE_{21}^s and TE_{01} are excited in the circular core of a mode coupler in Fig. 1.24 a will have a combining network as follow to extract the TE_{21}^c mode:

$$\begin{aligned} U + D &\Rightarrow TE_{01}, TE_{11}^s \text{ and } TE_{21}^c \text{ survive} \\ R + L &\Rightarrow TE_{01}, TE_{11}^s \text{ and } -TE_{21}^c \text{ survive} \end{aligned}$$

$$(U + D) - (R + L) \Rightarrow TE_{21}^c$$

Where U, D, L, R are the four extracting slots.

The same can be done using the configuration in Figure 1.24b to extract the TE_{21}^s mode:

$$\begin{aligned} U + D &\rightarrow TE_{01}, TE_{11}^c \text{ and } TE_{21}^s \text{ survive} \\ R + L &\rightarrow TE_{01}, TE_{11}^c \text{ and } -TE_{21}^s \text{ survive} \end{aligned}$$

$$(U + D) - (R + L) \Rightarrow TE_{21}^s$$

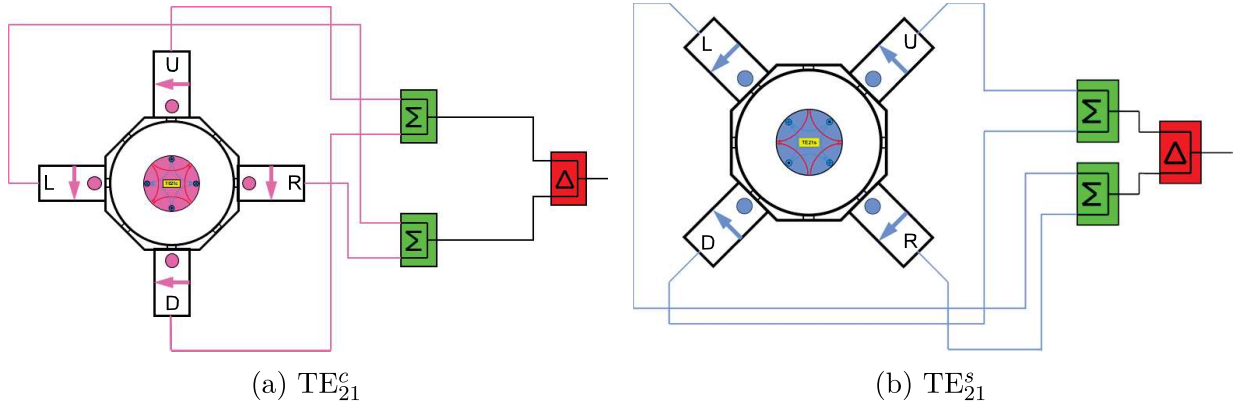
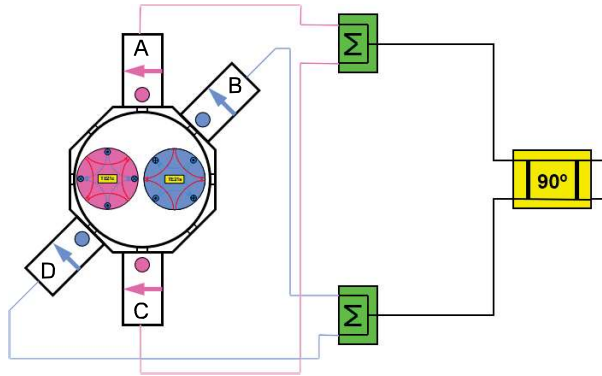


Figure 1.24: 4-port combining network

To extract both TE_{21}^s and TE_{21}^c at the same time using an asymmetric 4-port mode coupler in Fig. 1.25, the combining network will be described with Eq. 1.8.

$$\begin{cases} (A + C) \Rightarrow TE_{21}^c \\ (B + D) \Rightarrow TE_{21}^s \end{cases} \quad (1.8)$$

Where slots A and C will extract the TE_{21}^c and slots B and D will extract the TE_{21}^s .


 Figure 1.25: 4-way combining network for TE_{21}^c and TE_{21}^s

The same reasoning can be followed for the extraction through an 8-way mode coupler and are described with Eq. 1.9 and Eq. 1.10. Fig. 1.26 shows the recombining network: slots A, C, E, G will extract TE_{21}^c while slots B, D, F, H will extract TE_{21}^s

$$\begin{cases} (A - C) + (G - E) \Rightarrow TE_{21}^c \\ (H - B) + (D - F) \Rightarrow TE_{21}^s \end{cases} \quad (1.9)$$

$$\begin{cases} (A + E) - (C + G) \Rightarrow TE_{21}^c \\ (B + F) - (H + D) \Rightarrow TE_{21}^s \end{cases} \quad (1.10)$$

The two sets of recombinations are two ways to obtain the same result. Eq. 1.9 describes the 90° recombination, while Eq. 1.10 describes the 180° recombination and the reason why there exist these two kind of network is just for a design point of view. When the space surrounding the extractor is limited, is possible to choose the more convenient configuration.

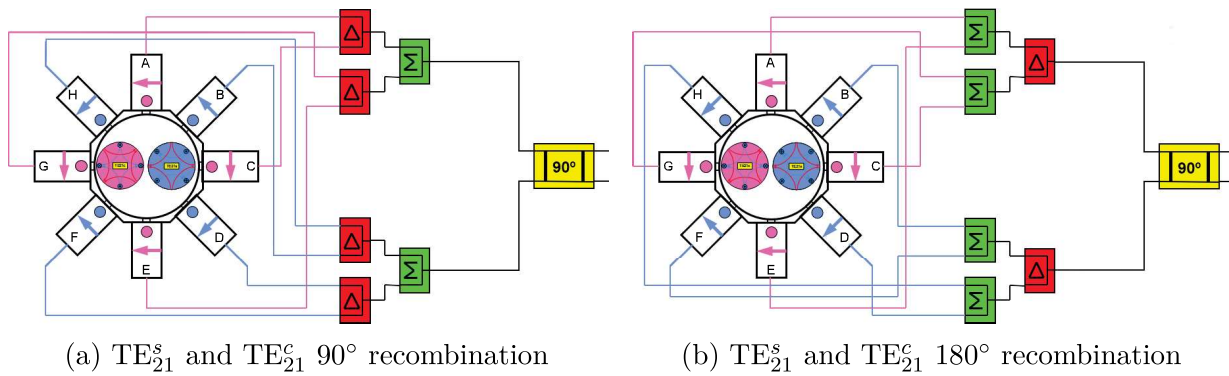
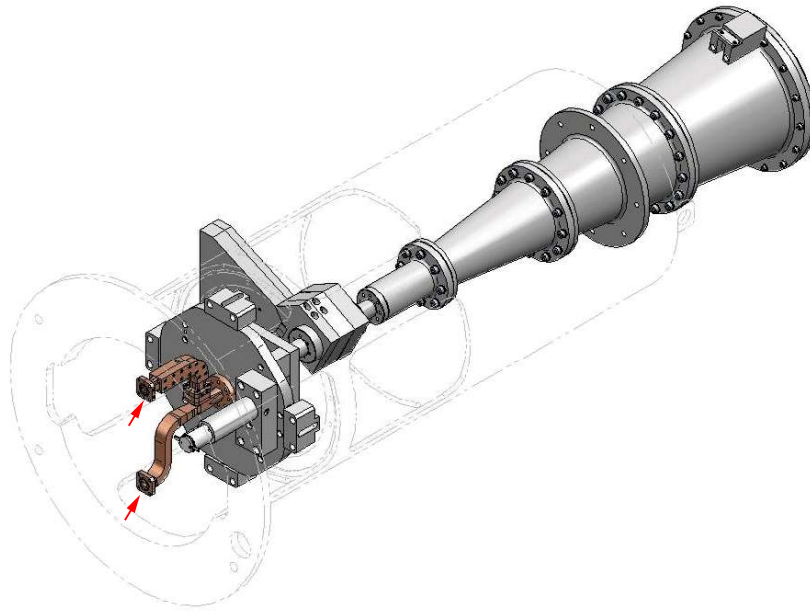
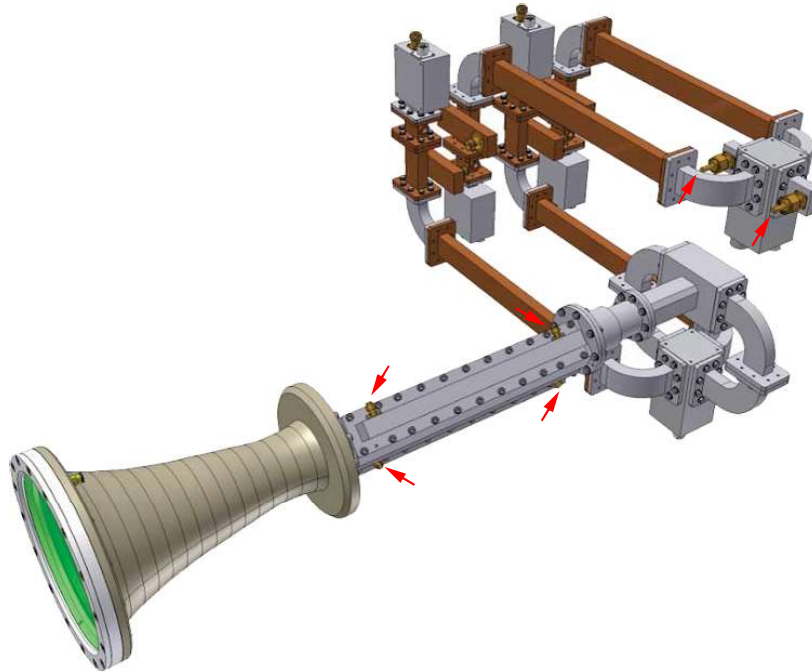


Figure 1.26: 8-port combining network

Connections between mode coupler to the rest of the system can be done either through waveguide or coaxial cable (rigid or flexible). The advantage using waveguide is that the signal is perfectly shielded and no external signals will interfere with it, but the problem is the space needed, therefore might be not a good choice in case of limited space available. On the other hand, coaxial cables do not give this problem because even complex connection can be done in case of limited space, but as a consequence the shielding from external interference is not perfect. Wrong matching or imperfect pin connection can introduce noise in the system and generate de-pointing problems.



(a) Waveguide Extraction [7]



(b) Coaxial Extraction [8]

Figure 1.27: Example of a mode extraction network of an ESA' system

References

- [1] "Ieee standard letter designations for radar-frequency bands", *IEEE Std 521-2002 (Revision of IEEE Std 521-1984)*, pp. 1–10, 2003. DOI: 10.1109/IEEESTD.2003.94224.
- [2] M. Richards, J. Scheer, J. Scheer, and W. Holm, *Principles of Modern Radar: Basic Principles, Volume 1*, ser. Electromagnetics and Radar. Institution of Engineering and Technology, 2010, ISBN: 9781891121524.

- [3] W. Melvin and J. Scheer, *Principles of Modern Radar: Radar Applications, Volume 3*, ser. Electromagnetics and Radar. Institution of Engineering and Technology, 2013, ISBN: 9781891121548.
- [4] S. Sherman and D. Barton, *Monopulse Principles and Techniques*, ser. Artech House radar library. Artech House, 1984, ISBN: 9781608071753.
- [5] Y. Choung and K. G. R, *Wide-band microwave signal coupler*, US Patent 4566012, 1986.
- [6] R. Collin, *Foundations for Microwave Engineering*, ser. McGraw-Hill electrical and electronic engineering series. McGraw-Hill, 1966, ISBN: 9780070118010.
- [7] S. S. a division of CALIAN Ltd., Ed., *Esa ds3 35m deep space antenna - design report, doc. no.: 129226 (technical document software manual)*, SED Systems a division of CALIAN Ltd., 2010.
- [8] A. (G. SE), Ed., *Documentation of 15 meter s/x band antenna, kourou, volume 10a, xaa system manual (technical document software manual)*, Astrium (Airbus Group SE), 2010.

2

Monopulse In-Lab Calibration System

Before its operational use, a monopulse antenna need to be calibrated through a well known target [1], where the signal source (i.e. a horn antenna or other kind of antennas) is mounted on a tall structure in the far-field region of the measured antenna (see Fig. 2.1). Hence, the name, calibration tower. Also satellites are used in some cases [2] performing a differential measurement between the transmitted and received signal from both antenna and spacecraft.

In the far-field region, the wavefront curvature produced by the source, becomes more planar over the antenna under test. Outdoor measurements might result the simplest way to test a space antenna due to its size (diameters can swing between few meters to tens of meters), but environmental conditions are critical factors; precipitations, humidity, wind and temperatures are the most critical points especially because most of the used antennas for space applications are installed in locations with rigid weather conditions (poles and equator latitudes mainly). Snow, storms, temperature, wind and humidity might have a big impact on these kind of measurements. Also terrain morphology need to be considered since obstacles may cause reflection, introducing the problem of multi path (Fig. 2.2), increasing the measurement errors and other uncertainties.

Measurements with a calibration tower requires two main operations: the first one is that the entire monopulse tracking chain must be installed on the antenna; the second one, in particular, if the antenna is already fully operational, it must be put downtime as long as the calibration procedure is completed.

These operations must be done every time a component of the tracking chain is changed to upgrade the antenna's characteristics (i.e. increase bandwidth or modify working frequency) or re-designed due to components not fully compatible. Both operation are expensive especially because during this period, the antenna it is not working for its commercial purposes.

To minimize these operations a novel setup has been designed allowing in-lab measurements on a bench test the entire tracking chain, without mounting it on the antenna to test it.

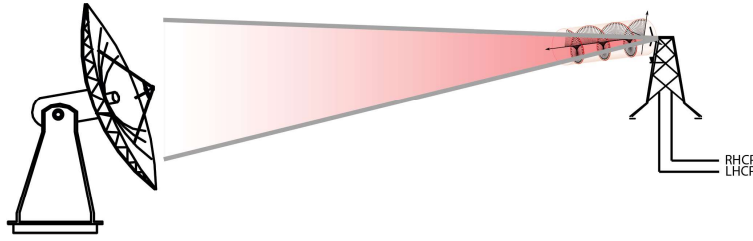


Figure 2.1: Calibration Tower

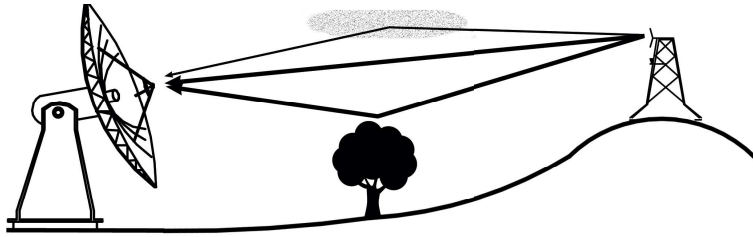


Figure 2.2: Multipath

2.1 Monopulse In-lab Bench Test

It consists on a simple multi-modal source generator for the monopulse tracking chain made with an overmoded circular waveguide (OCWG) component with offset sections. With this setup it is possible to prevent the use of expensive systems to calibrate the monopulse, by mimic in-lab its behaviour and eventually correct in advance possible designing errors that may lead to problems in the tracking system once installed on the antenna. The most common problem is the de-pointing that occurs when SUM and DELTA signals are not aligned (meaning that the maximum of the SUM signal is not aligned with the minimum of the DELTA). In this situation the antenna may track a target (calibration tower or a spacecraft) a in a wrong position with respect to the real one.

This waveguide junction is excited with the degenerate fundamental TE_{11} mode to properly excite amplitude and phase difference of the desired HOMs that are used for tracking purposes. Unlike many works reported in the literature that describe the conversion between two modes in the same circular waveguides [3] - [4], this work does not convert one mode to another without phase control, but aims to excite many high order modes (the ones needed for tracking purposes) controlling their amplitude and phase in a very precise way.

The proposed system is based on a offset-junction [5] [6] [7] between two waveguides of radius R large enough to allow the propagation of HOMs as shown in Fig. 2.3. As long as the two waveguides are collinear (their propagation axis is aligned), high order modes are not excited. As the symmetry is broken with a shift offset M_o with respect to the axis of the input waveguide, along the angular direction ϕ (Fig. 2.3), HOMs are generated. Depending on the radius and the operational frequency band, a circular waveguide can propagate HOMs up to a determined cutoff frequency f_c which is related to the zeroes of the Bessel functions. Two cascaded OCWGs with the same diameter but aligned in such way that their propagation axis is non-collinear (Fig. 2.3a), HOMs at port P_2 (such as TM_{01} , TE_{21} , TE_{01} , ... shown in Fig. 1.9) are generated, by feeding the input port P_1 with the fundamental TE_{11} modes. In particular, amplitude and phase difference of the HOMs with respect to the TE_{11} modes can

be controlled by changing the magnitude of M_o for the amplitude and the angular position ϕ of the offset respectively.

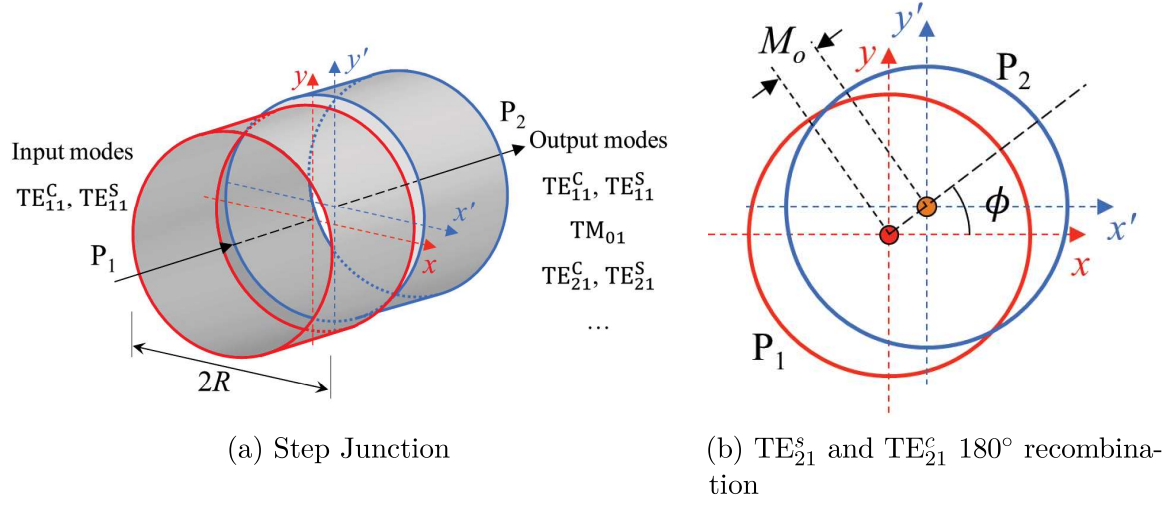


Figure 2.3: Step Junction

The firsts HOMs (the TM_{01} , the two degenerated TE_{21}^C , and TE_{21}^S , and the TE_{01}) exhibit a null in their radiation pattern at the boresight direction, which is convenient for tracking purposes, but the pattern of their respective electric (\mathbf{E}) and magnetic (\mathbf{H}) fields is radically different. This last aspect will determine the HOMs' phase difference evolution, with respect to the fundamental modes $TE_{11}^{C/S}$, as well as the way of extracting this information through a waveguide HOMs coupler (as explained in Chapter 1.4.1). Adopting a waveguide radius that allows the propagation at least up to the TE_{01} mode, it is evident that when the offset M_o is rather low, independently from the rotation angle ϕ , the two degenerate fundamental modes TE_{11}^C and TE_{11}^S will be fully transmitted ($|S_{21}| \approx 1$). Furthermore, the coupling parameter S_{21} relating the fundamental mode and an excited high order mode ($S_{21}(\text{HOMs}, TE_{11})$) will be very small, becoming zero if $M_o = 0$. By increasing the value of M_o , HOMs are inexorably generated and their excitation level should increase with M_o .

2.1.1 Excitation Coefficient High Order Modes

The theoretical determination of the phase difference ψ between any excited HOM and the incoming fundamental TE_{11} mode as a function of ϕ can be easily derived by inspection using their respective \mathbf{E}/\mathbf{H} patterns in a circular waveguide. The first HOM to be considered is the TM_{01} . As shown in Fig. 1.9, this mode has a radial \mathbf{E} field in any transversal section (orthogonal to the transversal azimuthal pattern of the \mathbf{H} field). If the incident TE_{11}^C fundamental mode (where its \mathbf{E} field is oriented in the vertical direction) reaches the discontinuity of an OCWG with a given offset magnitude and a rotation of $\phi = 0^\circ$ or $\phi = 180^\circ$ (offset along positive or negative x axis), the TM_{01} mode cannot be excited, due to the fact that TE_{11}^C and TM_{01} modes have opposite symmetry in the xz plane (odd for TE_{11}^C and even for TM_{01}). On the contrary, if the offset angle ϕ is exactly 90° or 270° (offset along the positive/negative y axis) the excitation level $K_{TM_{01}}$ of the TM_{01} mode will be the maximum attainable for an offset magnitude M_o . Furthermore, the normalized phase difference $\psi_{TM_{01}}$ between the fundamental mode TE_{11}^C and the excited mode TM_{01} varies from $\psi_{TM_{01}} = 180^\circ$

for $\phi = 90^\circ$ to $\psi_{\text{TM}_{01}} = 0^\circ$ for $\phi = 270^\circ$. This means that any offset deviation in the y-direction implies a jump of the phase $\psi_{\text{TM}_{01}}$ of 180° while an offset deviation in the x-direction does not affect the system. It is possible to conclude that for any other ϕ rotation, the TM_{01} magnitude is proportional to $|\sin(\phi)|$ while the phase difference $\psi_{\text{TM}_{01}}$ follows the general rule discussed before. This situation is clearly shown in Fig. 2.4 where the excitation coefficients of HOMs are given for both the incident fundamental modes (TE_{11}^C and TE_{11}^S) at different offset angles ϕ .

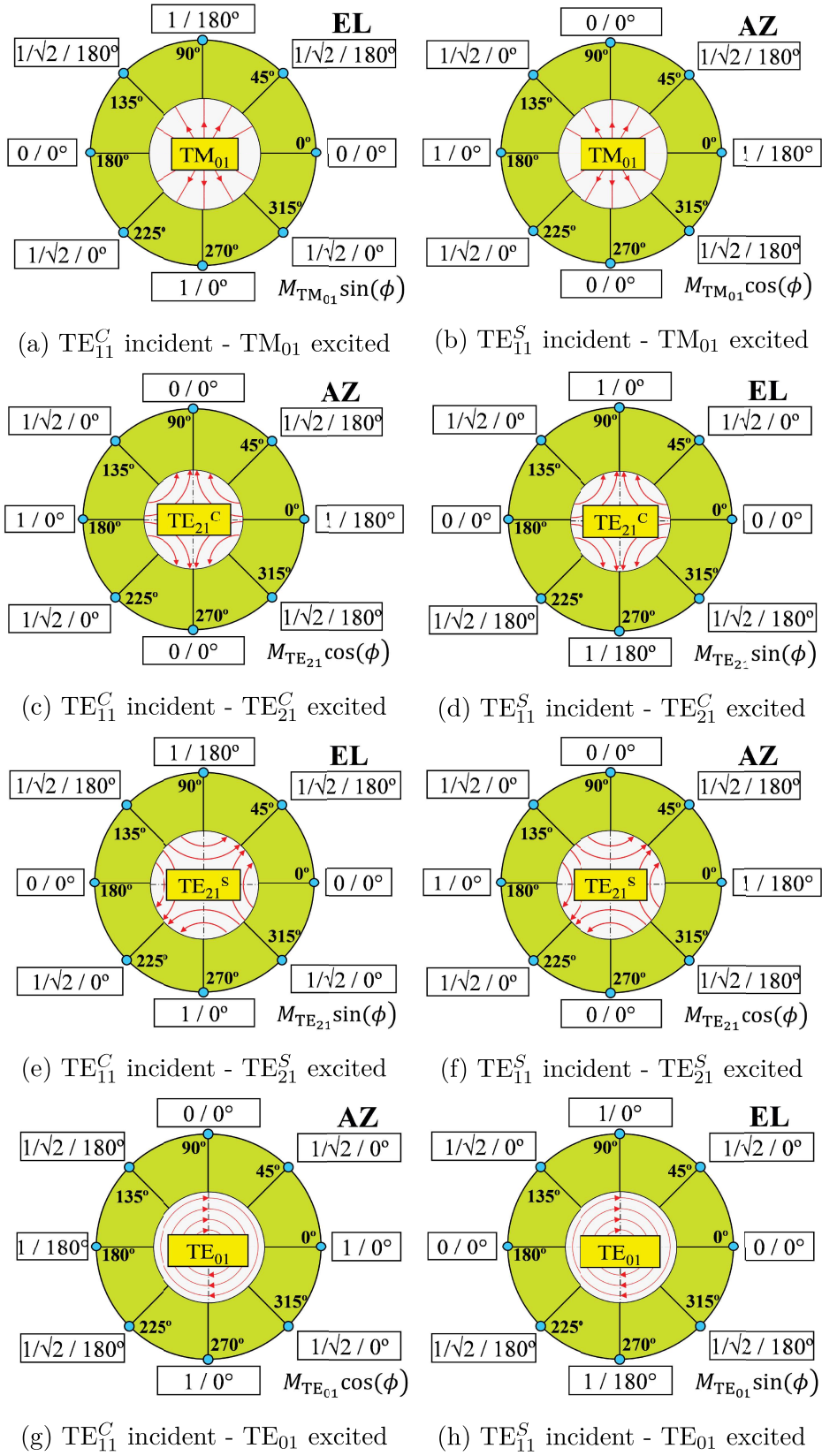


Figure 2.4: Excitation coefficients of HOMs for a given incident fundamental mode (TE_{11}^C or TE_{11}^S) at different offset angles ϕ

Table 2.1: Amplitude and phase of the HOMs when excited by a given incident fundamental mode. Depending on the coupling, the HOM provides sensitivity for elevation (EL) or azimuth (AZ) antenna depointing.

Incident	HOM	Amplitude M	Phase Ψ	Sensitivity
TE_{11}^C	TM_{01}	$M_{TM_{01}} \sin\phi$	$\{1 + \text{sign}[\sin(\phi)]\} \frac{\pi}{2}$	EL
TE_{11}^C	TE_{21}^C	$M_{TE_{21}} \cos\phi$	$\{1 + \text{sign}[\cos(\phi)]\} \frac{\pi}{2}$	AZ
TE_{11}^C	TE_{21}^S	$M_{TE_{21}} \sin\phi$	$\{1 + \text{sign}[\sin(\phi)]\} \frac{\pi}{2}$	EL
TE_{11}^C	TE_{01}	$M_{TE_{01}} \cos\phi$	$\{1 + \text{sign}[\cos(\phi)]\} \frac{\pi}{2}$	AZ
TE_{11}^S	TM_{01}	$M_{TM_{01}} \cos\phi$	$\{1 + \text{sign}[\cos(\phi)]\} \frac{\pi}{2}$	AZ
TE_{11}^S	TE_{21}^C	$M_{TE_{21}} \sin\phi$	$\{1 + \text{sign}[\sin(\phi)]\} \frac{\pi}{2}$	EL
TE_{11}^S	TE_{21}^S	$M_{TE_{21}} \cos\phi$	$\{1 + \text{sign}[\cos(\phi)]\} \frac{\pi}{2}$	AZ
TE_{11}^S	TE_{01}	$M_{TE_{01}} \sin\phi$	$\{1 + \text{sign}[\sin(\phi)]\} \frac{\pi}{2}$	EL

In general, the excitation coefficients of the HOMs can be defined as the complex ratio

$$K_{HOM}^C = \frac{S_{21_{HOM, TE_{11}^C}}}{S_{21_{TE_{11}^C, TE_{11}^C}}} = M_{HOM} \sin(\phi) e^{j\Psi_{HOM}} \quad (2.1)$$

$$K_{HOM}^S = \frac{S_{21_{HOM, TE_{11}^S}}}{S_{21_{TE_{11}^S, TE_{11}^S}}} = M_{HOM} \cos(\phi) e^{j\Psi_{HOM}} \quad (2.2)$$

It is possible to obtain the amplitude M_{HOM} and phase difference Ψ_{HOM} required to mimic the values retrieved by a monopulse system as if it would be tracking a real spacecraft. In particular, in case the HOM considered is the TM_{01} , the equations could be divided as follow

$$S_{21}(TM_{01}, TE_{11}^C) = M_{TM_{01}} \sin(\phi) \quad (2.3)$$

$$\Psi_{TM_{01}} = \{1 + \text{sign}[\sin(\phi)]\} \frac{\pi}{2} \quad (2.4)$$

The same considerations could be used if the incident fundamental mode is the TE_{11}^S . In this case, the excitation of the TM_{01} mode is proportional to $|\cos\phi|$ with exactly the same amplitude level $M_{TM_{01}}$

$$S_{21}(TM_{01}, TE_{11}^S) = M_{TM_{01}} \cos(\phi) \quad (2.5)$$

$$\Psi_{TM_{01}} = \{1 + \text{sign}[\cos(\phi)]\} \frac{\pi}{2} \quad (2.6)$$

From a practical point of view, and referring to the equivalence of Fig. 2.4, this means that taking into account the antenna axis coordinates system of a real tracking system, the TM_{01} excitation due to the fundamental TE_{11}^C mode is exclusively sensitive to the elevation pointing error (Δ_{EL}) while the excitation due to the fundamental TE_{11}^S mode is exclusively sensitive to the azimuth pointing error (Δ_{AZ}).

The same reasoning can be applied to the next HOMs, and the amplitude and phase results can be easily validated in any electromagnetic CAD tool. Table 2.1 summarizes this behaviour up to the TE_{01} mode. The two degenerated modes TE_{21}^C and TE_{21}^S always exhibit the same maximal amplitude $M_{TE_{21}}$ while their respective phase delay $\Psi_{TE_{21}}$ with respect to the fundamental modes are complementary.

2.1.2 Mathematical Model of the Step-Waveguide Junction

As the phase behaviour Ψ_{HOM} of the excited modes is already known for any value of the rotation angle ϕ , the correspondence between an arbitrary waveguide offset M_o and the resulting magnitude M_{HOM} for the different modes has to be established.

The frequency behaviour of the HOM excitations amplitudes' are similar to the frequency variation of the ratio λ_{gHOM}/λ_0 [8], where λ_{gHOM} is the guided wavelength for each individual HOM and λ_0 is the free space wavelength. Moreover, it can be demonstrated by simple electromagnetic simulations that an arbitrary variation of the offset magnitude in the OCWG circuit implies a linear variation of these excited levels with M_o , as long as M_o is not too large compared to the waveguide radius (e.g., $M_o < R/10$). Fig. 2.5 shows a simulation example for a Ku-band oversized circular waveguide. While the transmission for the fundamental modes TE₁₁ is almost perfect ($|S_{21}| \approx 0$ dB), HOMs excitations start at their respective cutoff frequencies and decrease smoothly with the frequency. Fig. 2.5 also shows the standard bandwidths used in a real tracking system where the so-called security guard is about 5 – 10% both close to the cutoff of the mode itself and to the cutoff of the next mode.

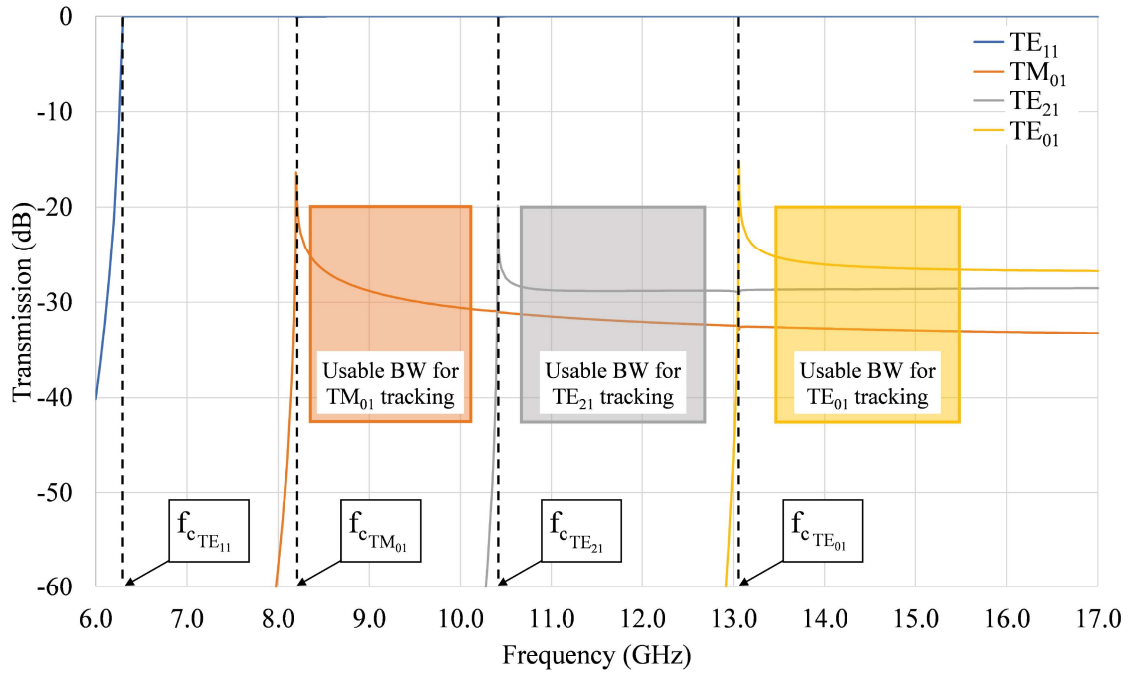


Figure 2.5: Behavior of the amplitude of the excitation coefficients of HOMs for an offset $M_o = 0.6$ mm in a circular waveguide with radius $R = 14$ mm.

Using the above reasoning, the excitation amplitude of a generic HOM with an incident fundamental mode TE₁₁ can be written as

$$|S_{21}(HOM, TE_{11})| = M_{HOM} = M_o \left[n \left(\frac{\lambda_{gHOM}}{\lambda_0} \right)^m + b \right] \quad (2.7)$$

where the optimal values of the coefficients m , n and b for each high order mode can be derived by using a simple conjugate-gradient fitting algorithm.

Since the behaviour of the excited magnitudes ($M_{TM_{01}}$, $M_{TE_{21}}$, $M_{TE_{01}}$) are mathematically known through Eq. 2.7 and the behaviour of their normalized phase shift ($\Psi_{TM_{01}}$, $\Psi_{TE_{21}^C}$,

Table 2.2: Optimized parameters for HOM mathematical model 2.3, considering a circular waveguide with radius of $R=14$ mm.

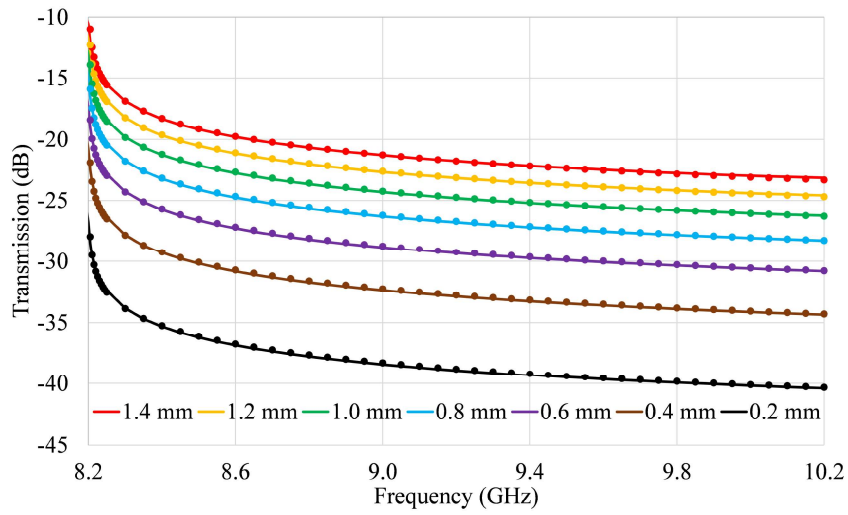
HOM	m	$n(\text{mm}^{-1})$	$b(\text{mm}^{-1})$
TM ₀₁	0.22972	0.13036	-0.09838
TE ₂₁	0.91575	0.00460	0.05974
TE ₀₁	0.96433	0.00565	0.06818

$\Psi_{\text{TE}_{21}^s}$, $\Psi_{\text{TE}_{01}}$) with respect to the fundamental modes is known through Table 2.1, it is possible to predict the excitation values of any HOM for a given offset set (M_o, ϕ) in an OCWG circuit. From Eq. 2.7 it is also possible to obtain the offset M_o for a desired excitation level of a specific HOM, corresponding to a desired tracking contour level (Fig. 2.8) at a given frequency by simply reverting the formula.

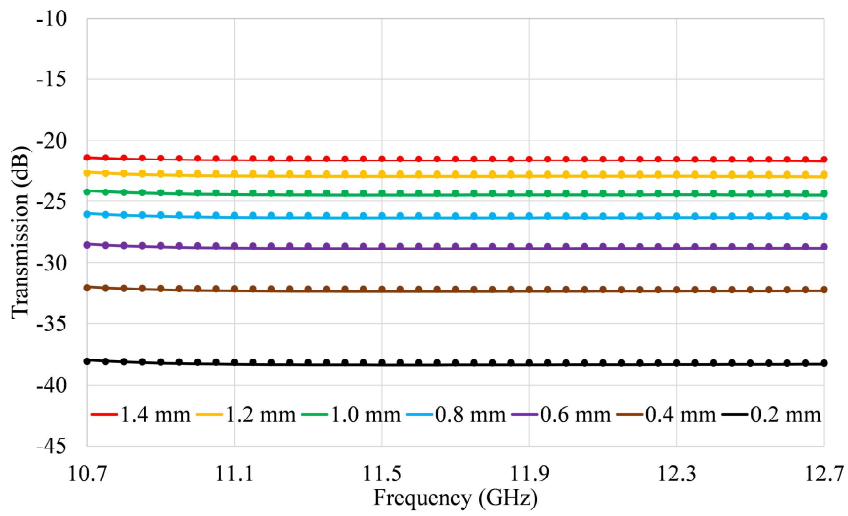
$$M_o = \frac{|S_{21}(\text{HOM}, \text{TE}_{11})|_{\text{desired}}}{n \frac{\lambda_{\text{HOM}}}{\lambda_0}^m + b} \quad (2.8)$$

Indeed, also the levels of all the undesired excited HOMs can be easily obtained. It is worth noting that the analytical model from Eq. 2.7 (and, consequently, Eq. 2.8) can be extended to any frequency range by using the waveguide radius as scaling factor.

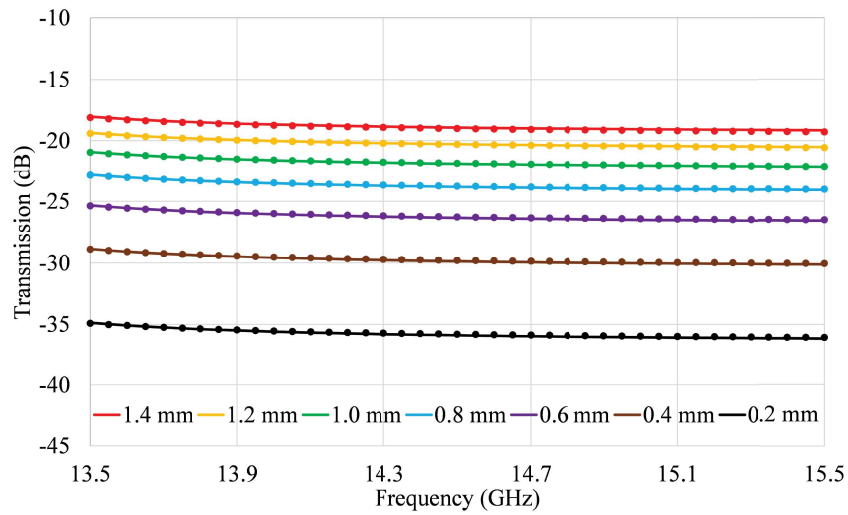
As an example, it is possible to retrieve the parameters m , n and b from the plots of Fig. 2.5 using the reverted Eq. 2.7 and results are shown in Table 2.2, assuming an offset $M_o = 0.6$ mm in a OCWG of radius $R=14$ mm. Afterwards, these coefficients have been used to determine the frequency behaviour of the OCWG under test, by varying the offset magnitude from $M_o = 0.2$ mm to $M_o = 1.4$ mm with a step of 0.2 mm. This has been simulated through HFSS and results are shown in Fig. 2.6. The excellent agreement can be observed for the three considered modes, with a maximum discrepancy of ± 0.3 dB.



(a) TM_{01} mode



(b) TE_{21} mode



(c) TE_{01} mode

Figure 2.6: Mathematical model 2.7 vs full-wave simulated results in a circular waveguide with radius $R=14$ mm. Curves refers to different values of the offset M_o



2.1.3 Simulated Modes Excitation from the Calibration Tower

To confirm the possibility to mimic the target position with this simple offset waveguide junction, we considered a tracking system based on a circular waveguide with a radius $R = 14$ mm and working at 12 GHz.

The link between two horn antennas has been simulated by HFSS, considering the structure shown in Fig. 2.7.



Figure 2.7: Structure considered to mimic the calibration tower.

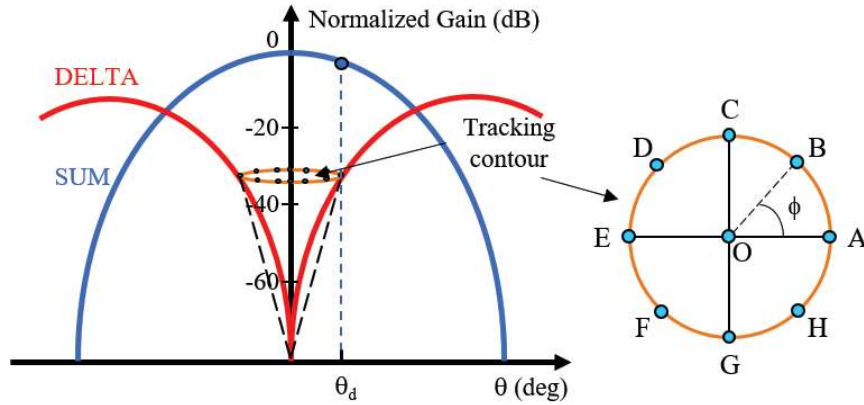


Figure 2.8: Normalized radiation pattern of the SUM and DELTA used in the monopulse system. (b) Calibration is typically performed inside the half-power beamwidth, using eight directions distributed on a circle.

Let assume to excite Port 1 with only the TE_{11}^C mode: to make the mode excitation in the receiving waveguide independent from the distance when considering the i th direction, the following normalization of the amplitude A and phase difference Ψ has been adopted.

$$A|_{dB} = S_{21}(m_2, TE_{11}^C)|_{dB,ith} - S_{21}(TE_{11}^C, TE_{11}^C)|_{dB,direction O} \quad (2.9)$$

$$\Psi = \angle S_{21}(m_2, TE_{11}^C)|_{ith} - \angle S_{21}(TE_{11}^C, TE_{11}^C)|_{ith} \quad (2.10)$$

where $S_{21}(m_2, TE_{11}^C)$ is the scattering parameter relating the TE_{11}^C excitation in Port 1 to any of the modes TE_{11}^C , TE_{11}^S , TE_{21}^C , TE_{21}^S , in Port 2, and direction O is the boresight direction shown in Fig. 2.8.

The same reasoning can be done exciting in Port 1 the TE_{11}^S mode. However, due to the symmetries of the geometrical structure and of the mode field patterns, amplitude and phase difference results can be retrieved directly from those with the TE_{11}^C excitation, just considering a rotation of 90° .

Running the simulation for all the eight positions and for the boresight direction O with

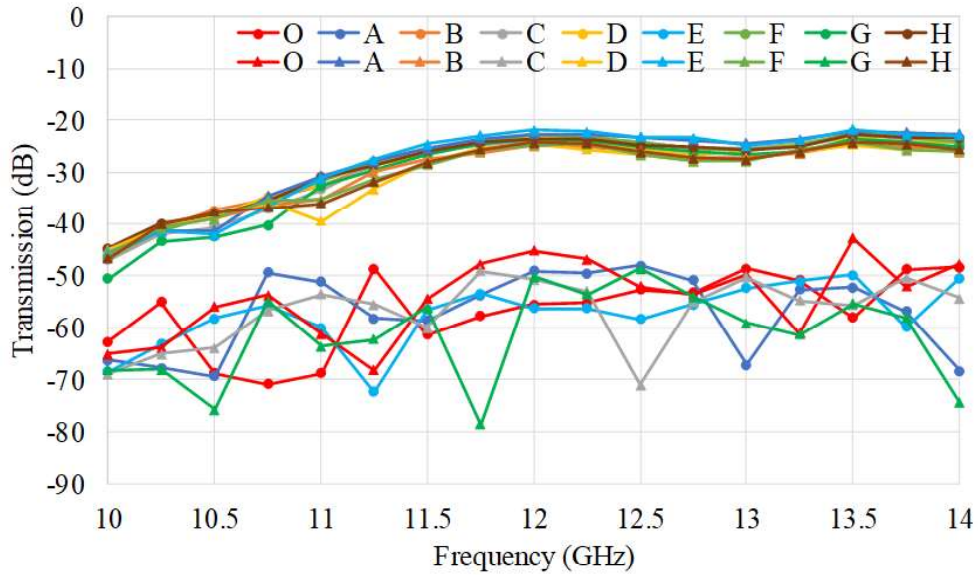
Table 2.3: Waveguide offset extracted using Eq. 2.2 at 12 GHz, when considering different antenna depointing angles for a circular waveguide with radius of $R=14$ mm and ϕ of 45° .

Depointing angle	$M_{TM_{01}}$	$M_{TE_{21}}$	$M_{TE_{01}}$	M_o (mm)
0.5°	-46.9	-42.6	-40.4	0.11
1°	-32.4	-30.7	-28.7	0.44
5°	-27.3	-22.5	-20.5	1.13

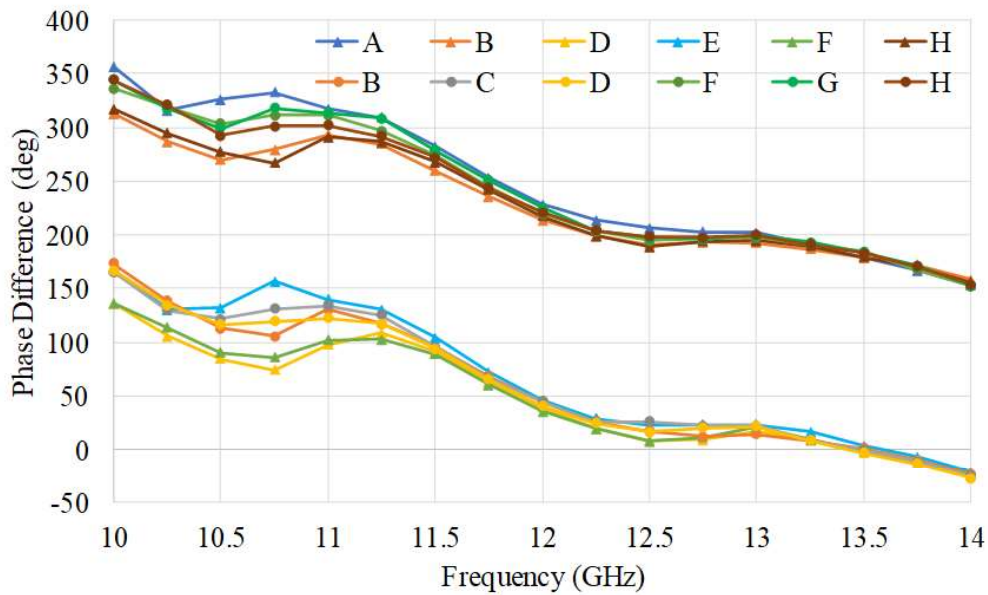
TE_{11}^C excitation on the TX side, Eq.2.9 and Eq. 2.10 are used to retrieve the results shown in Fig. 2.9. Both the amplitude [Fig. 2.9a] and phase [Fig. 2.9b] of TE_{21}^C and TE_{21}^S are plotted. For a given target misalignment θ_d with respect to boresight, the amplitude of Δ signal shows a given value compared to the maximum of Σ signal (in Fig. 2.8). Moreover, the phase difference between Σ and Δ signals has a precise value that normally swings between 0 and 180 degrees, depending on the HOM used and on the target position ϕ around the tracking contour (TC). From Fig. 2.9 it appears that, when the transmitted excitation is TE_{11}^C , the received TE_{21}^C mode is not excited at the boresight direction O as well as for A ($\phi = 0^\circ$) and E ($\phi = 180^\circ$) directions. On the contrary, the degenerated TE_{21}^S mode in RX, is not excited at the boresight O , and for C ($\phi = 90^\circ$) and G ($\phi = 270^\circ$) directions. This is not surprising, due to the symmetry of the structure. Moreover, it is notice that there is a 180° phase shift between directions that are symmetrically located with respect to the boresight direction.

Purposely introducing a depointing of 0.5° , 1° , and 5° with respect to the line-of-sight between the two simulated horn antennas, with a fixed rotational angle of $\phi = 45^\circ$ (point B in Fig. 2.8). The amplitudes of the TM_{01} , $TE_{21}^{S/C}$, TE_{01} HOMs due to the depointing in the circular waveguide of the receiving antenna are reported in Table 2.3 (columns $M_{TM_{01}}$, $M_{TE_{21}}$, and $M_{TE_{01}}$). It is noted that the above-mentioned amplitudes are normalized assuming as reference the excitation coefficients at Port 2 of Fig. 2.1 of the TE_{11}^C or the TE_{11}^S mode, when Port 1 in Fig. 2.1 is excited with the same mode. In this way, all the phase and amplitude changes due to the propagation effects and to the receiving antenna are cancel out.

From these values, using Eq. 2.8 and the coefficient m , n and b of Table 2.2, the offset M_o required to obtain the given excitations for the three HOMs have been calculated. The three values are practically coincident (within 1%), and their average value is reported in the last column of Table 2.3.



(a) Normalized amplitude between TE_{21}^C RX and TE_{11}^C RX (dots) and TE_{21}^S RX and TE_{11}^C RX (triangles)



(b) Phase difference between TE_{21}^C RX and TE_{11}^C RX (dots) and TE_{21}^S RX and TE_{11}^C RX (triangles)

Figure 2.9: Calculation of the modes excited in the RX waveguide when the link in Figure 2.1 is considered with TE_{11}^C excitation on Port 1.

2.2 Design of monopulse waveguide components

To properly validate the effectiveness of the OCWG, all the waveguide components of a monopulse tracking chain (transitions, 3dB/90° hybrid coupler, septum polarizer, OMTs and mode coupler) have been designed, simulated and measured. All the simulations have been performed at 12 GHz.

This analysis is important not only because it is necessary to have a proper working monopulse tracking chain, but also because all these components have a big effect on the resulting tracking signals. Electromagnetic analysis of the component have been performed with the EM simulator Ansys HFSS and Mician, and measurement campaign has been performed with network analyser. All the designed components are made of raw aluminium.

2.2.1 Circular-To-Circular Waveguide

Most of the circular components have been designed with a radius R of 14 mm to work in a 1 GHz-wide frequency band centred at 12 GHz. To properly excite these components with a commercial source generator, it is necessary to convert the designed radius to the standard one used in this frequency band, that is of 9.9 mm.

Aside from this reason, the second aim of this conversion from smaller to larger diameter (9.9 mm to 14 mm) it is needed because the standard components are designed to be mono modal, and therefore to allow the propagation of HOMs, larger waveguides are needed.

The mechanical connection has been done using a standard WR75 rectangular waveguide flanges and to perform all the measurements, ports are closed with designed matched loads. From Fig. 2.11 it is possible to notice a very good isolation (0 dB) with the fundamental TE_{11} modes and a good input matching (less than 35 dB) at port P_1 (the same at port P_2) in the band of interest (see Fig. 2.5). Discrepancies between simulations and measurements of the input matching is due to the manufacturing process and material used. Simulations of simple waveguide structure generate results close to the theoretical expected values, not achievable when manufactured.

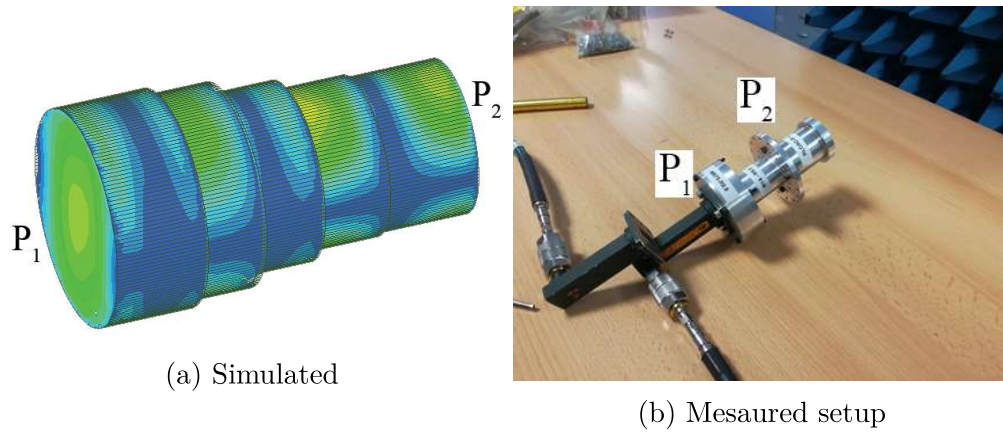


Figure 2.10: Circular-to-circular waveguide from R of 14 mm to 9.9 mm

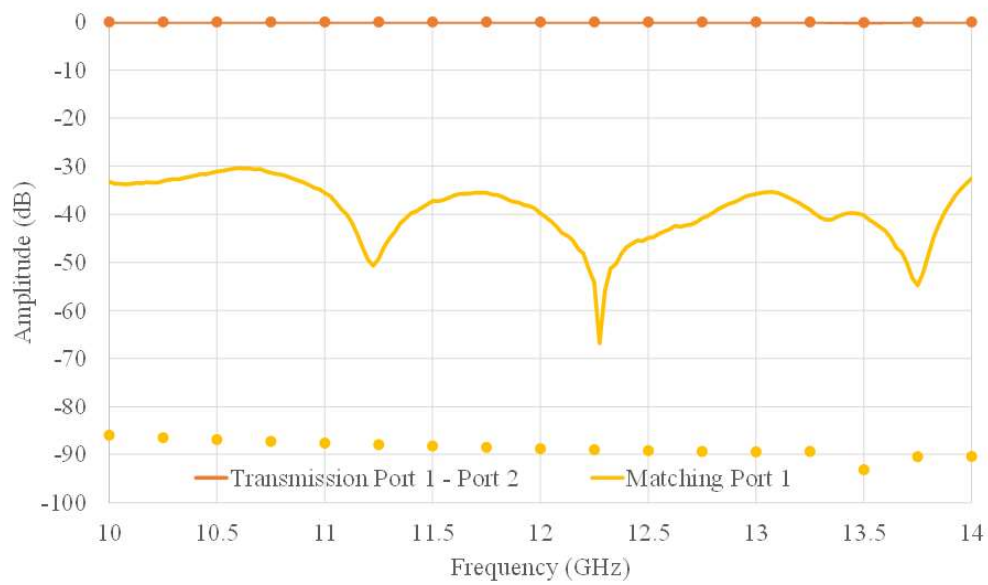


Figure 2.11: Simulations (dots) and measurements (solid line) of the Circular-to-Circular waveguide.

2.2.2 3dB/90° Hybrid Coupler

The hybrid coupler is used to combine the extracted TE_{21} modes from the mode coupler giving as output the tracking signals that are used by a processor to move the antenna toward the target as described in Section 1.2. Also in this case, mechanical connection is made through a standard WR75 flange as shown in Fig. 2.12. Measurements are performed by closing the unused ports with standard WR75 matched loads.

Graphs of Fig. 2.13 show a very good agreement between simulations and measurements in the band of interest (see Fig. 2.5). In particular, transmission and coupling around -3 dB as expected from the theory of this component. Also in this case, port isolations and matching present a good behaviour of about -30 dB.

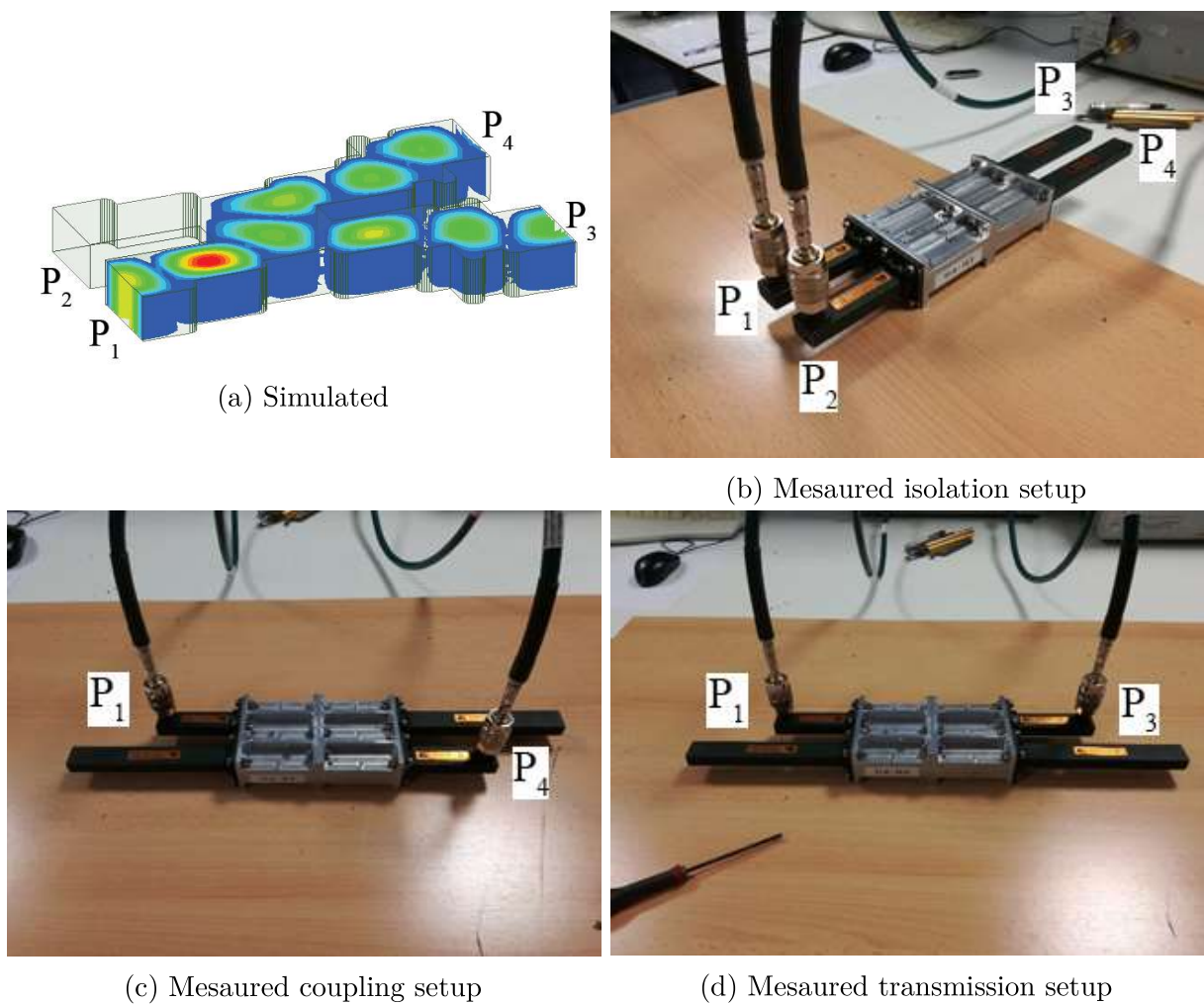


Figure 2.12: 3 dB - 90° hybrid coupler

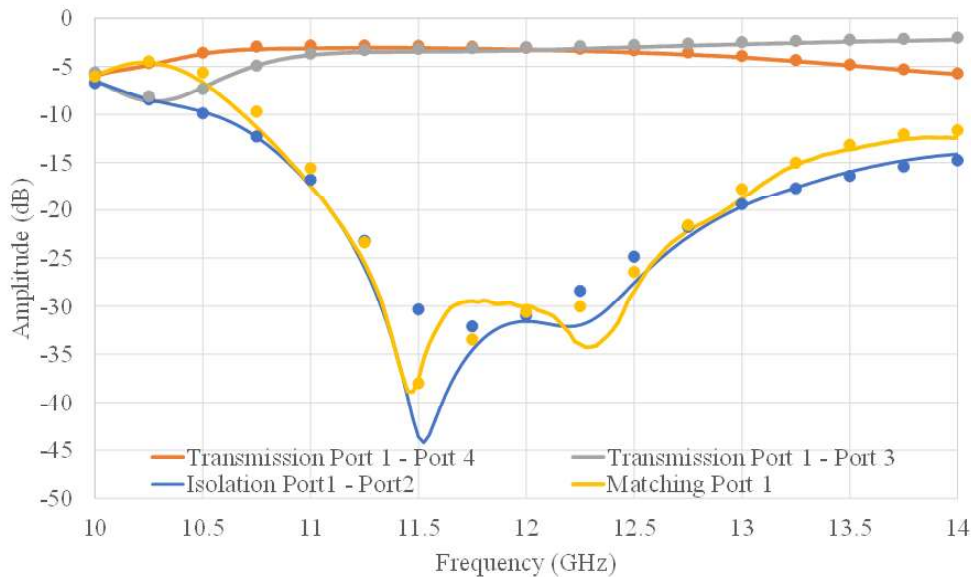


Figure 2.13: Simulations (dots) and measurements (solid line) of the 3 dB - 90° hybrid coupler.

2.2.3 Compact Quadrature Hybrid Coupler

Size and weight of waveguide component can be a limiting point for ground stations or compact tracking systems so that it might be necessary to reduce size of each component maintaining its EM characteristics. The most common way to minimize waveguide component's dimensions is through a scaling factor of the original sizes depending on the ratio between the guided modal wavelength λ_g with respect to the free space wavelength λ_0 . Hybrid couplers are one of the key components required to have a working tracking system. The proposed structure allows a very compact design without using any scaling factor, but modifying the component design, allowing an operational bandwidth of 40% with 25 dB of matching and isolation.

In the literature there exist similar structures that rarely achieve a full-band coverage with very compact sizes and a good isolation between ports.

For example, the riblet coupler [9] and its evolution [10] achieves a 25% of bandwidth exhibiting the compact characteristics through the H-plane configurations. Other structures based on multi-hole [11], [12] or multi-window (branch-line) [13], [14] coupling allow excellent EM performances but at the cost of large size of coupling sections and therefore too bulky in case the space where to install it is not sufficient. Improvements have been obtained in [15], [16] and the natural evolution [17]. In [18] to achieve a 10-dB coupler with a 44% bandwidth in a very compact design have been used three apertures in two different levels. In any case, to obtain this result, a number of matching fins and posts are required, increasing the design complexity. Plus, these elements are not necessary in a 10-dB coupler like in [19] with a 45% of bandwidth. In particular, this last design presents mechanical limitations between coupling apertures, limiting the fabrication and frequency scaling; nonetheless it requires several transitions to the standard waveguide connection, affecting the compactness. Another work in [20] uses three apertures along the longitudinal axis allowing a 41% bandwidth but increasing the total length, affecting again the compactness. Finally, a last configuration [21] is based in two back-to-back septa originating a single multi-step coupling aperture, exhibiting a very

good compactness and EM characteristics, but with a cost of a 20% operational bandwidth. To overcome all the described problems, this compact quadrature hybrid coupler proposes two symmetric stepped apertures that generates a square coaxial-like section (see Fig. 2.14), allowing an ultra-compact design and large operational bandwidth without using any junction to connect it to the standard waveguide dimensions. This design allows also to change the required EM performances to better match the needed configuration. Moreover the coaxial-like section is thick enough (larger than $\lambda_0/10$) to be easily mechanized for higher frequencies (up to 100 GHz with standard milling machines).

2.2.3.1 Field Configuration and Design

The proposed hybrid coupler is schematically represented in Fig. 2.14(a). It is a structure with three planes of symmetry and consists of a central four-stepped ridge from which two large and symmetric coupling windows are obtained. From this result a very stable phase imbalance over broad bandwidths and a coupling less sensitive to frequency variations, enabling full-band operations. Due to ridge section, no external mode transformer are needed. The coupling area presents a quasi-squared central section shown in Fig. 2.14(b) with external dimensions a_2 and b_2 , becoming a half-wave coaxial-like section, with a rectangular inner conductor of dimensions h_5 and w . As a consequence, the fundamental TE_{10} mode at the four ports of the coupler will be transformed to a quasi-TEM mode.

The quasi-coaxial central section will not allow the propagation of only the fundamental TEM mode, but also few high order modes (TE_{10} -like, TE_{01} -like and the TE_{11} -like modes) as show in Fig. 2.15, resulting in a radial field directed from the metallic central section towards the outer metallic walls (like a TEM mode) plus the fields in the same (TE_{10} mode) and opposite direction (TE_{01} and TE_{11} mode). Since the contribution of the high order modes is not negligible, the complete field in the mid-section will be a superimposition of the propagating modes, resulting in a quasi-TEM behavior, assuming a monomodal TE_{10} feeding at the input port. As the electric field propagates from one input port to the output port, complete sequence is shown in Fig. 2.16. Due to the symmetry of the structure, the same reasoning can be followed for all the other ports.

To match the waveguide height in the coupling area to standard rectangular waveguide, only a single step is required, reducing the total length of the complete structure.

The complete dimensions are shown in Table ???. Other fractional bandwidth can be easily obtained re-adapting size of the coupling area.

An important figure of merit to represent the genuineness of a circuit is through the amplitude imbalance between adjacent ports that can be seen as a sort of axial ratio (AR).

Typically, axial ratio is defined for circular or elliptical polarization as the ratio between the two vector components of the electric field. In the case of a four-port network such as an hybrid coupler, it is possible to define AR as the ratio between the two transmission parameters. Using the port distribution in Fig. 2.14(a), assuming the input port P_1 and output ports P_3 and P_4 , AR can be computed as

$$AR = \frac{|S_{31}|^2 + |S_{41}|^2 + |S_{31} + S_{41}|^2}{|S_{31}|^2 + |S_{41}|^2 - |S_{31} + S_{41}|^2} \quad (2.11)$$

Results in Fig. 2.19 where a good accordance between simulations and measurement are shown. In particular, it is possible to notice that at 12 GHz, the amplitude ratio between ports P_3 and P_4 is less than 1 dB, enhancing the goodness of this configuration.

caption[Mechanical parameters (units in mm). L_{tot} is the total length of the coupling area divided by λ_0 . Ports have standard WR75 dimensions: $a = 19.05$ mm, $b = 9.525$ mm.]Mechanical parameters (units in mm). L_{tot} is the total length of the coupling area divided by λ_0 . Ports have standard WR75 dimensions: $a = 19.05$ mm, $b = 9.525$ mm.

a_1	a_2	b_1	b_2	w	l_1	l_2	l_3
17.6	15.8	8	13.4	2.4	2.17	2.3	1.2
l_4	l_5	h_2	h_3	h_4	h_5	L_{tot}	
1.2	7.055	14.7	13	5	3	1.16	

The realized component have a very compact dimension as shown in Fig. 2.17 with a total dimension of $40 \times 40 \times 30 \text{mm}^3$ and output ports WR75. Fig. 2.18 reports an excellent agreement between simulations and measurements with an input matching and isolation below -25 dB in the frequency band under test (10-15 GHz).

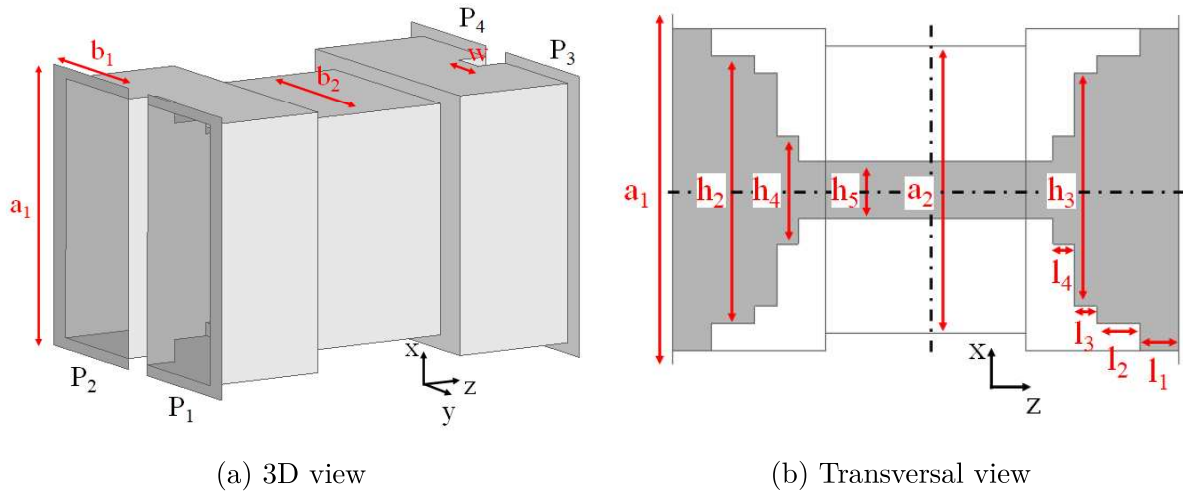


Figure 2.14: Quadrature Hybrid Coupler

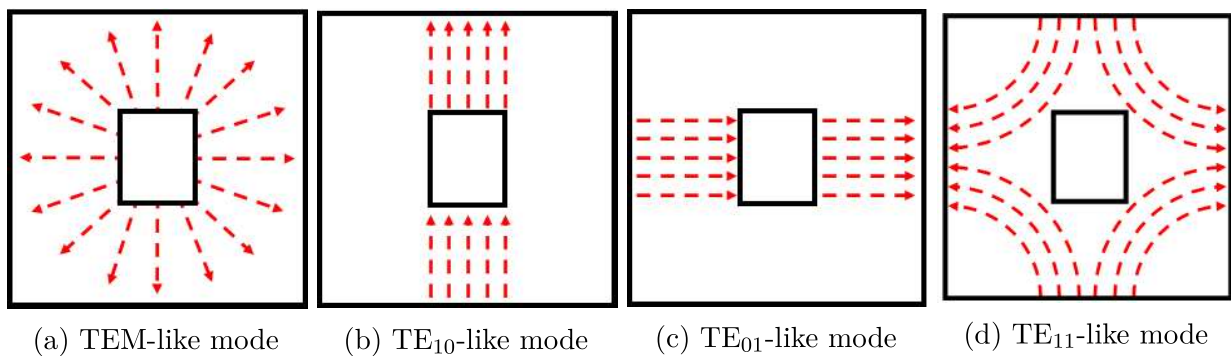


Figure 2.15: Propagating modes in the coaxial section

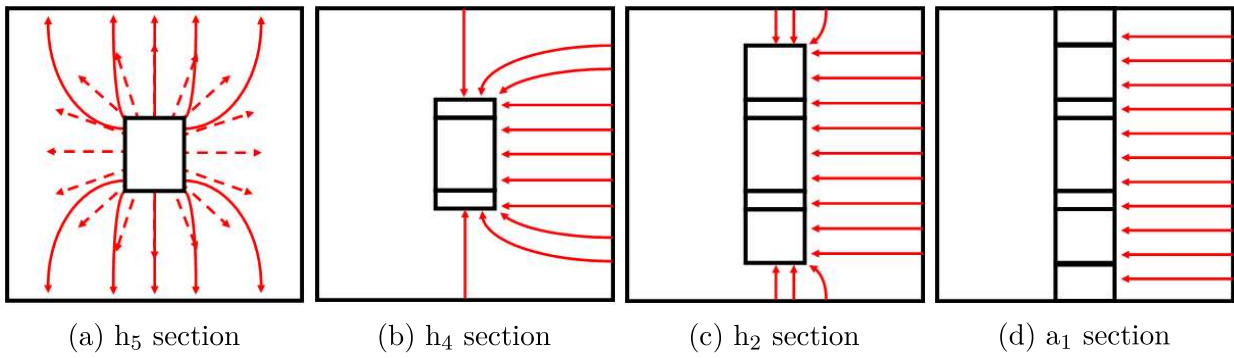
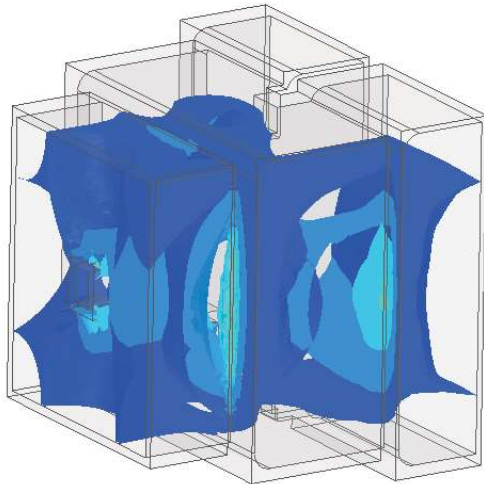
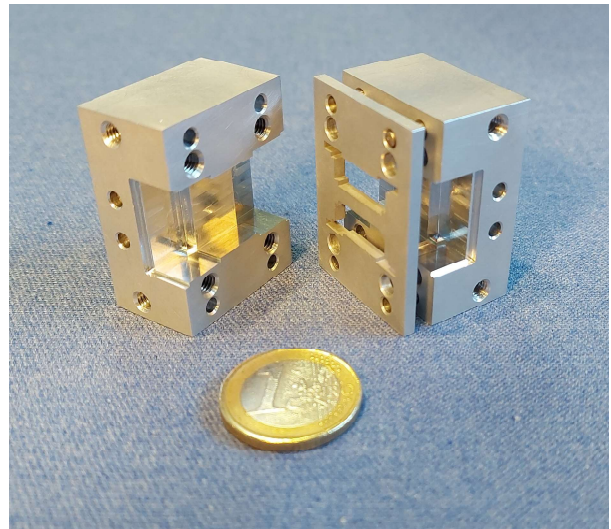


Figure 2.16: Propagating modes in the coaxial section



(a) Simulated



(b) Manufactured compared with 1€.

Figure 2.17: Designed compact hybrid coupler

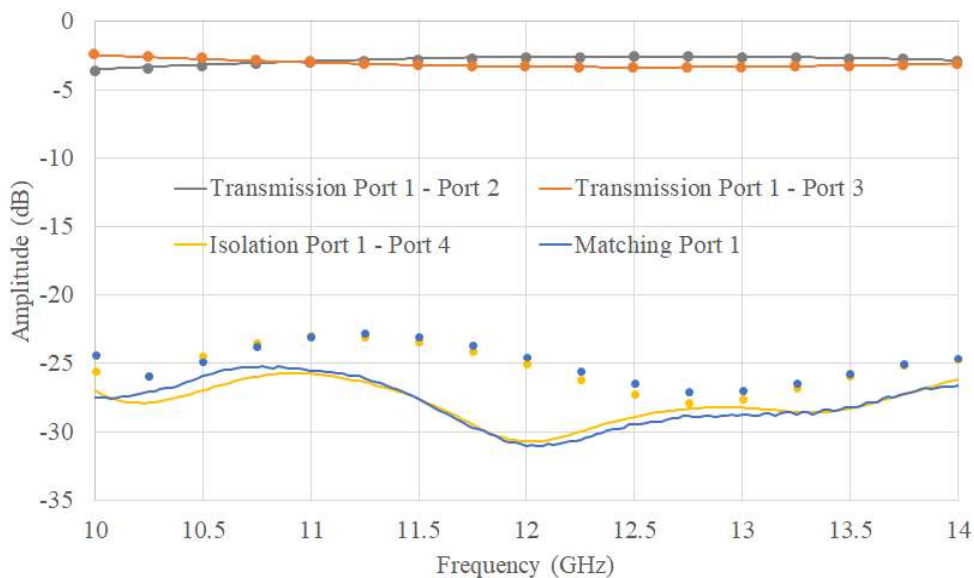


Figure 2.18: Simulations (dots) and measurements (solid line) of the compact hybrid.

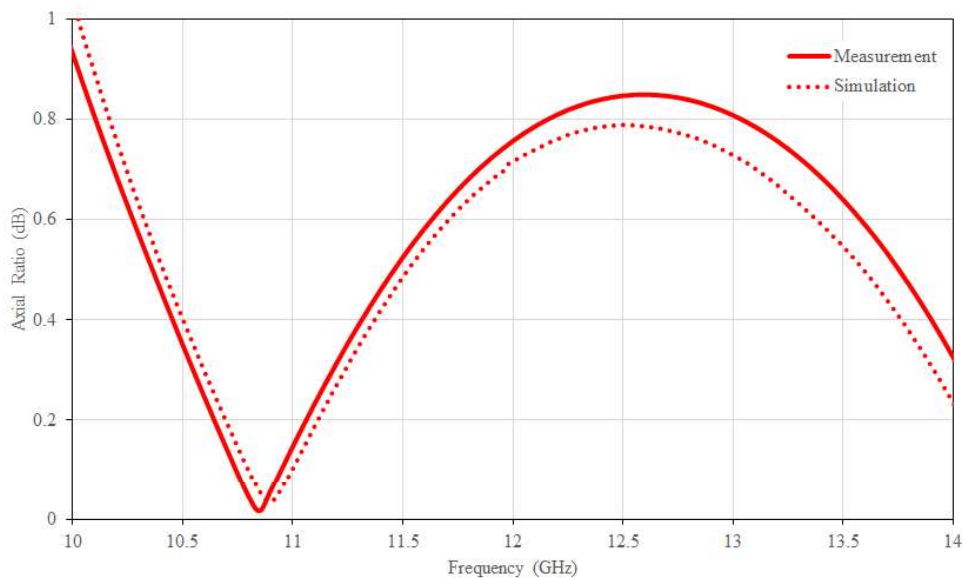


Figure 2.19: Simulations (dots) and measurements (solid line) of the axial ratio from 2.11

2.2.4 Septum Polarizer

In a classical monopulse tracking chain, a septum polariser is used to separate right-hand and left-hand circular polarization or linear polarization for the SUM signal as explained in Section 1.2. In this experiment, the septum polarizer has been used to excite the entire tracking chain having in input a commercial field source, maintaining the described theoretical characteristic. The key point is to generate the same tracking signal to build the DELTA-SUM signal it is not necessary at this stage.

For simplicity, measurements have been performed with both vertical and horizontal linear polarization as shown in Fig. 2.20.

Results in Fig. 2.21 show a very good agreement of both transmission and isolation between simulations and measurements. In particular, it is possible to notice a transmission of -3 dB for both linear polarisations inside the band of interest as expected from the theory; as the frequency increases the component cannot guarantee a good operation as it has been designed to work correctly up to 12.5 GHz (as reported in Fig. 2.5). Also in this case, mechanical connection has been made using a standard WR75 flange and to perform all the measurements, ports are closed with designed matched loads.

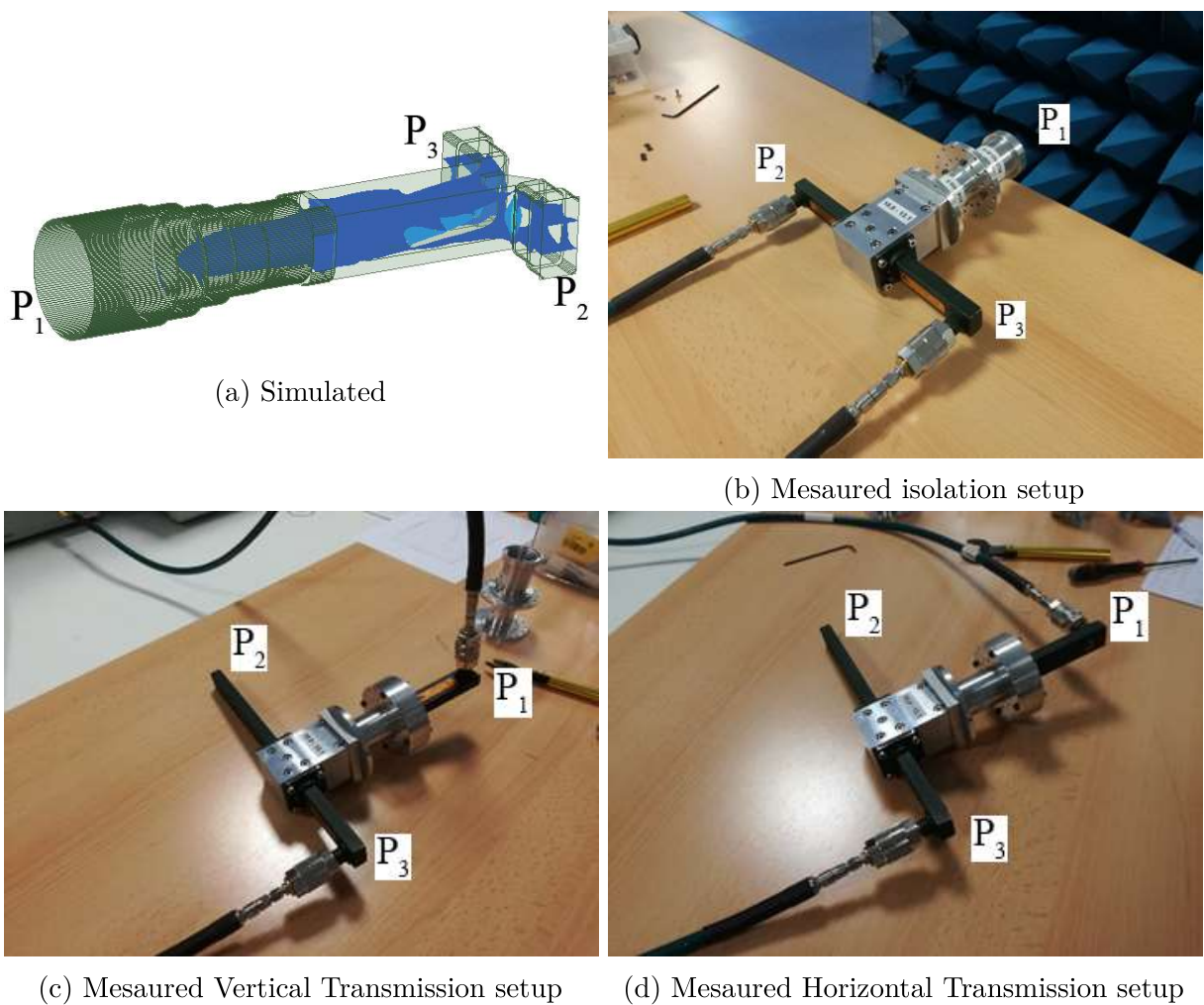


Figure 2.20: Septum Polariser

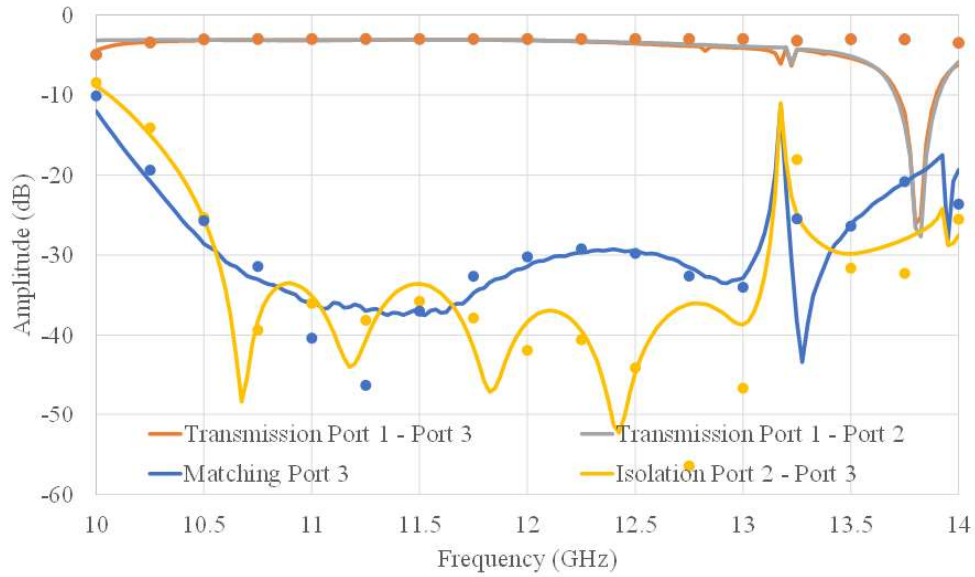


Figure 2.21: Scattering parameters of the Septum Polariser.

2.2.5 Radiating Load

An important component for the practical analysis is the radiating load shown in Fig. 2.22. This load is installed at the output port P_2 of the mode coupler (see Fig. 2.24, but also for the analysis of the septum polariser in Fig. 2.20). This component, with a radius of 14 mm as mode coupler and septum polarizer, is needed to close the circuit and avoid any back reflections of fundamental TE_{11} modes. Measurements in Fig. 2.23 shown a matching of around -30 to -35 dB in accordance with the expected behaviour. Discrepancies with simulations, like in the case of the circular-to-circular transition, are due to manufacturing process and material characteristics.

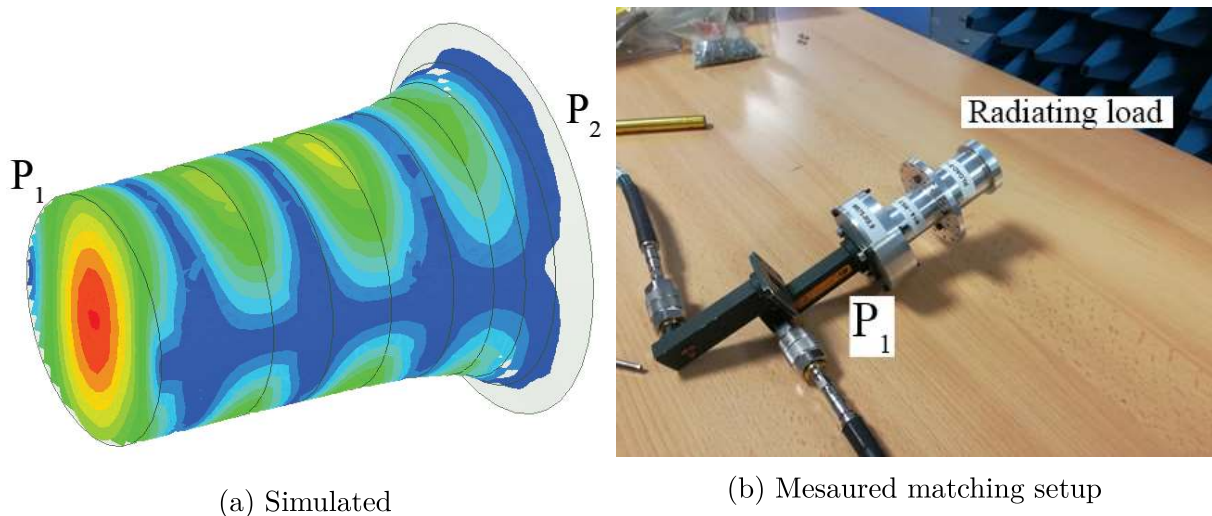


Figure 2.22: Radiating Load

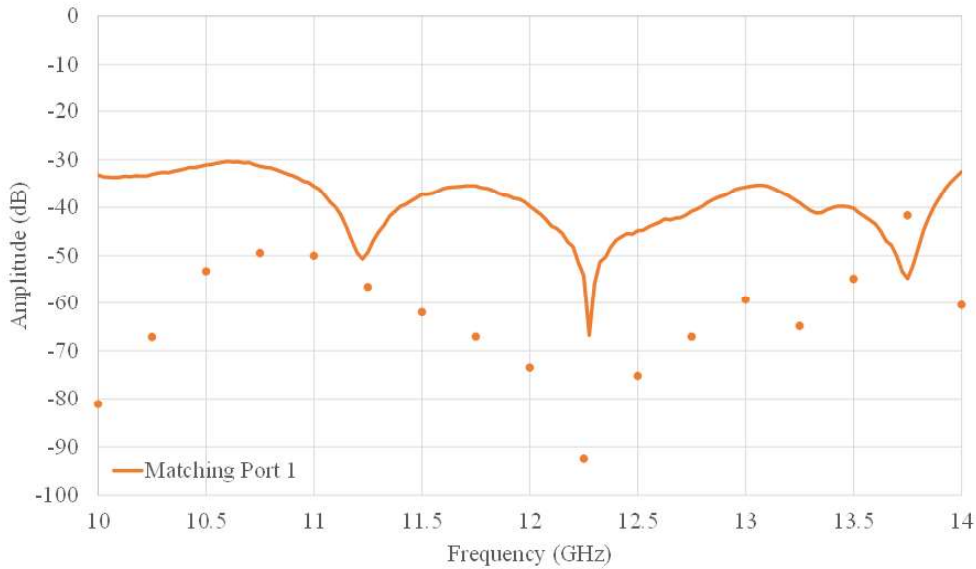


Figure 2.23: Simulations (dots) and measurements (solid line) of the radiating load.

2.2.6 Mode Coupler

The core element of a monopulse chain is the mode coupler, to extract the fundamental and high order modes and build SUM and DELTA signal. Any design or mechanical error in this component could generate catastrophic problems on the monopulse system.

The mode coupler shown in Fig. 2.24 is designed with a radius of 14 mm for the circular waveguide but to be fed and tested, transitions from larger to smaller circular waveguides are needed. This mode coupler is the simple one where only one of the two degenerate TE_{21} modes is extracted. Mechanical connections are made using standard WR75 flanges. Also in this case, unused ports in the measurement process have been closed with standard WR75 matched loads and with the designed circular matched load.

Fig. 2.25 shows the electromagnetic behaviour of the component in the band of interest (Fig. 2.5) connected to the hybrid coupler. Very good agreement can be seen for matching S_{33} at the output port P_3 closing P_1 and P_2 with matched loads. Also a very good agreement between simulations and measurements for the transmission of the fundamental modes TE_{11} from port P_1 to port P_2 as well as the coupling from port P_1 to port P_3 .

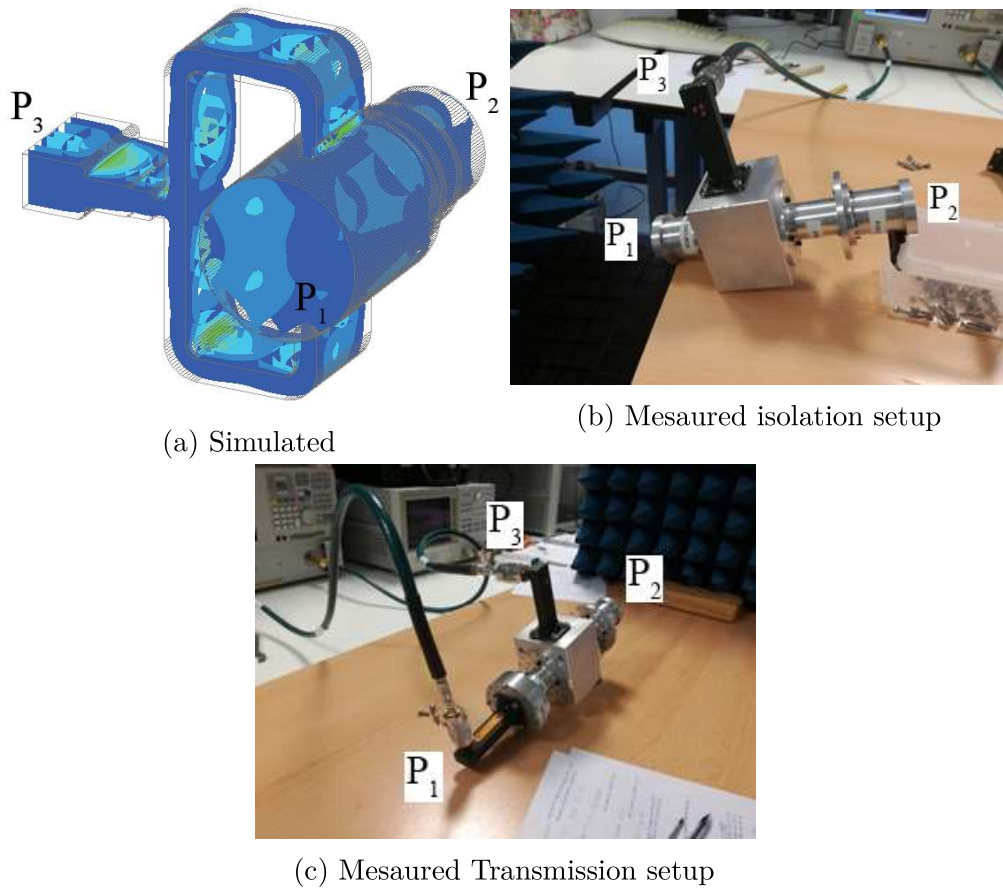


Figure 2.24: Mode Coupler - Single Mode Extraction

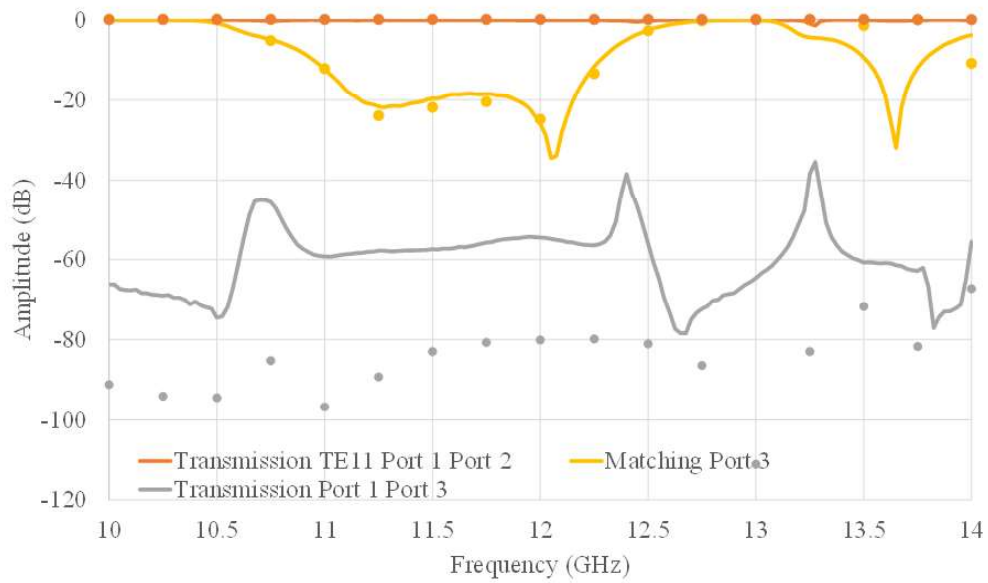


Figure 2.25: Scattering parameters of the single-mode Mode Coupler.

2.3 OCWG Measurements and Tracking test

Once all the microwave components are built, the test for a complete tracking chain is possible.

A prototype of the step-waveguide junction has been fabricated considering a circular waveguide with a radius $R = 14$ mm (Fig. 2.27). The structure, made of raw aluminium, is composed by two sections of waveguide designed so that they can be joined with different waveguide offsets, namely from $M_o = 0.2$ mm up to $M_o = 1.4$ mm with a step of 0.2 mm, while the rotation angle ϕ (Fig. 2.3) can sweep from 0° to 360° with a step of 22.5° . The monopulse tracking chain (see Fig. 1.11) has been assembled through the designed components described before, in addition to the step-waveguide junction for the excitation of HOMs. In this case, a dual-mode mode coupler is used (Fig. 2.26), where the main circular waveguide P_1 has a radius of $R = 14$ mm and is connected to the step waveguide junction, which is fed with a circular polarised input signal obtained by properly combining the two degenerate fundamental TE_{11} modes through a septum polariser. A RHCP is therefore generated and will be used for the entire measurements campaign.

The mode coupler is able to extract both the TE_{21}^S and the TE_{21}^C modes at the output ports P_3 and P_4 . Moreover, the 3-dB hybrid junction is connected to the ports P_3 and P_4 of the step-waveguide junction to extract the left-hand circular polarisation (LHCP) and right-hand circular polarisation (RHCP).

The overall experimental setup (shown in Fig. 2.28) is then closed through the radiating load connected to the port P_2 of the mode coupler where the fundamental TE_{11} is extracted for the SUM signal. In this situation it is not needed.

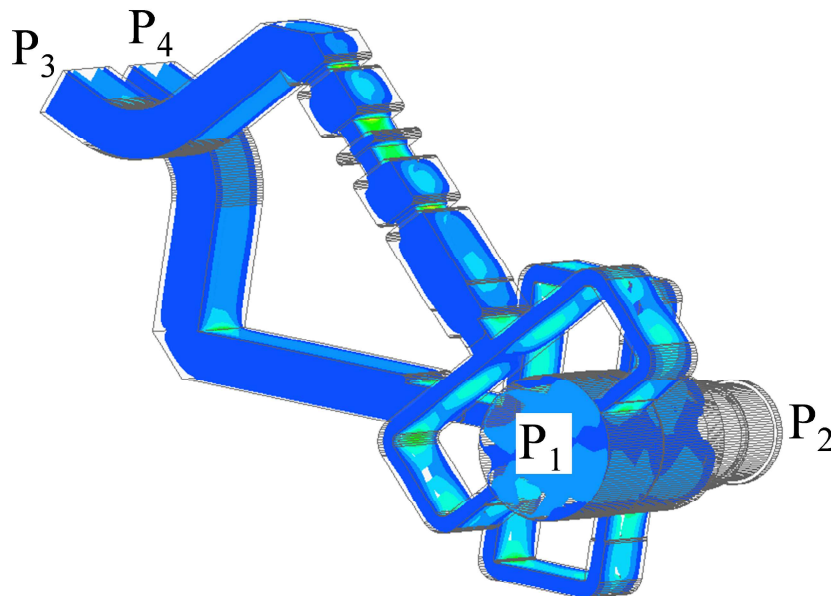
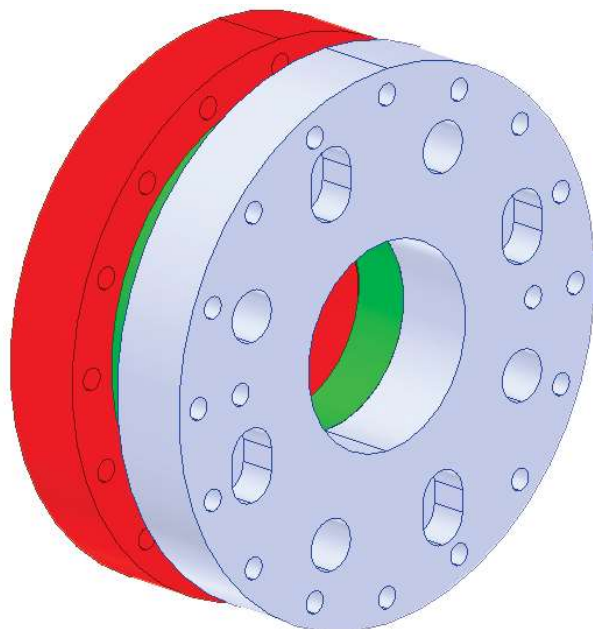


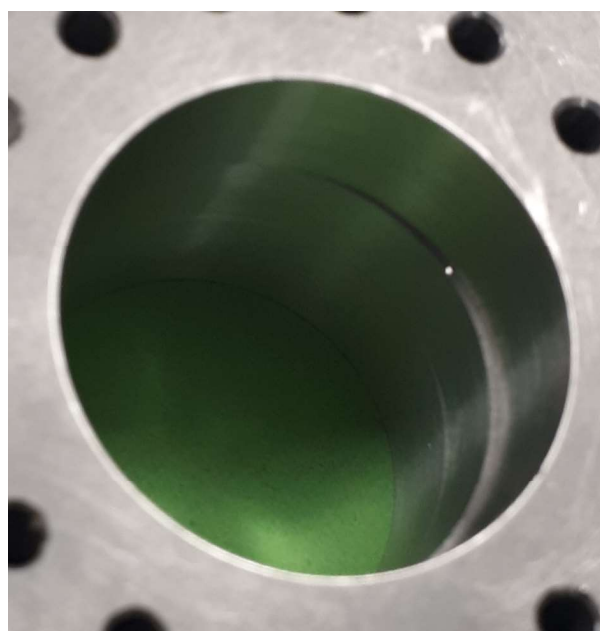
Figure 2.26: Mode coupler for $TE_{21}^{S/C}$ mode extraction used in the monopulse system.



(a) CAD structure



(b) Manufactured



(c) Close-up step-junction

Figure 2.27: Step-waveguide junction

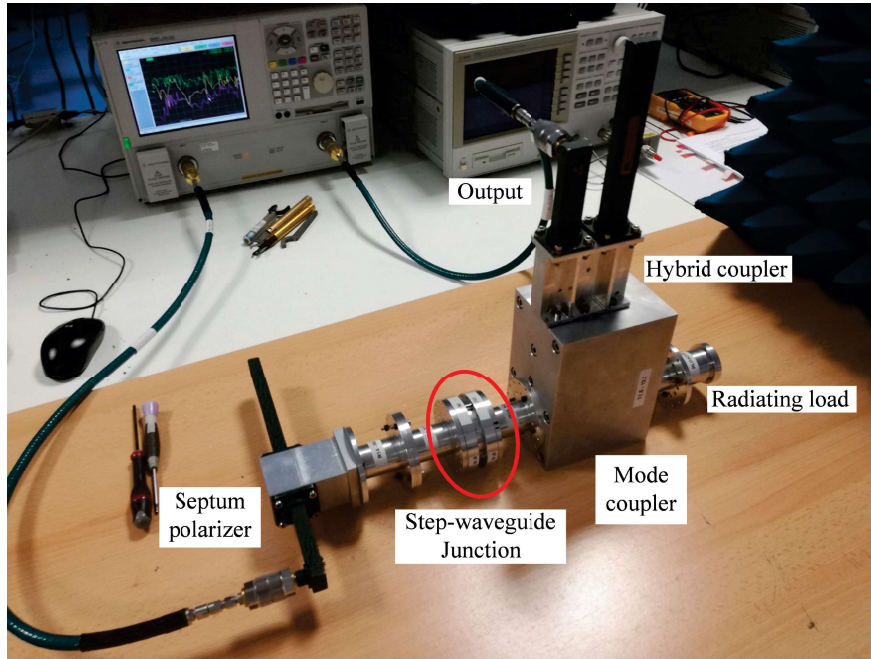


Figure 2.28: Experimental prototype of the complete setup where, apart from the various transitions and matched loads, it is possible to see the offset waveguide in the middle of the structure, the tracking coupler connected to a septum polarizer on the side, and a 3 dB/90° hybrid coupler on the top. The hybrid has one output closed with a matched load to measure the RHCP signal.

The experimental results at 12 GHz are shown in Fig. 2.29a for the RHCP and in Fig. 2.29b for the LHCP. The measured levels for the RHCP are around -33 dB, -27 dB, and -23 dB for $M_o = 0.4$ mm, $M_o = 0.8$ mm, and $M_o = 1.2$ mm, respectively in accordance with the simulations described in Chapter 2.1.3. As expected, the values for the LHCP shown in Fig. 2.29b are practically zero, due to the RHCP excitation of the system. In the same Fig. 2.29a, the simulated results are also reported (crosses). The comparison shows a good agreement, thus demonstrating the effectiveness and accuracy of the proposed step-waveguide junction to mimic the mode excitation due to a depointed target.

A wideband measurement of the system has also been performed. Fig. 2.30 shows the amplitude of the coupling coefficient level TE_{21} computed through Eq. 2.7 and measured in the frequency band 11.5 – 12.2 GHz, for different offsets M_o . The agreement of the measurements is very good with a maximum discrepancy of ± 1 dB, probably due to a non-perfect matching between the cascaded tracking coupler, septum polariser, and matched load used to close the circuit. In any case, the average of the measured coupling is in agreement with the theoretical values.

Finally, Fig. 2.31 shows the frequency behavior of the measured phase $\Psi_{TE_{21}}$ of the mode TE_{21} for a fixed offset $M_o = 0.8$ mm. Also, in this case the agreement between simulations and experimental results is very good with a small up-shift of a few degrees, which is attributed to a mismatch of the radiating load in Fig. 2.28, leading to a non-negligible contribution of the reflected waves. Similar curves were measured for the other values of the offset, but they are not reported since the plots are practically identical to the one in Fig. 2.31.

It is worth noting that the current implementation is a proof of concept, and it has the practical limit to require a manual intervention to change the offset and/or the rotation angle

between the two waveguides. Moreover, the steps are fixed both in offset and in rotation angle. However, this operation can be easily motorized to achieve a continuous rotation and offset, thus speeding-up the measurement as well as allowing to mimic any direction of arrival of the signal.

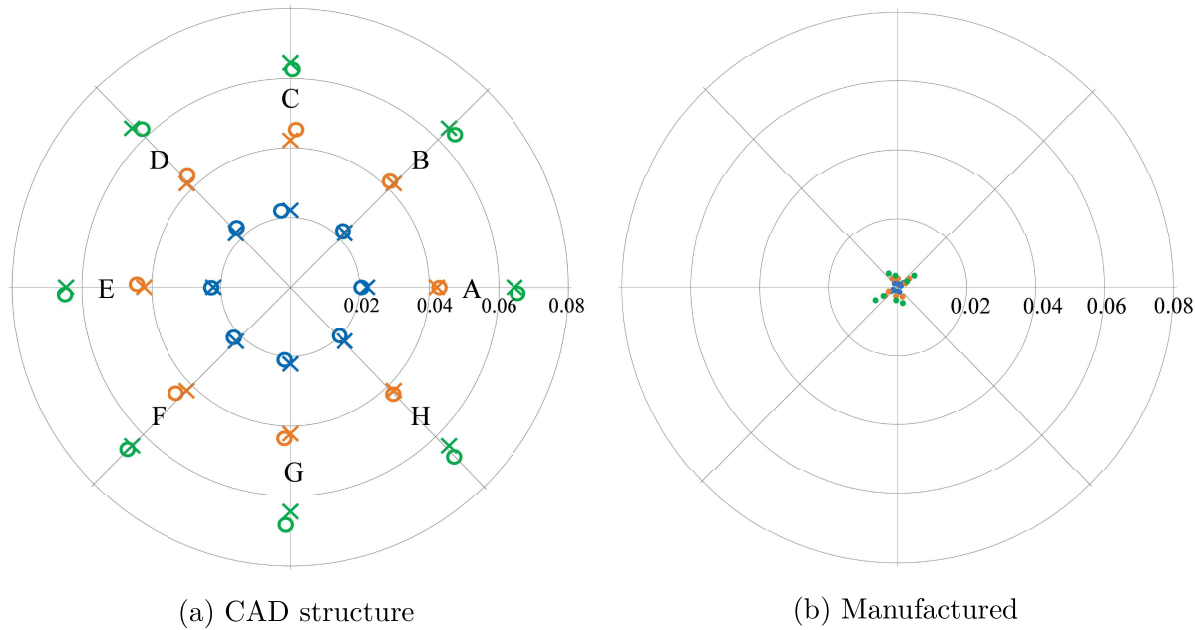


Figure 2.29: Experimental results for an incident RHCP signal.(a) output RHCP; (b) output LHCP. In both cases three offset values are considered, namely $M_o = 0.4$ mm (blue dots), $M_o = 0.8$ mm (orange dots), and $M_o = 1.2$ mm (green dots). In the case of the RHCP output also the simulated results of the two antenna systems are presented (crosses).

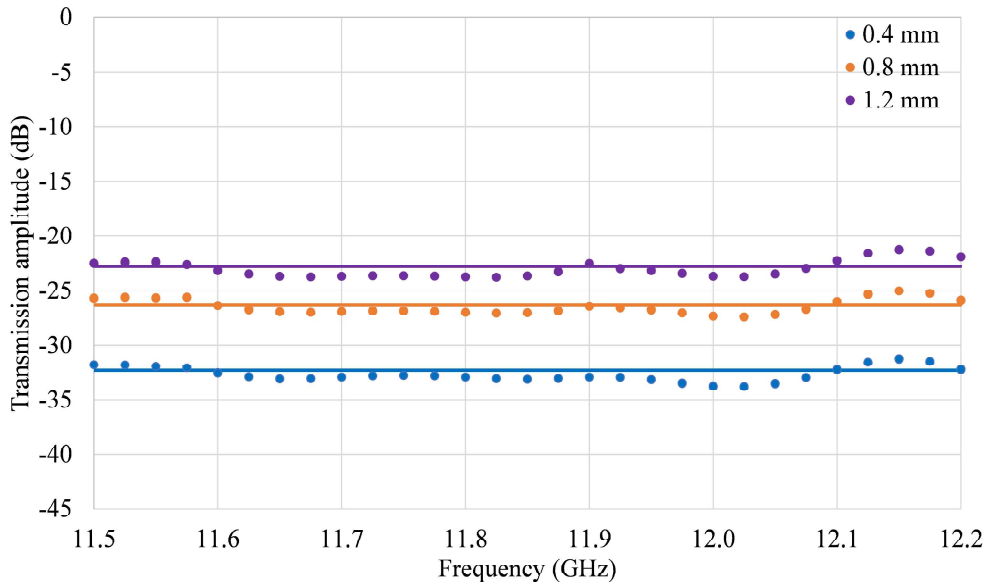


Figure 2.30: Wideband values of the amplitude of the excitation coefficients at the RHCP output port for different values of M_o . The measured values (markers) are compared to the simulations (solid lines).

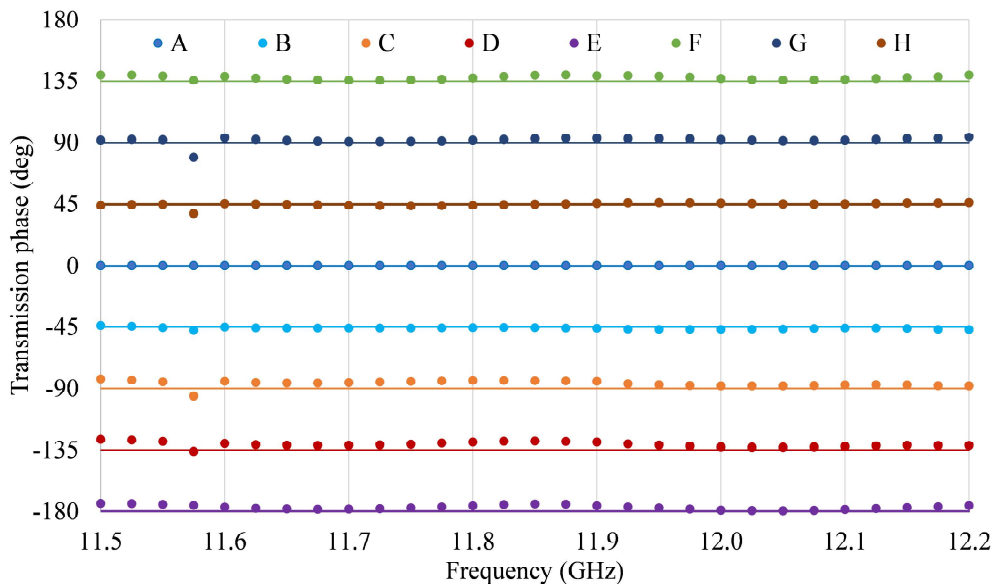


Figure 2.31: Wideband values of the phases of the excitation coefficients at the RHCP output port for different values of rotating angle ϕ , for an offset $M_o = 0.8$ mm. The measured values (markers) are compared to the simulations (solid lines). Positions A, B, C, ... refer to Fig. 2.3b.

2.4 Conclusion

In this second chapter, a way to calibrate in-lab monopulse systems has been shown through description design and analysis of a complete monopulse chain fed by an overmoded circular waveguide in Ku-Band, working in the frequency band 10 – 14 GHz. It has been proven how it is possible to calibrate monopulse systems exciting in the needed high order modes of a circular waveguide without the need of a physical calibration tower. This system can be easily rescaled to work at other frequency bands or other high order modes through the proposed mathematical model.

The advantage of the proposed work is the possibility to test in-lab monopulse system mimicking the depointing effect avoiding any problem related to environmental conditions, reducing costs and antenna downtime.

References

- [1] C. Balanis, *Antenna Theory: Analysis and Design*. Wiley, 2016, ISBN: 9781118642061.
- [2] J. Taylor, *Deep Space Communications*, ser. JPL Deep-Space Communications and Navigation Series. Wiley, 2016, ISBN: 9781119169062.
- [3] K. Wang, T. Li, H. Li, *et al.*, “A broadband te₀₁-te₁₁ mode converter with elliptical section for gyro-twts”, *IEEE Transactions on Microwave Theory and Techniques*, vol. 67, no. 9, pp. 3586–3594, 2019. DOI: 10.1109/TMTT.2019.2925065.
- [4] A. Chittora, S. Singh, A. Sharma, and J. Mukherjee, “A novel tm₀₁ to te₁₁ mode converter designed with radially loaded dielectric slabs”, *IEEE Transactions on Microwave Theory and Techniques*, vol. 64, no. 4, pp. 1170–1175, 2016. DOI: 10.1109/TMTT.2016.2536031.
- [5] G. Ceccato, J. L. Cano, A. Mediavilla, and L. Perregrini, “Controlled excitation of waveguide high-order modes for a simple and accurate monopulse tracking system test bench”, *IEEE Transactions on Microwave Theory and Techniques*, vol. 69, no. 2, pp. 1327–1334, 2021. DOI: 10.1109/TMTT.2020.3045202.
- [6] —, “Controlled high order mode generation for tracking coupler bench test”, in *2020 IEEE/MTT-S International Microwave Symposium (IMS)*, 2020, pp. 904–907. DOI: 10.1109/IMS30576.2020.9224025.
- [7] —, “A simple and accurate method for circularly polarised monopulse tm₀₁ tracking system testing”, in *2020 23rd International Microwave and Radar Conference (MIKON)*, 2020, pp. 218–221. DOI: 10.23919/MIKON48703.2020.9253906.
- [8] N. Marcuvitz, I. of Electrical Engineers, I. of Engineering, *et al.*, *Waveguide Handbook*, ser. IEE electromagnetic waves series. McGraw-Hill, 1951, ISBN: 9780863410581.
- [9] H. J. Riblet, “The short-slot hybrid junction”, *Proceedings of the IRE*, vol. 40, no. 2, pp. 180–184, 1952. DOI: 10.1109/JRPROC.1952.274021.
- [10] L. Hildebrand, “Results for a simple compact narrow-wall directional coupler”, *IEEE Microwave and Guided Wave Letters*, vol. 10, no. 6, pp. 231–232, 2000. DOI: 10.1109/75.852425.

- [11] S. Wen, Q. Wang, Taowu, and Y. Tan, “Design of a compact 3db ka-band directional coupler”, in *The 2012 International Workshop on Microwave and Millimeter Wave Circuits and System Technology*, 2012, pp. 1–4. DOI: 10.1109/MMWCST.2012.6238197.
- [12] M. M. M. Ali, S. I. Shams, and A.-R. Sebak, “Low loss and ultra flat rectangular waveguide harmonic coupler”, *IEEE Access*, vol. 6, pp. 38 736–38 744, 2018. DOI: 10.1109/ACCESS.2018.2854189.
- [13] S. Srikanth and A. Kerr, “Waveguide quadrature hybrids for alma receivers”, 2001.
- [14] H. Rashid, V. Desmaris, V. Belitsky, M. Ruf, T. Bednorz, and A. Henkel, “Design of wideband waveguide hybrid with ultra-low amplitude imbalance”, *IEEE Transactions on Terahertz Science and Technology*, vol. 6, no. 1, pp. 83–90, 2016. DOI: 10.1109/TTHZ.2015.2502070.
- [15] T. Kawai, M. Kishihara, Y. Kokubo, and T. Ohta, “Cavity-type directional couplers with simple structure”, in *1997 IEEE MTT-S International Microwave Symposium Digest*, vol. 2, 1997, 413–416 vol.2. DOI: 10.1109/MWSYM.1997.602821.
- [16] E. Hadge, “Compact top-wall hybrid junction”, *Transactions of the IRE Professional Group on Microwave Theory and Techniques*, vol. 1, no. 1, pp. 29–30, 1953. DOI: 10.1109/TMTT.1953.1124837.
- [17] R. Beyer and U. Rosenberg, “Compact top-wall hybrid/coupler design for extreme broad bandwidth applications”, in *IEEE MTT-S International Microwave Symposium Digest, 2005.*, 2005, pp. 1227–1230. DOI: 10.1109/MWSYM.2005.1516898.
- [18] C. L. Wang, “Compact 10 db broadband directional coupler”, in *2013 IEEE International Conference on Applied Superconductivity and Electromagnetic Devices*, 2013, pp. 282–284. DOI: 10.1109/ASEMD.2013.6780775.
- [19] H. Xin, S. Li, and Y. Wang, “A terahertz-band e-plane waveguide directional coupler with broad bandwidth”, in *2015 16th International Conference on Electronic Packaging Technology (ICEPT)*, 2015, pp. 1419–1421. DOI: 10.1109/ICEPT.2015.7236847.
- [20] Y. Zhang, Q. Wang, and H. Xin, “A compact 3 db e -plane waveguide directional coupler with full bandwidth”, *IEEE Microwave and Wireless Components Letters*, vol. 24, no. 4, pp. 227–229, 2014. DOI: 10.1109/LMWC.2013.2296297.
- [21] N. J. G. Fonseca and J.-C. Angevain, “Waveguide hybrid septum coupler”, *IEEE Transactions on Microwave Theory and Techniques*, vol. 69, no. 6, pp. 3030–3036, 2021. DOI: 10.1109/TMTT.2021.3074194.

3

Radome Effects on tracking

It is not unusual to find antennas for space, military and civil applications installed in places where environmental conditions have a significant impact on their performances. Ice, moist, rain, wind, cold and hot temperature, not only have big impact on the antenna's electromagnetic performances, but also on its mechanical characteristic. Strong wind can move the antenna losing target alignment; accumulation of water can degrade the surface with rust; temperature variations can deform the geometrical shape of the antenna and so on. All these problems must be taken into account during the design and development of the ground station since they can inexorably degrade its performances, ending up with catastrophic problems (such as Arecibo antenna in Puerto Rico [1]).

Environmental problems can be overcome through special structure used to enclose and shield ground stations from the environment. In such way, the antenna can be kept in controlled atmosphere and avoid most of the problems described before. These shields are typically used in places with severe weathers (like poles or equator), but it is not unusual to find them also in places where weather is not a major key factor, but it is necessary to protect the antenna (i.e. communication towers, ships, aircraft). Structures of this kind (i.e. radomes) have different advantages in antennas' performances and reduction of operational costs because less maintenance is required. These advantages, on the other hand, do not come for free; radome, in fact, must be specifically designed for the specific antenna in terms of size, shape and performances. Therefore these structure are very expensive.

Radomes are typically made by dielectric or other composite materials, covering the antenna in its entirety, therefore these materials must be as transparent as possible in the working frequency band.

Radomes can be used to protect any kind of antennas: from the small ones like telecom antennas for civil application (i.e. cell towers in Fig 3.1) to reflector antennas for aeronautical and space applications (i.e. ECHELON system in Fig 3.2). In this thesis radomes for large ground stations for space, civil and military applications are considered. In these cases there are two types of radomes: Multi-Layer (ML) or Metal Space Frame (MSF) [2] [3].



Figure 3.1: Example of GSM station [4]



Figure 3.2: Example of aeronautical surveillance system [5]

Multi-Layer radomes are designed with self-supporting panels (typically with an hexagonal shape) connected with each other through metallic bolts (Fig. Fig. 3.3a); panels are made by different layers with high dielectric constant (i.e. E-glass or polyester fibreglass) and layers with low dielectric constant (honeycombs or foam).

Metal Space Frame radomes, on the other side, are made with a single dielectric layer panels (typically with a triangular shape) connected trough metallic poles (see Fig. 3.3b)



(a) Multi-Layer Radome

(b) Metal Space Frame Radome

Figure 3.3: Difference between ML and MSF Radome. It is possible to notice the different frame shape and joints between the two types. (Photo credits of ESOC)

One of the big issue of radomes in these applications is the tracking capability. Putting whatever object in front of an antenna, may degrade the electromagnetic performance and even if radomes are specifically designed to be as much transparent as possible, antenna's EM performances will be still affected. In Chapter 1 has been discussed what are the problems for monopulse system and where these problems are generated inside the tracking chain. Radomes, are external structure that do not depend on the antenna's hardware, but play a role in the monopulse by modifying the EM field received (or transmitted) that is used to couple modes in the waveguide network to generate SUM and DELTA signals. Results are shifts and asymmetric changes of the DELTA with respect to the SUM signal as shown in Fig 3.4, where the presence of radome changes the DELTA signal shape, with consequent tracking errors and depointing problems.

In Chapter 3.1.1 will be shown a technique to compensate this problem. Therefore, aside from antenna's tracking chain, the presence of radome structure adds an extra contribute enhancing the depointing problem. In addition to that, the last element that can worse even more the depointing is that on radome may deposit water in all form: liquid (rain, fog, mist) and solid (ice, snow) not only increasing EM losses, but also generating a sort of lens effect that may scatter in an uncontrollable way the received or transmitted field of the antenna. This last contribution cannot be compensated or corrected but it is possible minimize it by designing particular surfaces preventing or minimizing the water effect as explained in Chapter 3.2.

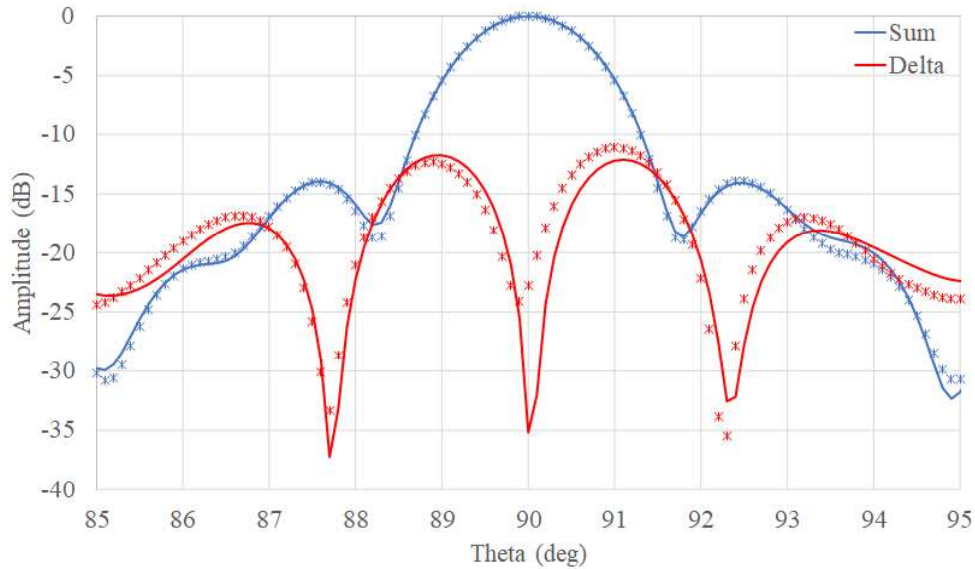


Figure 3.4: Example of Sum and Delta Offset without (solid line) and with (crosses) feed obstruction of a 1-metre diameter cassegrain antenna at 12 GHz

3.1 Multi-Layer Radome

In this thesis, Multi-Layer (ML) radomes' panels are studied because are considered the most common ones due to the balance between electromagnetic and mechanical characteristics with limited operational maintenance.

These panels are designed as stack of different dielectric materials with high and low dielectric constant to balance the electromagnetic transparency as well as strong mechanical resistance. Usually the external face of the panels is protected with an additional layer to guarantee the water resistance and prevent accumulation of moist, snow or ice.

Radome with ML panels are self supporting without the need of atmospheric pressure control from the inside. Interconnection is possible overlapping two panels jointed together with bolts and screw.

Panels are frequency dependent, therefore they must be designed to work in a specific frequency band: for low frequencies, in most of the panels it is possible to guarantee the electromagnetic transparency along with a robust structure; on the other side, for high frequencies, panels may result too thin to guarantee a sufficient mechanical robustness. Every company that design ML radomes have its own recipe to build this structures, but all have in common that dielectric materials are always used and the only difference is the internal structure (number of layers, thickness, etc.).

ML radomes used in these studies are produced by FDS Italy Srl. Seven different type of panels are tested (an example shown in Figure 3.5). For reason of intellectual properties, data designs cannot be shown. Non-commercial examples and data are only presented.

Fig. 3.5(a) shows how ML panels are designed and Table 3.1 shows the dielectric properties of each material used for radomes' panels. Foam constitute the core material of each panel, guaranteeing mechanical stiffness as well as the correct EM properties. To make the even more robust, different layers of fiberglass are used in a sort of sandwich configuration, while the external layer is made with a coating layer to avoid water penetration. Panels are jointed

through metallic bolts to guarantee a solid structure, but also a solution with plastic bolts will be presented (Fig. 3.5(b)-(c)). The presence of metallic elements in the interconnection can cause electromagnetic losses due to scattering.

The aim of this study is to overcome the electromagnetic losses due to metallic interconnection by adding compensating elements making these panels as much transparent as possible with minimum losses. This analysis has been performed through the EM simulator Ansys HFSS and measurements in FDS Italy facilities.

Table 3.1: Dielectric parameters of common material used for Multi-Layer radomes' panels

Material	ϵ_r	$\tan\delta$
Foam	1.1	0.002
Fyberglass	4.1	0.013
Gelcoat	3.0	0.005

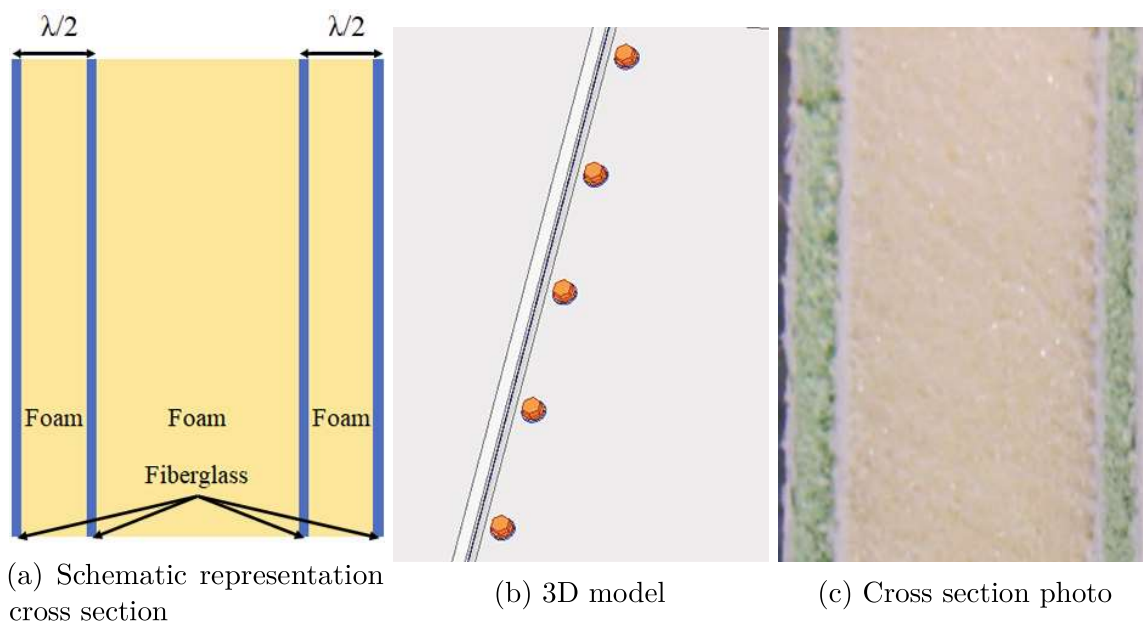


Figure 3.5: Example of Multi-Layer Radome

3.1.1 IFR Model and Joint Compensation

In an ideal condition, radome for aeronautical and space applications where reflector antennas are involved, could be described as a structure made by a single dielectric panels with transparent electromagnetic properties; therefore EM analysis can be performed though scattering parameters or using the generic ABCD matrix, studying reflection and transmission of the EM signal from the internal antenna to the external one.

In real situations analysis through ABCD matrix cannot be performed since radome is composed by multiple panels connected to each other; instead, a differential analysis between the transmitting and receiving antennas, firstly using a panel without metallic interconnection (a big single panel) and then using two jointed panels interconnected (Fig. 3.7) allow to understand its EM behaviour.

To analyse this problem the Induced Field Ratio (IFR) [6]-[7] is used, by considering the ratio between the plane wave generated from the transmitting antenna that hits the panel without the joints and reaches the receiving antenna, and the plane wave that hits the panel with joints.

$$IFR = \left(e^{-\Delta\alpha} e^{-\Delta\phi} - 1 \right) \sqrt{\frac{\lambda D_1 D_2}{D_1 + D_2}} \frac{e^{-j\frac{\pi}{4}}}{w} \quad (3.1)$$

where $\Delta\alpha$ and $\Delta\phi$ are the amplitude and phase variation of the incident field on the joint, λ the wavelength, D_1 and D_2 the distances between the joint and the two probe antennas (that for simplicity is assumed to be equal) and w the interconnection width.

With this definition, for a purely non-blocking object, hence mostly transparent, the resulting IFR will be $0 + j0$ while a pure blocking object (such as a metallic wall) it would result in an IFR of $-1 + j0$ that will appear as completely opaque and much larger than the considered wavelength.

Therefore, the aim of this study is to minimize the IFR in order to obtain a structure as less blocker as possible.

To compensate the presence of metallic joints and mitigate the scattering that can cause, a metallic structure has been installed inside the jointed section between the two panels and locked with panels' rivets. This ladder-shaped metallic structure (Fig. 3.6) exploits electromagnetic resonances to make these joints as much invisible to EM fields as possible. Each ladder is designed to work in the specific panel's frequency band by adapting its size. Two types of ladders have been designed: a simple ladder with single open window (Fig. 3.6a), and a triple ladder, with three open windows (Fig. 3.6b).

- The simple ladder presents three degrees of freedom: window size (height H_s and width W_s) and width of the metallic structure (w). This ladder compensates the IFR more effectively at low frequency;
- a triple ladder with two symmetric smaller windows in addition to the bigger one, presenting an additional degree of freedom, the internal window's width (W_s) and it is more suggested for higher working frequencies.

In both ladders, for simplicity, width of the metallic structure is considered always the same and after some tests, thickness of the structure does not play a big role (up to 1 mm thickness).

EM analysis and measurement setup consist in two broadband horn antennas placed at a distance from the panel support so that the far field condition is guaranteed (Fig. 3.7 and Fig. 3.9). The alignment between horns and panels in the measurement setup has been made through a laser pointer aligning the interconnection axis of the jointed panels with the antenna boresight (Fig. 3.8 and Fig. 3.10) and a differential analysis has been performed. First without any metallic compensation (without ladders) and then installing the compensating structure. All the measurements have been performed in the FDS Italy's anechoic chamber. Tests have been conducted in vertical and horizontal polarization by rotating the two horns of 90° . Panel support has been designed with a transparent material in the microwave region, similar to the material used for radome panels. Panels are then fixed to the support using nylon screws to avoid possible vibrations.

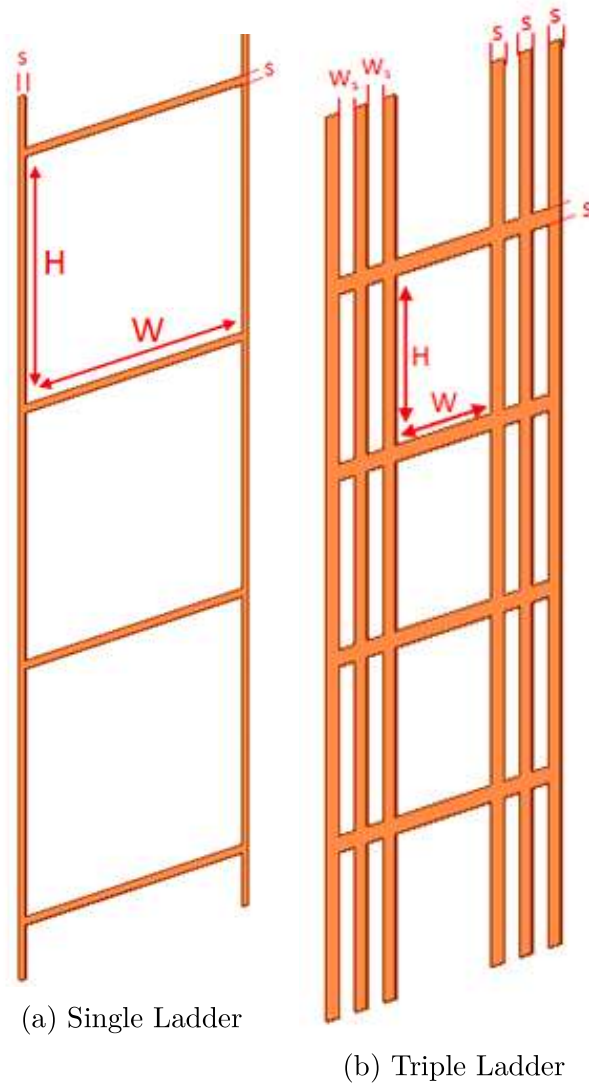


Figure 3.6: IFR compensating metallic structures

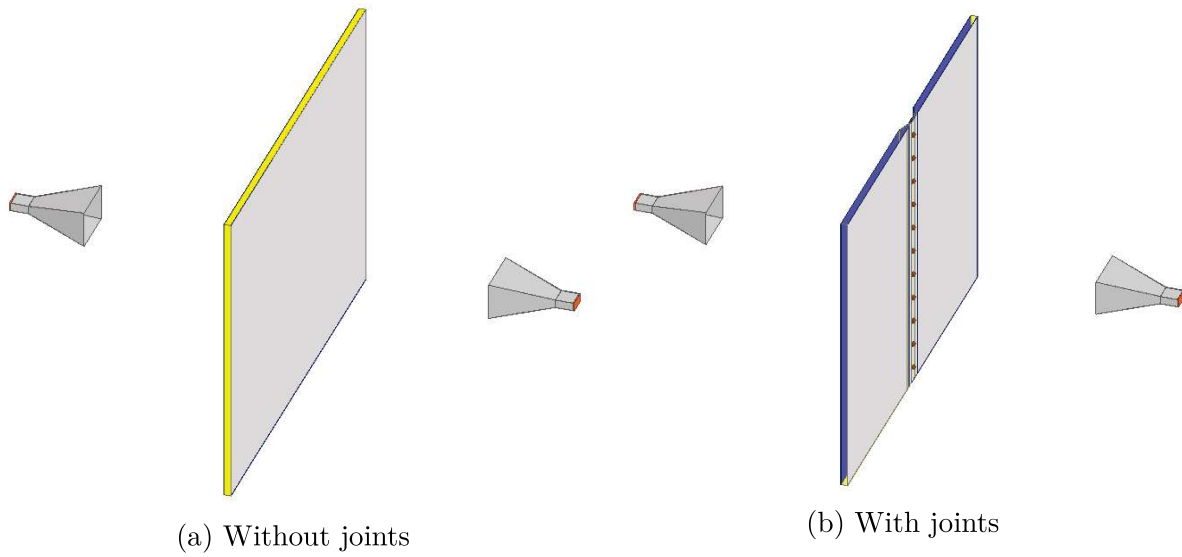


Figure 3.7: Example of HFSS simulation setup of a multi-layer radome panel

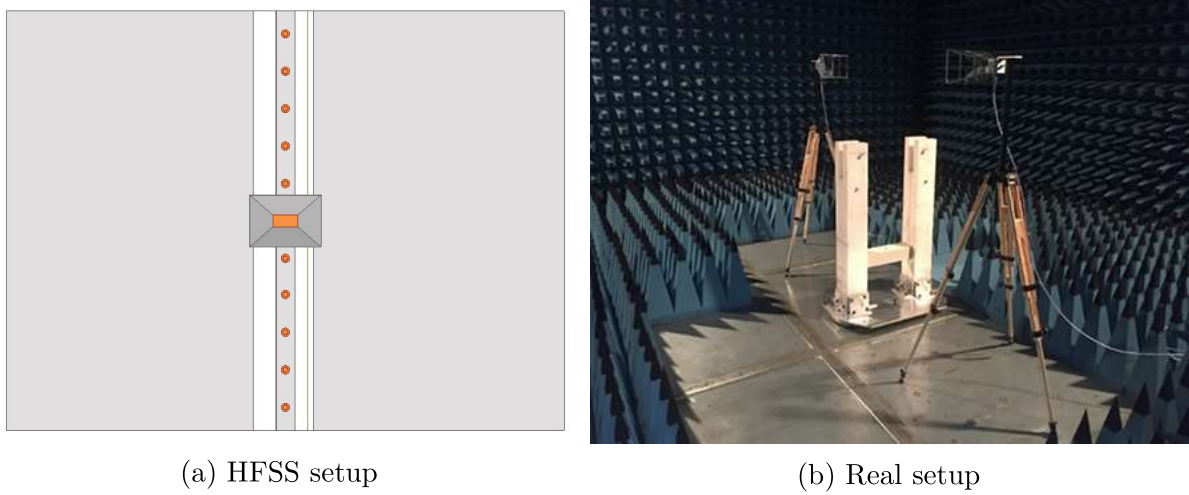
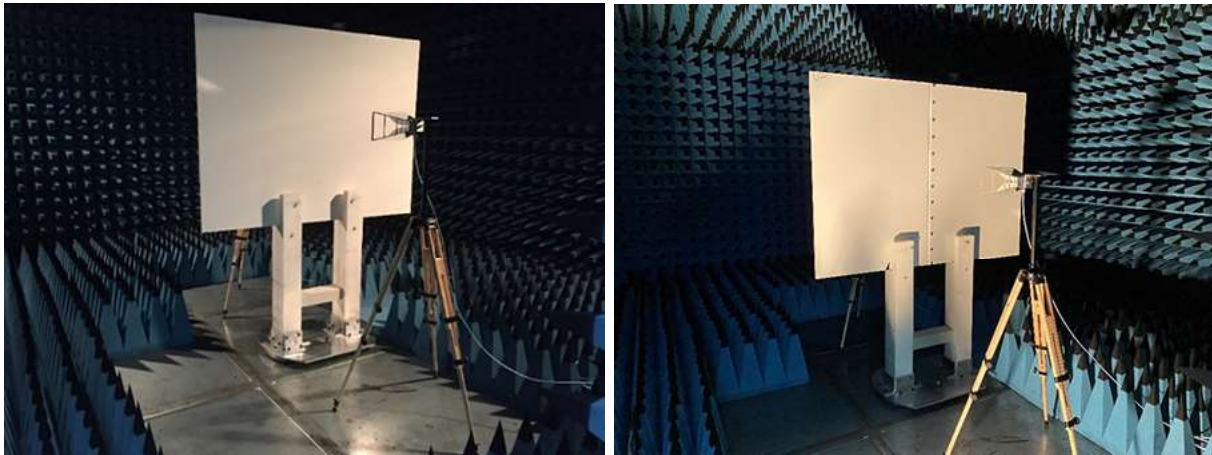


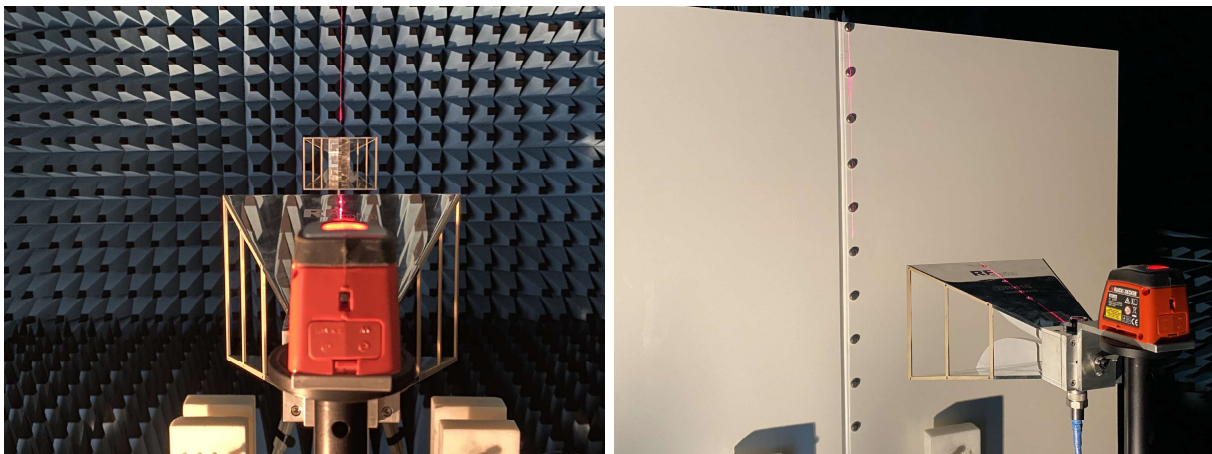
Figure 3.8: Alignment between horns and panel



(a) Without joints

(b) With joints

Figure 3.9: Panel measurements in FDS Facilities



(a) Antenna's alignment

(b) Panel Alignment

Figure 3.10: Laser alignment

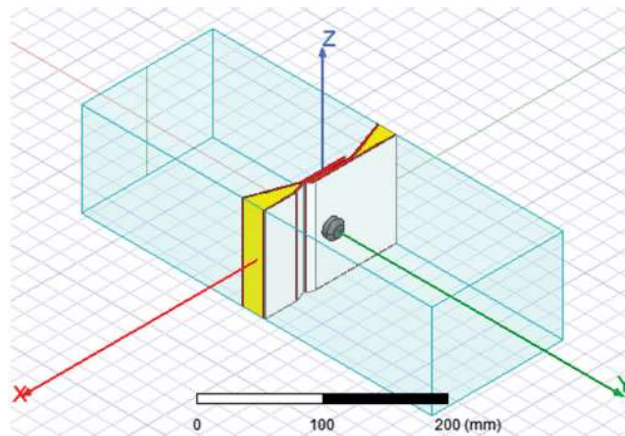
3.1.2 Compensating Ladders Design

During this study, five different working frequency bands are of interest for the IFR compensation. Each design serves a specific band for a specific type of panel, where different panel layering is designed but not presented in this thesis because intellectual properties of FDS Italy Srl.

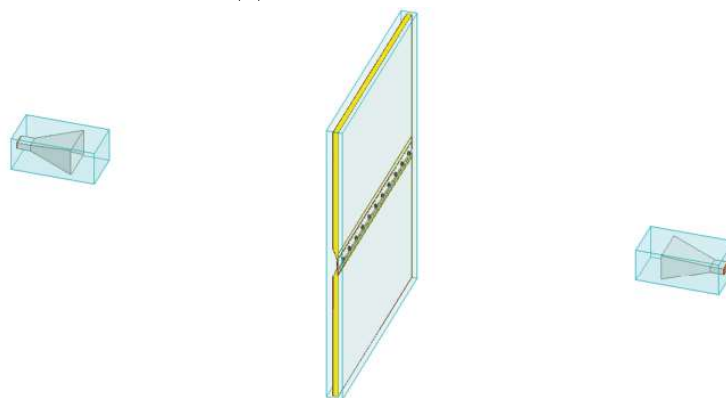
To guarantee a sufficient mechanical robustness, each ladder presents an S parameter (see Fig. 3.6) greater than 1 mm and a thickness of 0.20 mm, that is a constrain due to the copper foil used to build these ladders to guarantee a sufficient mechanical resistance for open windows through punching or photolithography.

Fig. 3.11 shows the simulated model for both vertical (TE) and horizontal (TM) polarization. Due to the field distribution, the vertical TE model can be simplified exploiting the plane of symmetry along the jointed axis (z-axis) and therefore it is possible to simulate a smaller part of the panel. This allows a smaller computational effort and an higher electromagnetic accuracy.

On the other hand, for the horizontal TM model, a similar approach it is not possible: a reduced model of the panel will not give the same electromagnetic accuracy due to the field distribution with respect to the plane of symmetry along the jointed axis (z-axis) and therefore the complete model have been simulated. This increases the complexity of the model which translates to a higher computational effort, suffering the electromagnetic accuracy.



(a) Vertical TE model



(b) Horizontal TM model

Figure 3.11: Comparison simulated TE model and TM model

3.1.2.1 IDEM1-1B

The first case, identified as IDEM1, works in a frequency band from 2.7 GHz to 3.3 GHz and from Fig 3.14 it is possible to notice a good accordance between simulations (dashed line) and measurements (solid line) with a discrepancy between 0.1 – 0.2 dB for the TE case (Fig 3.14(a)). Similar results are reported also for the TM case (Fig 3.14(b)). Peaks in the reported simulated results are numerical errors due to complexity of the electromagnetic model. The built compensating structure is shown in Fig. 3.12. In the same frequency band, a second case identified as IDEM1B is compensated as shown in Fig. 3.15. A good accordance for vertical and horizontal polarization can be noticed. Peaks in simulated results are still numerical errors due to complexity of the electromagnetic model. The compensating structure is shown in Fig. 3.13



Figure 3.12: Copper compensating structure made through punching technique for IDEM1. The same strip can compensate vertical and horizontal polarizations.

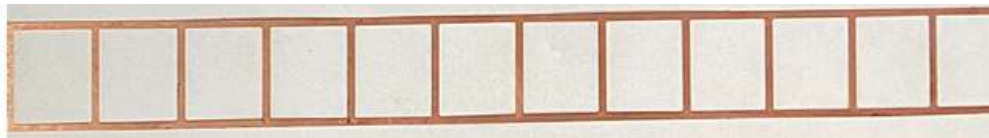
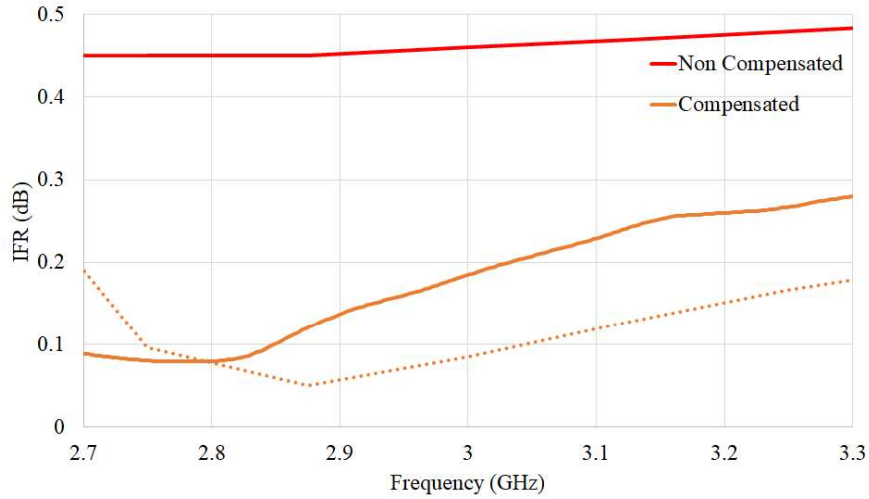
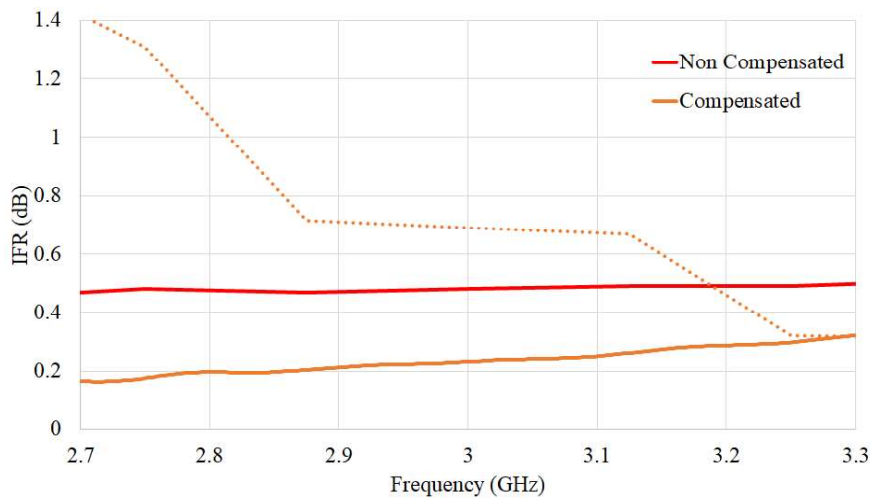


Figure 3.13: Copper compensating structure made through punching technique for IDEM1B. The same strip can compensate vertical and horizontal polarizations.

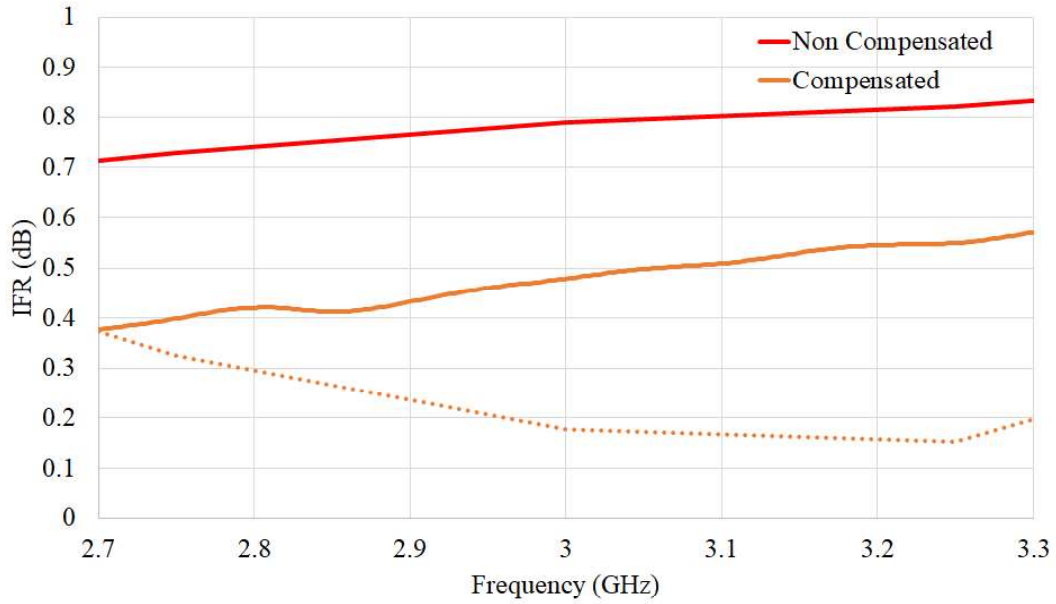


(a) Vertical polarization

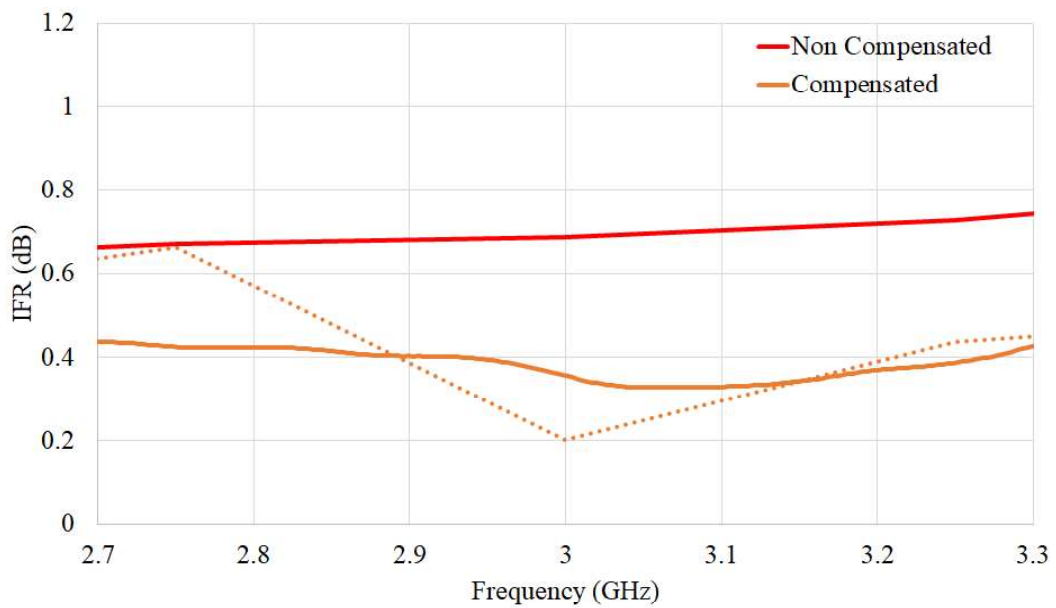


(b) Horizontal polarization

Figure 3.14: Comparison between simulations (dots) and measurements (solid line) of IDEM1 with compensation and non-compensation case.



(a) Vertical polarization



(b) Horizontal polarization

Figure 3.15: Comparison between simulations (dots) and measurements (solid line) of IDEM1B with compensation and non-compensation case.

3.1.2.2 IDEM2

A third object, ITEM2, works in the frequency band from 5.5 to 5.7 GHz is presented in Fig. 3.17 with small discrepancies between simulations and measurements similar to the previous cases. The compensating structure is shown in Fig. 3.16

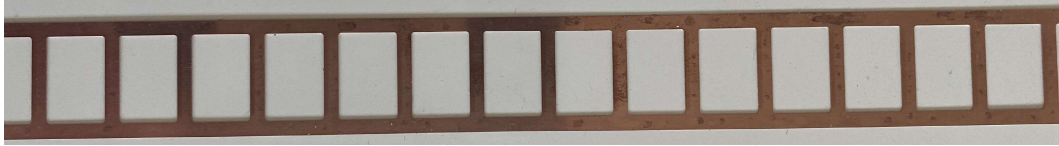
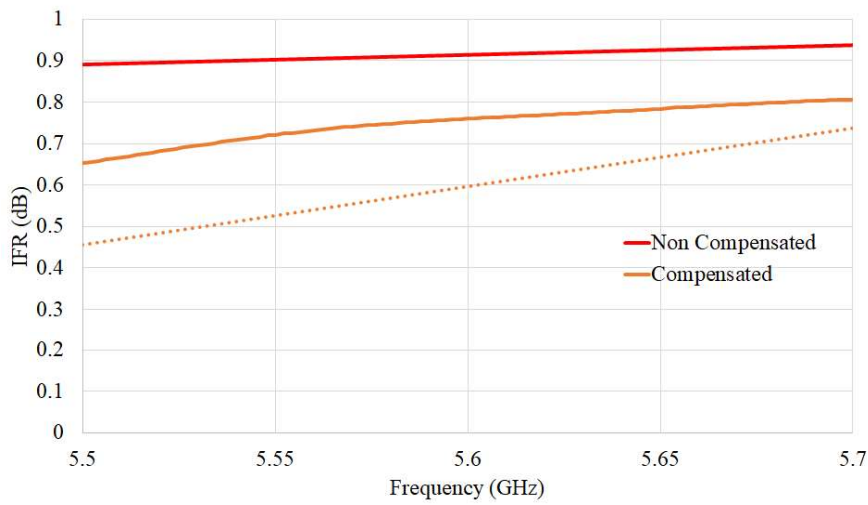
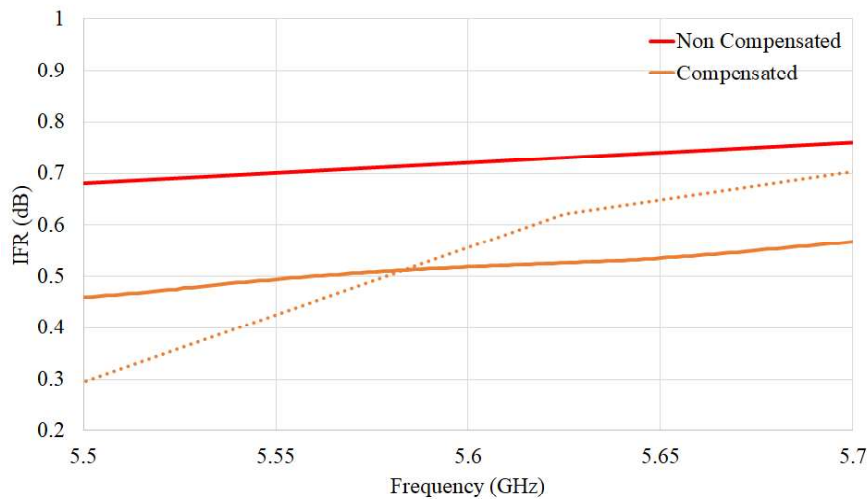


Figure 3.16: Designed compensating structure through punching technique made in copper for ITEM2. The same structure can compensate vertical and horizontal polarizations.



(a) Vertical polarization



(b) Horizontal polarization

Figure 3.17: Comparison between simulations (dots) and measurements (solid line) of ITEM2 with compensation and non-compensation case.

3.1.2.3 IDEM3

The fourth object, ITEM3, works in the frequency band from 1 to 1.7 GHz is presented in Fig. 3.19 with discrepancies between simulations and measurements. Due to the geometry, and the extremely complex model measurements result slightly better than simulations. The compensating structure is shown in Fig. 3.18

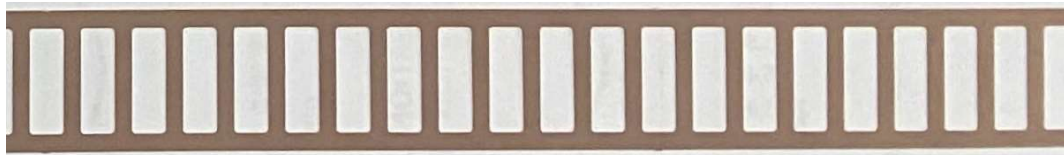
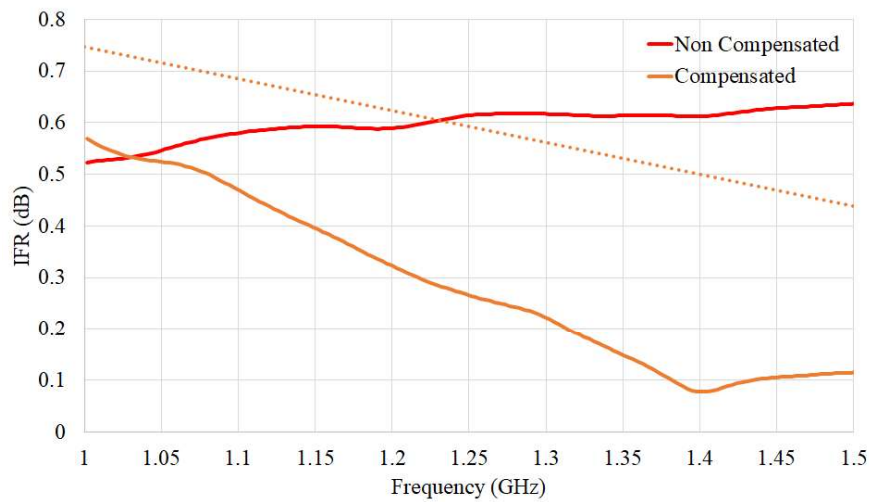
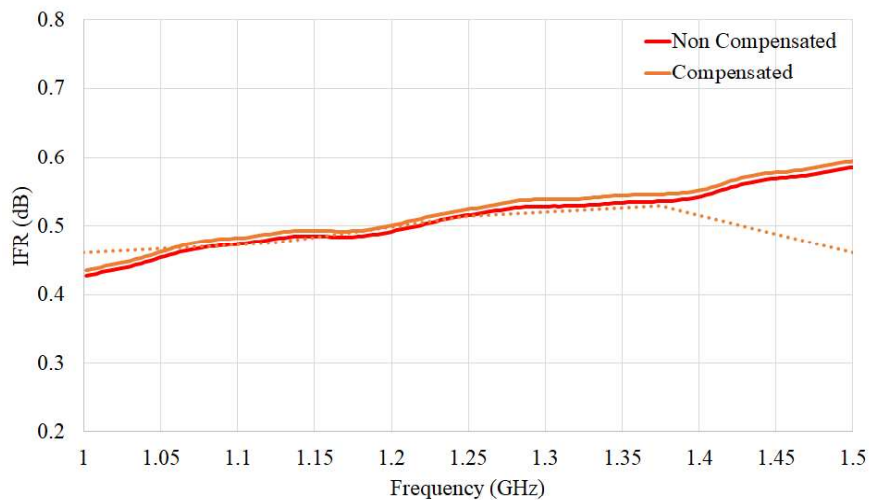


Figure 3.18: Designed compensating structure through punching technique made in copper for ITEM3. The same structure can compensate vertical and horizontal polarizations.



(a) Vertical polarization



(b) Horizontal polarization

Figure 3.19: Comparison between simulations (dots) and measurements (solid line) of ITEM3 with compensation and non-compensation case.

3.2 Weather Raining Condition

One of the key point of radome panels is the non-susceptibility to deposit water on the panel' surfaces. Even if panels are made by low losses materials, accumulation of water on the surface can degrade the electromagnetic behavior increasing transmission losses and ruining the antenna radiation pattern. To mitigate this problem, panels are covered with hydrophobic materials in such way that water droplet slide off the radome surface.

In the literature can be found studies concerning weather behavior of radomes panel. In [8] is described the impact of weather conditions in arctic regions limited to the K-Band while [9] study the systems in the S-Band. Plus, most of the studies that can be found on the hydrophobic behavior of radomes are performed using MSF radomes [10], [11], [12].

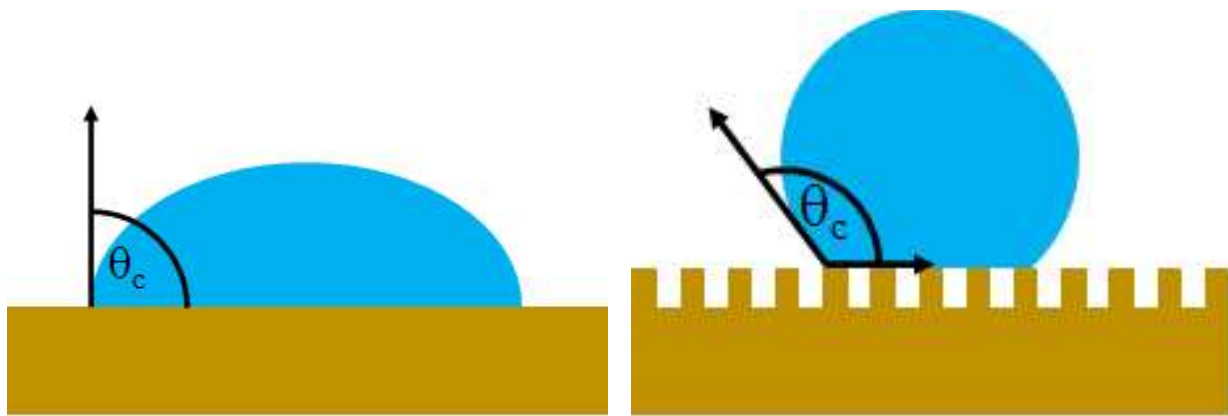
On the contrary, this study aims to characterize the hydrophobicity in different frequency bands from the L-Band to the K-Band (L, S, C, X and K) using ML radomes, in a controlled environment where rain is generated with a specific rainfall rate.

Hydrophobicity of a material is highly dependent on the roughness of the surface [13] as shown in Fig. 3.20. Due to the non-homogeneity of the surface, droplet can be trapped inside "holes" (Wenzel state). In the case of highly rough surfaces there is the possibility that since the distance between "holes" is not sufficient to break the surface tension of the droplet (Cassie-Baxter state), the liquid can be suspended on the surface due to air trapped between the material and the droplet way. As a convention, a surface it is said to be hydrophobic if the contact angle, the angle between the liquid (droplet in this case) and the solid material (panel surface) is $\theta_c > 90^\circ$ (Fig. 3.20a). In fact, for smaller angles, liquid will generate a thin film on the material surface, spreading all over the surface which represent to $\theta_c \sim 0^\circ$. (i.e. cellophane, shiny metals, ceramics). On the other side, as the contact angle increases, liquid will not be able to spread and droplets can be seen on the surface material (Fig. 3.20b).

To study this hydrophobicity of radome panels, a measurement campaign has been performed: on the surface of each panel has been deposited a droplet of bi-distilled water of $5\mu\text{L}$ and the contact angle measurement have been performed though a KSV CAM 200 able to acquire 20 images per second. For each sample, four measurements have been performed with water deposited on different points as shown in Fig. 3.21a. Standard deviation has also been computed. Results are reported in Table 3.2. Bi-distilled water avoid the deposit on the panel surface of any water residual impurity.

During the measurement campaign, different kind of coating materials have been tested as shown in Table 3.2. The first sample identified with G-CA1 does not reach the condition to be considered a pure hydrophobic material, even if the contact angle almost meet the condition $\theta_c > 90^\circ$. Other two gelcoat materials (G-CA2 and G-CA3) barely meet the hydrophobic conditions (3.21b) even if in practical applications, better solutions can be achieved to minimize how much water stops on the surface. In fact, materials identified as H-CA1/2 meet the required condition; measurements show that these two surface are extremely hydrophobic as shown in Fig. 3.21c.

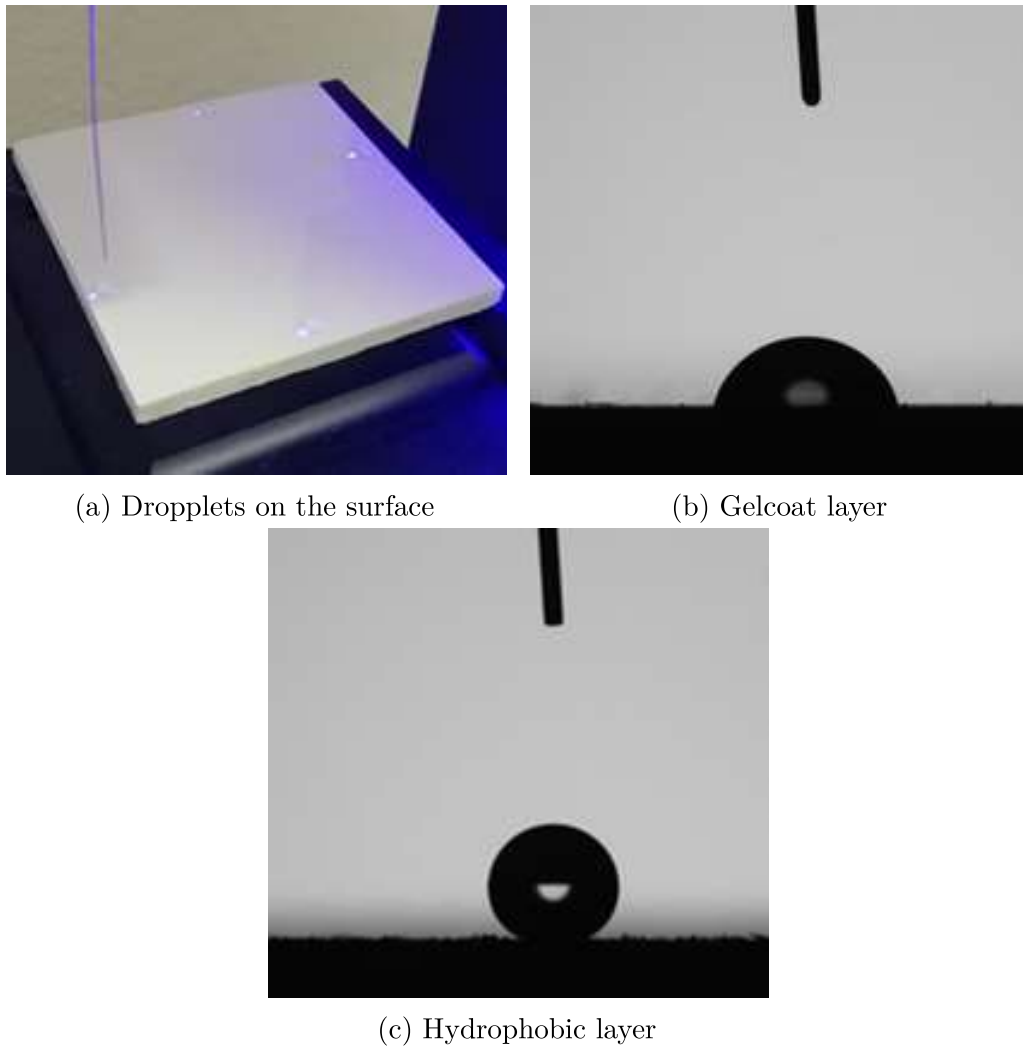
Hydrophobic materials, therefore, minimize the water presence on panel surface but as this advantage do not come for free. These treatments are extremely expensive and require periodical maintenance to guarantee their nominal characteristics.



(a) Hydrophobic threshold $\theta_c = 90^\circ$

(b) Hydrophobic threshold $\theta_c > 90^\circ$

Figure 3.20: Contact Angle for rough surfaces



(a) Droplets on the surface

(b) Gelcoat layer

(c) Hydrophobic layer

Figure 3.21: Contact Angle for rough surfaces

The experiment has been conducted through the Sigma/ 2 - S2Cb water pump [14] (see Fig 3.23), able to guarantee a rainfall rate of 10-20-30-50-100 and 180 mm/h. A sort of shower has been built; a system of sprinklers connected to the water pump is used to make rain on the panel surface, and a panels' support bounded to the shower allows to rotate panels with respect to the ground plane to study the different angle conditions (30° , 45° and 60°). The panel surface used for the test is $30 \times 30 \text{ cm}^2$. This test is repeated for both linear polarization (vertical and horizontal). A low-cost prototype of the shower is shown in Fig. 3.23(a). The complete structure will have transparent walls (plexiglass) for backsplash and a system to collect water on the ground.

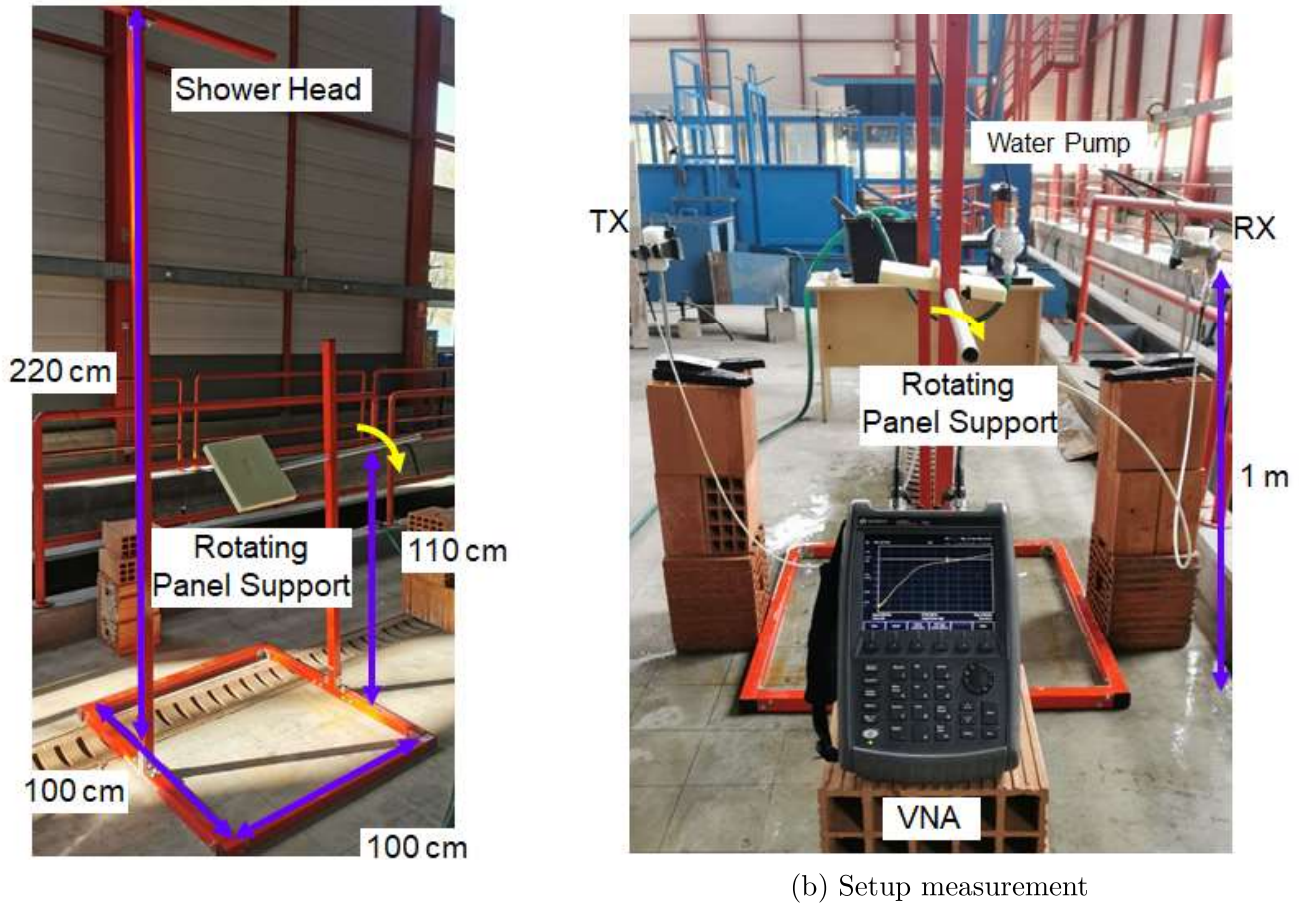
The complete setup measurements (shown in Fig. 3.23(b)) will be made by the shower with a (manually) rotating panel support and a set of broadband antennas at a distance of 60 cm from the centre of the support, in the far-field region. Due to the metallic nature of the shower, possible scattering effects will be compensated through a Fast Fourier Transform made by the vector analyser used for measurements.



Figure 3.22: Sigma/ 2 - S2Cb water pump [14]

Table 3.2: Measured contact angle (θ_c) and standard deviation (SD) of samples, coated with Gelcoat (G) and Hydrophobic (H) layer

Sample	θ_c (deg)	SD (deg)
G-CA1	74	6
G-CA2	95	2
G-CA3	94	5
H-CA1	157	2
H-CA2	156	1



(a) Shower prototype

(b) Setup measurement

Figure 3.23: Prototype of shower to generate controlled rainfall to test radomes' panels hydrophobicity

Measurements in Ku band (10-14 GHz) at the maximum rainfall rate (180 mm/h) have been performed as follow:

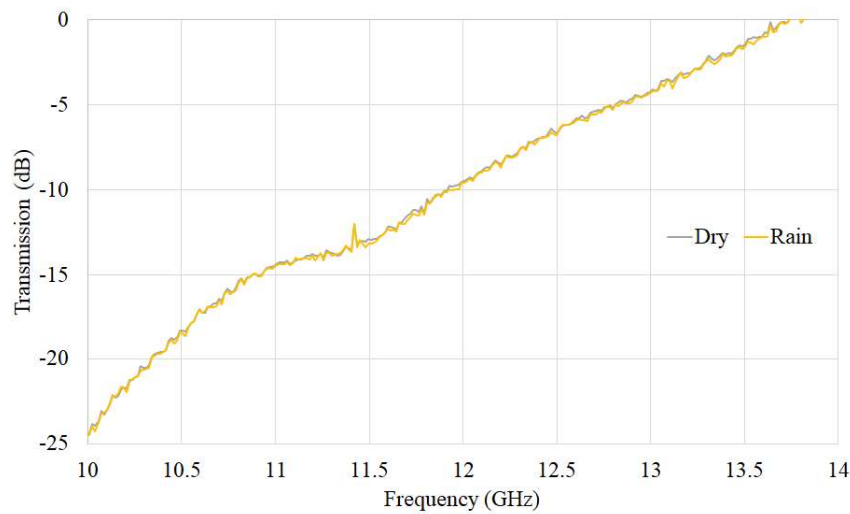
- shower only: with/without rain;
- shower + support only: 30 – 45 – 60° dry;
- shower + support with gelcoat panel: with/without rain - 30 – 45 – 60°;
- shower + support with hydrophobic panel: with/without rain - 30 – 45 – 60°.

As expected, no significant differences between the three angles of the support as well as the measured environment in both dry and rain conditions without support (Fig. 3.24(a)-(b)). The presence of rain in the measured atmosphere will not give a significant effect, making it non susceptible to unwanted scattering effect because rainfall is much slower with respect to the electromagnetic field in this working frequency. Moreover, droplets size is much smaller than the wavelength.

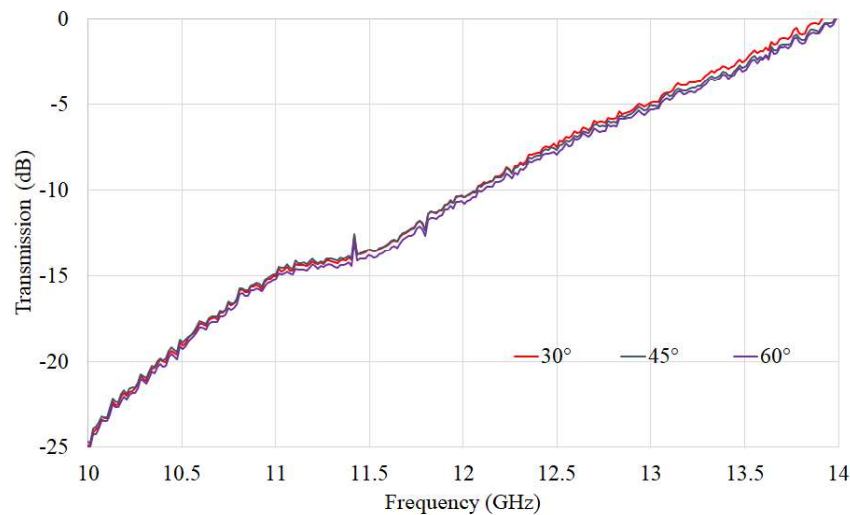
Different in the case of the gelcoat panel (Fig. 3.25) in which there is a significant difference between wet and dry panel (about 2 dB at 12 GHz). This because gelcoat layer is so smooth that water deposits on it, creating a sort of layer that increases EM losses. As expected, for a 30° panel angle, water layer will be much thicker than higher angles (60°). Fig. 3.26 shows

the normalized values between the dried gelcoat panel with respect to the wet one, enhancing the difference between smaller and higher angles.

Hydrophobic panel, on the other hand, are less affected by water presence on its surface, this because due to its characteristic, even for small rotation angles (30°) water will not stop on the surface, slipping away. Therefore the measured results will be almost the EM losses of the panel itself (Fig. 3.26). Difference between dry and wet panel has been measured and it is possible to appreciate differences only for a 30° angle, while 45° and 60° angles are almost impossible to distinguish. Anti-physical results (normalization above 0 dB) from 12 GHz to 15 GHz are due to rain moving the panel during measurements and/or non perfectly alignments between panel and antennas, since the entire alignment process is done by hand, using a simple spirit level.

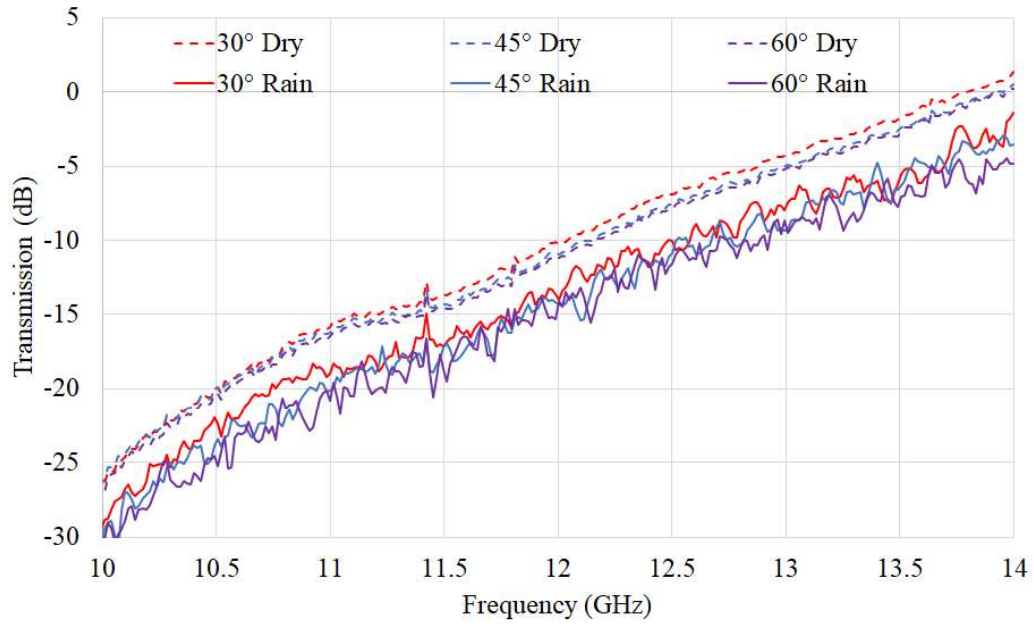


(a) With/without rain - shower only

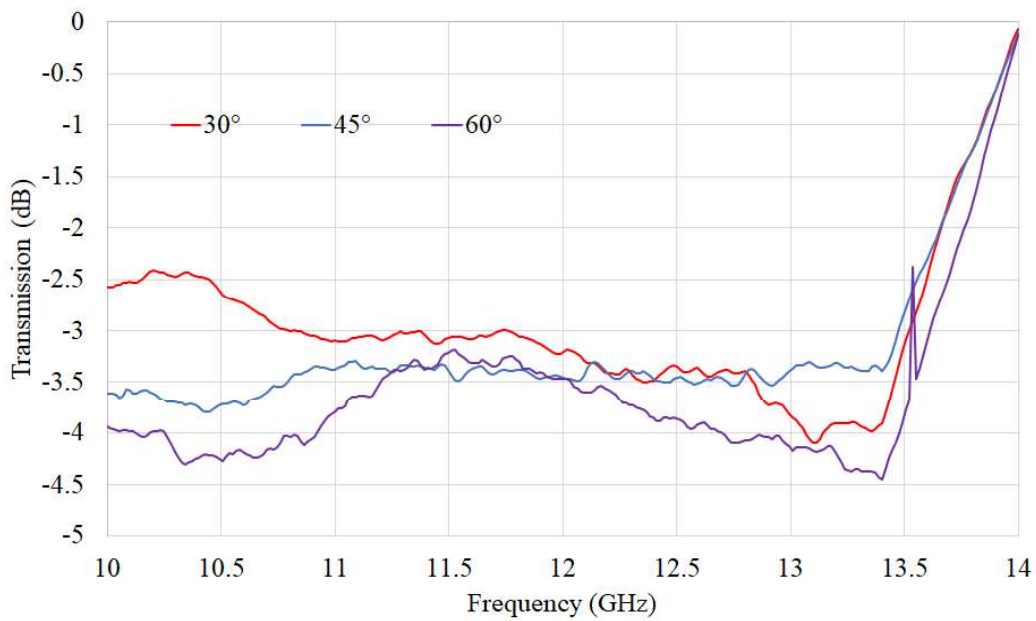


(b) With support - dry

Figure 3.24: Measurements in Ku band of (a) the structure only and (b) the structure with panel support for different angles. Support must remain dry to avoid interference during the panels measurements.

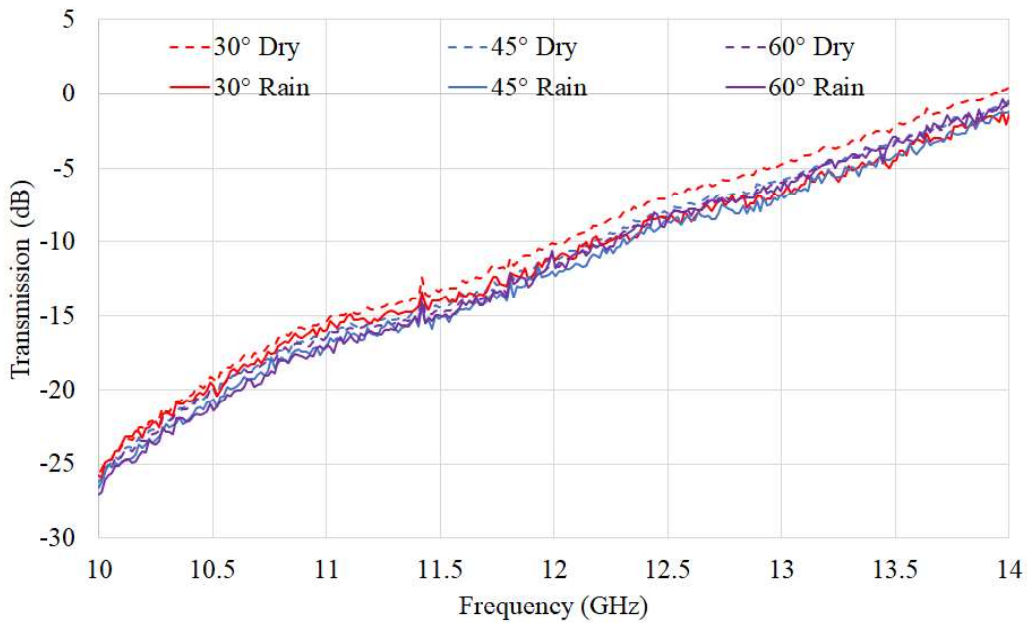


(a) Gelcoat

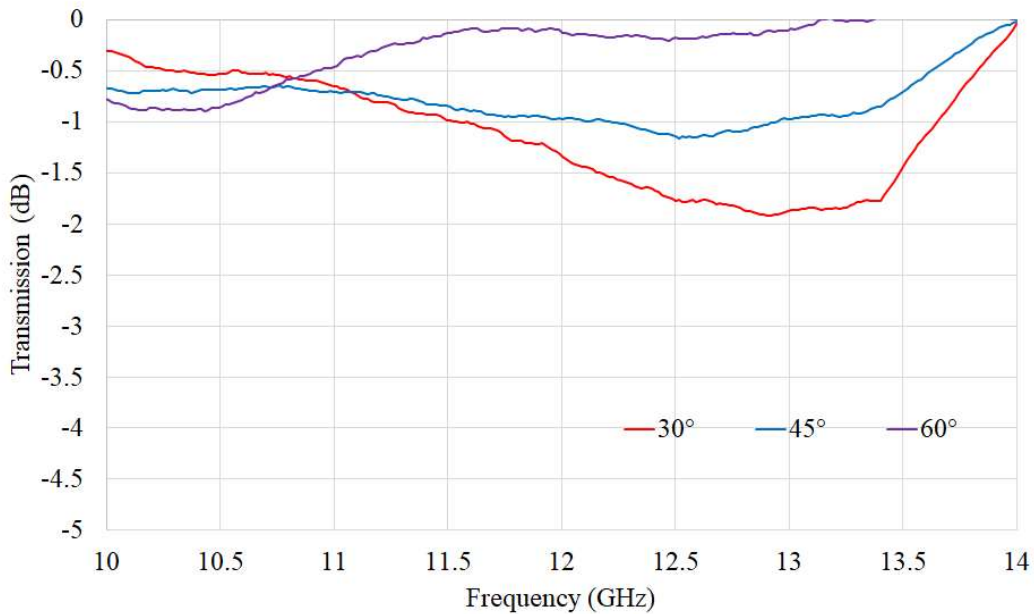


(b) Normalized Gelcoat

Figure 3.25: Measurement of gelcoat panels in Ku Band. (a) dry panel (dashed lines) and wet panels (solid lines) while (b) shows the normalized measurements with respect to dry panels



(a) Hydrophobic



(b) Normalized Hydrophobic

Figure 3.26: Measurement of hydrophobic panels in Ku Band. (a) dry panel (dashed lines) and wet panels (solid lines) while (b) shows the normalized measurements with respect to dry panels. Normalization is more sensitive to measurement errors because behaves similarly to dry panels

3.3 Conclusion

In this third chapter, transparency of radome panels have been characterized. In particular, structures to compensate the presence of metallic bolts and rivets in the jointed section has been researched through the Induced Field Radio model to minimize any de-pointing problem due to the presence of radome protecting a ground station. Simulations and measurements of these structures show that the compensation is possible. Ideally, is it possible to compensate the amplitude of IFR to be zero in a specific working frequency, but since radome panels work in a larger frequency band, a total compensation is not possible. Even thou, the IFR minimization is possible designing specific optimized structures.

A study of highly hydrophobic materials have also been conducted to minimize any electromagnetic scattering due the presence of water droplets, ice or snow on radome surface. Presented results are a proof of concept on panels' hydrophobicity in a specific frequency band. Measurements in this sense confirm that panels coated with hydrophobic materials behave as almost-dry panel with respect to standard panels without hydrophobic coating.

References

- [1] *Gut-wrenching footage documents arecibo telescope's collapse*, <https://www.nature.com/articles/d41586-020-03421-y>.
- [2] A. Kay, "Electrical design of metal space frame radomes", *IEEE Transactions on Antennas and Propagation*, vol. 13, no. 2, pp. 188–202, 1965. DOI: 10.1109/TAP.1965.1138397.
- [3] R. Shavit, A. Smolski, E. Michielssen, and R. Mittra, "Scattering analysis of high performance large sandwich radomes", *IEEE Transactions on Antennas and Propagation*, vol. 40, no. 2, pp. 126–133, 1992. DOI: 10.1109/8.127395.
- [4] *Stazione radio base*, https://it.wikipedia.org/wiki/Stazione_radio_base.
- [5] *Echelon*, <https://en.wikipedia.org/wiki/ECHELON>.
- [6] J. Richmond, "Scattering by a dielectric cylinder of arbitrary cross section shape", *IEEE Transactions on Antennas and Propagation*, vol. 13, no. 3, pp. 334–341, 1965. DOI: 10.1109/TAP.1965.1138427.
- [7] W. Rusch, J. Appel-Hansen, C. Klein, and R. Mittra, "Forward scattering from square cylinders in the resonance region with application to aperture blockage", *IEEE Transactions on Antennas and Propagation*, vol. 24, no. 2, pp. 182–189, 1976. DOI: 10.1109/TAP.1976.1141307.
- [8] A. Rudge, K. Milne, A. Olver, and P. Knight, *The Handbook of Antenna Design*, ser. IEE electromagnetic waves series v. 1. P. Peregrinus, 1982, ISBN: 9780906048825.
- [9] A. Mancini, R. M. Lebrón, and J. L. Salazar, "The impact of a wet s-band radome on dual-polarized phased-array radar system performance", *IEEE Transactions on Antennas and Propagation*, vol. 67, no. 1, pp. 207–220, 2019. DOI: 10.1109/TAP.2018.2876733.
- [10] D. Gibble, "Effects of rain on transmission performance of a satellite communication system", *IEEE International Convention Record*, 1964.

- [11] A. Cohen and A. Smolski, “The effect of rain on satellite communications earth terminal rigid radomes(rain effect on satellite communications earth terminal rigid radomes, determining transmission loss and water film thickness)”, *Microwave Journal*, vol. 9, pp. 111–121, 1966.
- [12] J. A. Effenberger, R. R. Strickland, and E. B. Joy, “The effects of rain on a Radome’s performance”, *Microwave Journal*, vol. 29, pp. 261–274, 1986.
- [13] R. N. Wenzel, “Resistance of solid surfaces to wetting by water”, *Industrial & Engineering Chemistry*, vol. 28, no. 8, pp. 988–994, 1936. DOI: 10.1021/ie50320a024. [Online]. Available: <https://doi.org/10.1021/ie50320a024>.
- [14] *Water pump sigma/ 2 - s2cb, prominent*, <https://www.prominent.co.uk/en/Products/Products/Metering-Pumps/Motor-Driven-Metering-Pumps/p-sigma-x-s2cb-control-type-motor-driven.html>.

Conclusions

This thesis aims to evaluate the de-pointing problems in antennas for space applications in monopulse tracking systems. These problems are mainly due to errors in component design (tracking chain) but a significant contribution is also given by the presence of radome and water accumulation on it that enhance the de-pointing.

To solve the first problem, this thesis proposes a simple yet effective way to calibrate monopulse tracking systems in-lab in order to evaluate in advance the de-pointing before the tracking chain is installed on the antenna and, in case, re-design its component avoiding antenna downtime.

For the second case, radome panels are typically jointed through metallic bolts or rivet, increasing the EM scattering and therefore enhancing the de-pointing. To minimize this effect, compensating resonant structures have been designed. Moreover, water presence (either in liquid or solid form) on radome surface may increase even more the de-pointing. An experimental evaluation of panels (manufactured by FDS Italy Srl) has been conducted. Two type of coating panels have been tested in a controlled environment for different rain conditions. As expected, hydrophobic coating surface drastically reduce the EM scattering and therefore reducing de-pointing errors.

These results will lead to a significant upgrade in the design of antennas for space applications with the possibility to boost even more the communication performances.

Future development of this research will be to motorize the in-lab calibration of the tracking chain in order to automate the operation and further enhance the radome EM transparency by designing even more efficient compensating structures.

List of Publications

- [1] G. Ceccato, J. L. Cano, A. Mediavilla, and L. Perregrini, “Controlled high order mode generation for tracking coupler bench test”, in *2020 IEEE/MTT-S International Microwave Symposium (IMS)*, 2020, pp. 904–907. DOI: 10.1109/IMS30576.2020.9224025.
- [2] —, “A simple and accurate method for circularly polarised monopulse tm01 tracking system testing”, in *2020 23rd International Microwave and Radar Conference (MIKON)*, 2020, pp. 218–221. DOI: 10.23919/MIKON48703.2020.9253906.
- [3] —, “Controlled excitation of waveguide high-order modes for a simple and accurate monopulse tracking system test bench”, *IEEE Transactions on Microwave Theory and Techniques*, vol. 69, no. 2, pp. 1327–1334, 2021. DOI: 10.1109/TMTT.2020.3045202.
- [4] J. L. Cano, G. Ceccato, T. Fernandez, A. Mediavilla, and L. Perregrini, “An ultra-compact full-band waveguide quadrature hybrid coupler”, *IEEE Microwave and Wireless Components Letters*, pp. 1–4, 2021. DOI: doi:10.1109/LMWC.2021.3116103.